WAVE TAILORING GRANULAR MATERIALS: EFFECT OF RANDOMNESS AND PLANE WAVE PROPAGATION

BY

MOHITH MANJUNATH

DISSERTATION

Submitted in partial fulfillment of the requirements
for the degree of Doctor of Philosophy in Aerospace Engineering
in the Graduate College of the
University of Illinois at Urbana-Champaign, 2014

Urbana, Illinois

Doctoral Committee:

Professor Philippe H. Geubelle, Chair
Professor John Lambros
Professor Alexander Vakakis
Assistant Professor Oscar Lopez-Pamies
Assistant Professor Huck Beng Chew

Abstract

This thesis addresses some of the fundamental issues/aspects as well as practical significance of impact response in granular media. In the first part of the study, we investigate numerically the effect of randomness in material and geometric properties on wave propagation behavior in 1D and 2D granular media. Results obtained for both 1D chains and 2D media show the kinetic energy amplitude decays with distance, with the rate of decay found to depend on the level of randomness and the distance from point of impact. The kinetic energy amplitude initially decays exponentially before transitioning to a universal power-law regime that is valid for all levels of randomness. The power-law regime is fundamentally due to the presence of secondary waves whose amplitude is higher than that of the primary wave after the point of transition. Another key result quantifies the rate of decay of force amplitude in a 2D square packing system along various directions of propagation. Several contour maps are obtained that demonstrate the directions along which we can obtain minimum or maximum decay, which are practically relevant for material design.

In the second part of the study, we focus on plane wave propagation in higher dimensional structures. In the case of 2D and 3D monodisperse granular media, we demonstrate an equivalence with 1D chains and consequently derive the relation between wavefront speed and force amplitude in higher dimensional systems. Subsequent normalization results in a universal wavefront speed-force amplitude relation that is valid across the different ordered 2D and 3D systems such as hexag-

onal, body-centered cubic and face-centered cubic packings. We also investigate the effect of angular impact on granular media and discuss mechanism through which the shearing component of the loading is propagated in the system. In the case of 2D dimer systems, we consider a square packing system with interstitial intruders. Following the procedure that we developed for monodisperse granular media, we obtain an equivalent nonlocal dimer chain that gives the same response with relevant scaling of material properties. In this study, we demonstrate the existence of a new family of plane solitary waves over a wide range of material and geometric properties. We also indicate a discrete set of solutions for which there is locally maximum decay, thereby showing promise for wave mitigation as well.

In the last part of our study, we conduct a preliminary study to investigate the vibration response of beams made of a granular chain embedded in a linear elastic matrix. A nonlinear, dynamic finite element model is developed, in which the granular chain is converted to a series of 1D nonlinear bar elements whose contribution is added to linear quadrilateral elements. We study the bending response by applying a harmonic loading on a composite beam fixed on both ends and show a fundamental difference between the dynamic response of a linear elastic beam and the embedded granular system at resonance. Unlike a linear elastic beam, we find the deflection of an embedded granular system to be finite at resonance. Furthermore, in the presence of precompression, the frequency at which the composite beam deflection is maximum can be controlled based on the level of precompression, acting as an active control feature in material design.

To my teacher.

Acknowledgments

Firstly, I am very thankful to my advisor Prof. Philippe Geubelle for his guidance all through my years at the University of Illinois. In spite of his administrative responsibilities, he made sure to take some time off every week to meet his students and thus making our progress smooth. I also take the opportunity to thank my lab mates: Ahmad Najafi, Amnaya Awasthi, Mahesh Manchakattil Sucheendran, Masoud Safdari, Erheng Wang and Raj Kumar Pal, to name a few, for helpful discussions and more importantly giving an opportunity to contemplate about life in general. I really appreciate Professors John Lambros, Alexander Vakakis, Oscar Lopez-Pamies and Huck Beng Chew for serving as my committee members and giving suggestions over the course of my doctoral study.

I am really grateful to my teacher and a wonderful set of friends here in Urbana, in whose association I am learning to see the world with a different attitude. I owe special thanks to my parents and grandmother for playing their roles in bringing me up and supporting me in my decisions.

Table of Contents

Chapter 1 Introduction **1**
1.1 Literature Review 4
1.2 Thesis Objectives and Outline 13

Chapter 2 Randomness in 1D granular chains **18**
2.1 Problem description and numerical setup 19
2.2 Randomness in mass 21
2.2.1 Decay in force amplitude 25
2.2.2 Decay of the maximum kinetic energy 27
2.2.3 Normalization of response over different impact velocities and Young's moduli 30
2.2.4 Evolution of the force amplitude 33
2.2.5 Distribution of energy during wave propagation 36
2.3 Randomness in Young's modulus and radius 41
2.4 Conclusions 44

Chapter 3 Randomness in 2D granular media **46**
3.1 Problem definition 47
3.2 Results and discussion 51
3.2.1 Characteristics of wave propagation 51
3.2.2 Force amplitude decay 53
3.2.3 Spatial distribution of peak compressive force 60
3.2.4 Evolution of ensemble kinetic energy 67
3.3 Conclusions 69

Chapter 4 Plane wave propagation in monodisperse granular media . . . **71**
4.1 Numerical setup 73
4.2 Normal impact 75
4.2.1 Analytical study 75
4.2.2 Verification 78
4.2.3 Normalization 79
4.3 Angular impact: 2D hexagonal packing 80
4.3.1 Numerical observations 81
4.3.2 Analytical predictions 86
4.4 Conclusions 97

Chapter 5 Plane wave propagation in dimer granular media 99
5.1 Problem statement 101
5.2 Numerical Results 102
5.2.1 Equivalent 1D system 102
5.2.2 Numerical observations 105
5.2.3 Extraction of solitary waves 107
5.3 Analytical investigation 115
5.3.1 Quasi-continuum approximation 115
5.3.2 Asymptotic analysis 122
5.4 Conclusions 130

Chapter 6 Embedded granular systems 132
6.1 Problem description and numerical setup 133
6.2 Finite element formulation 135
6.3 Implementation 137
6.4 Dynamic code verification 138
6.5 Convergence studies 140
6.6 Results: dynamic loading 143
6.6.1 Linear elastic beam 143
6.6.2 Embedded granular system 145
6.7 Conclusions 151

Chapter 7 Conclusions and Future Work 153
7.1 Key contributions 153
7.2 Future directions 155

Appendix A Finite element formulation 160
A.1 Force-displacement relations 160
A.2 Tangent stiffness matrix 161
A.3 Newmark method 162

References 164

Chapter 1

Introduction

Granular media are a unique class of materials whose behavior is different from the three well-known states of matter: solids, liquids and gases. Granular media possess some characteristics of each of the three phases: they can be packed just like solids when the grains are relatively stationary and they can also be made to take the shape of their container like liquids; also, when a container of granular media is vigorously shaken, the grains disperse with infrequent collisions, similar to a gas. Granular materials are discrete particles whose sizes can vary anywhere from a few microns to several kilometers. Among the various granular materials, colloidal particles are typically less than a micron in size, clay particle's size is about few microns, sand particles are usually order of few hundred microns, granule or gravel have characteristic dimension of order of few millimeters and boulders are very large particles with size ranging from tens of centimeters to several kilometers. Each of the above mentioned classes of granular materials is a research area in itself.

Of the many examples found in nature, sand is one case of a very simple form of granular medium commonly encountered. Yet the understanding of the response of sand remains elusive due to its complexity. A key characteristic subject of multiple studies is the *angle of repose*, which is defined as the angle between a sandpile and the horizontal [1]. Beyond a certain angle of repose, the sandpile forms an avalanche which can build in size very quickly as it flows down the slope. Granular materials of various shapes and sizes are also employed in a wide range of industrial applications. Agricultural enterprises need to store, pack and transport food items

such as rice and nuts which are granular in nature. Similarly, the pharmaceutical industry requires different ways to optimally store the powders and manufacture various medicines. Mining is another example where coal, a granular material, is stored and transported often to various industries.

Most of the above examples utilize granular materials usually of the size of few microns to few hundred microns. One of the primary goals of our study is to design a new class of materials that would possess features such as stress wave mitigation, energy conservation or tailoring upon impact. Therefore, in order to derive more flexibility in modifying certain properties of the system at the particle level, we consider granular materials of the size of granules which are spherical in shape (beads) and a few millimeters in diameter. The spheres are stacked either next to each other in a line (1D) or closely packed in an ordered manner in 2D and 3D. In order to take advantage of granular materials for wave mitigation and tailoring, we need to first understand how energy travels in a granular system. Impact on a granular material system causes the energy to propagate along the various inter-particle contacts, which deform due to the relative motion between the contacting particles. If the stress developed at a contact is less than the yield stress of the material, the spheres remain elastic; otherwise there will be permanent plastic deformation.

In granular media with spherical particles, we need an elastic force-displacement model between two spheres in contact in order to perform numerical simulations or compare with experiments. Several researchers [2, 3] have found that the classical Hertz theory for elastic solids in contact provides satisfactory results since it was first proposed in 1882 [4]. In the Hertzian law, the applied load, F, is related to the distance of approach of the spheres' centers, δ, as $F \propto \delta^{3/2}$. The proportionality factor is a function of material and geometric properties which will be defined in the later sections.

Wave propagation in granular media made of spherical particles is unique as it differs from wave propagation in linear elastic continuous media in several ways. In continuous media, both tensile and compressive waves are linear and travel at constant speeds dependent on the material properties of the medium. In contrast, wave propagation in granular media intrinsically depends on the nonlinearity at inter-particle contacts due to the Hertzian law. There is also a second source of nonlinearity which stems from the fact that the spheres do not exert any force in tension, unlike continuous media. Over the past few decades, the Hertzian law has been used by various researchers to study the dynamics of granular media [3]. In a 1D homogeneous chain of spheres just touching each other without initial compression at contacts, numerical investigation using the Hertzian law and experiments have demonstrated the presence of nondispersive waves with compact support known as solitary waves [5]. These solitary waves were first observed in a water channel where they were found to be stable and travel very long distances without decay. Unlike a linear elastic wave, the speed of a solitary wave depends upon its amplitude as a consequence of the Hertzian law. For example, in a system of linear elastic spherical granules, the speed of a solitary wave (V_s) varies with its force amplitude (F_m) as $V_s \propto F_m^{1/6}$ [5]. Also, the width of a solitary wave in a spherical particle-system is determined to be about five particle diameters, but in general it depends upon the shape of the granule [2].

Since the granular materials can be discretely inhomogeneous, i.e., offer the flexibility of altering the material and geometric properties of each granule, there is enormous scope to employ the materials in a wide range of areas [6]. Thus there is also a possibility of tailoring the impact energy in preferential directions by changing the properties locally. These materials find applications in topics such as impurity or damage detection in materials [7, 8, 9], generation of high-accuracy focusing and high-energy acoustic pulses [10], and impulse confinement and disintegration

[11, 12]. Also, granular systems in the presence of precompression at some or all the contacts demonstrate a different kind of dynamics whose continuum approximation is found to follow the Korteweg-de Vries (KdV) equation. The solitary waves in the case where the contact deformations are much smaller than the precompression are more closely related to the KdV equation solution [5]. The presence of precompression allows sound propagation in the granular system and has been successfully employed in applications and areas such as acoustic lens (or sound bullet) and band gaps.

1.1 Literature Review

One of the earliest attempts to numerically understand the effect of nonlinearity in a dynamical system was undertaken by Fermi, Pasta and Ulam [13]. The chosen dynamical system was a 1D lattice of masses connected by springs with the nearest neighbors having weak quadratic or cubic interactions in addition to linear interactions, popularly known as the FPU problem or lattice. The goal of their study was to determine if there was any equipartition of energy among the various modes of vibration. While the linear case shows that the string of particles vibrates indefinitely according to the initial mode of excitation with equipartition, the FPU lattice surprisingly did not show equipartition of energy among all the degrees of freedom. The energy was mostly carried by a particular mode at a given instant of time. In the following decades, the FPU problem has been revisited and several theoretical studies were conducted to explain some of the phenomena including a continuum approximation of the FPU lattice [14].

While the earlier studies considered quadratic or cubic variations, Nesterenko [5] formulated the problem of a 1D chain of homogeneous spheres interacting via the Hertzian potential. Nesterenko first assumed that the relative displacements

between the contacting spheres to be much smaller than the precompression level and showed that the resulting continuum approximation has properties of the KdV equation mentioned earlier. The opposite case, i.e., the relative displacements being much larger than the precompression level, also showed the existence of solitary waves in the continuum approximation where a surprisingly simple solution different from the KdV equation was obtained by taking the solution to be a traveling wave with a certain phase velocity. Nesterenko then performed numerical simulations to confirm the presence of solitary waves in a 1D granular chain. Lazaridi et al. [15] conducted the earliest set of experiments where a piston of certain mass impacted a chain of spheres and a comparison was made with numerical results. A reasonable agreement was found between the experimental and numerical results, demonstrating solitary waves for the first time in a granular chain with no linear interaction component (acoustic speed equal to zero). Later, the concept of "sonic vacuum" was introduced [16] to indicate the inability of a granular chain in absence of linear interaction component to allow acoustic disturbances to propagate in the system. Nesterenko [16] performed a more in-depth theoretical analysis of an equivalent 1D continuum system with stress-strain relationship $\sigma \propto \xi^n$ and $n > 1$. The conditions for which solitary waves exist in such systems and the spatial length of the waves as a function of n were also derived. Further, several experiments were also conducted [16, 17] to study the characteristics of a solitary wave at the interface between two sonic vacua. The mass of the piston impacting the first sonic vacuum was varied, resulting in a series of waves in some cases and a single pulse in others. The piston mass plays a role because the contact time with the first sphere depends on the two masses in contact and a higher loading time will lead to the decomposition of a single wave into series of waves with decreasing amplitude.

Coste et al. [18] conducted detailed experimental analysis on a 1D chain of spheres with moderate or zero precompression, and the results were consistent

with the theoretical predictions of Nesterenko. Wave velocity and force amplitude measurements demonstrated and verified the nonlinear dependence for both with and without static force. Following the comprehensive study by Coste et al., few studies focused on theoretical analysis of the existence of solitary waves in granular chains. In the first study, Mackay [19] applied the result of Friesecke et al. [20] to the Hertzian model and concluded that solitary wave exists if the potential energy is greater than zero and the precompression force $F \geq 0$. While Mackay's study focused on the Hertzian model, Ji et al. [21] later extended it to a more general class of granular chains where the power-law exponent n is taken to be arbitrary, i.e., the shape of the particles are not necessarily spherical. Following a similar approach as Mackay's, Ji et al. proved that the criterion for the existence of solitary waves is $n > 1$. Several other experiments have also been conducted on homogeneous [22] and heterogeneous granular media [23], demonstrating solitary wave propagation and wave speed characteristics. Since the granular materials are highly tunable to extract required wave propagation behavior [2], these material systems found potential applications in many areas such as granular protectors [12], acoustic lens [10], shock mitigation and absorption [3] and band-gaps [24].

Many studies have also focused on tapered and decorated granular chains, whose design can lead to a wide variety of energy absorption devices [25, 26, 27, 28]. In analytical consideration of tapered and decorated granular chains, Harbola et al. [27, 28] used a binary collision approximation, where the pulse is assumed to propagate via interaction of two particles at a time. Although the model overpredicted the pulse amplitude in that study, it was found to capture very well other key characteristics, such as the pulse speed and the decay rate. The interaction of a solitary wave with a wall or a material interface [11, 29, 30] and characteristics of wave propagation in chains with different geometries or mass defect [31, 32] have also been subjects of interest. Recent efforts have focused on extending the granular contact law to in-

clude the effects of plasticity for simulating a wider range of granular materials. Pal et al. [33] conducted a two-part study wherein an elasto-plastic force-displacement law between two elastic-perfectly plastic spheres in contact was extracted using finite element analysis and then used to perform wave propagation studies in 1D granular chains. In the dynamic study, the force amplitude was found to decrease as expected but a more detailed analysis showed different regimes of decay such as exponential and inverse regimes. Several scaling laws were derived to effectively capture the wave propagation characteristics for a wide range of input forces. Further, phenomena such as wave trains and wave merging were revealed that require a more focused research to understand the effect of plasticity on wave propagation. Carretero-Gonzalez et al. [34] introduced an additional term in the Hertzian model to capture dissipative effects arising in the experiments other than friction and plasticity. The additional term comprises of a dissipative force dependent on the relative velocities of the spheres which has a prefactor and an exponent as the two unknown parameters. Several experiments and numerical simulations were performed and systematically compared to obtain the dissipation coefficients for three different materials. Interestingly, the exponent was found to be approximately constant for all the materials while the prefactor was material dependent.

Sokolow et al. [35] reported additional set of results on solitary wave train formation in elastic granular chains. Their results demonstrated the effect of striker mass on wave propagation where a single solitary wave is formed if the striker mass is less than or equal to the mass of a sphere in the chain while a series of solitary waves (wave train) is formed otherwise. The solitary waves' amplitudes decrease progressively in the wave train and the decay is found to be approximately exponential. Later, Job et al. [36] performed further analysis of homogeneous and stepped (decreasing radius) chains by comparing simulations with theory and experiments. Using a quasi-particle approach wherein a solitary wave is approximated as a single

quasi-particle carrying the momentum and energy of the solitary wave, the exponential decay rate of the solitary wave force amplitude was predicted and showed to be in good agreement with the simulations and experiment. Pal et al. [37] conducted dynamic studies on wave propagation in elastic and elasto-plastic chains for a wide range of loading conditions. In the elastic case, a map was generated showing the transition between the single solitary wave and wave train regimes depending on the loading amplitude and time. In elasto-plastic chains, the wave propagation behavior is found to be different for both short and long loading times. Multiple waves are formed even for the case of short loading time as the spheres in free flight behind the leading wave collide, which was not the case in elastic chains.

On the theoretical side, a few studies have proposed approximate solutions for the solitary waves in 1D homogeneous chains, which have been shown to be more accurate than the Nesterenko's continuum approximation. Chatterjee [38] developed an asymptotic solution for the solitary wave as a perturbed Gaussian. Although the asymptotic analysis was developed for the case of the power-law exponent in $F \propto \delta^n$ to be $n = 1 + \epsilon$ with $\epsilon \ll 1$, the resulting solution was found to be accurate even for the Hertzian case with $n = 1.5$. The third-order approximation was shown to be nearly identical to the discrete numerical solution and therefore considerably more accurate than the Nesterenko's solution. On the other hand, Sen et al. [6] formulated an infinite series solution from a hybrid numerical-analytical approach. Firstly, an analytical function was formulated based on the boundary conditions of a solitary wave, which resulted in a function containing an infinite number of unknown coefficients. Then the first few unknown coefficients were numerically determined by comparing with displacement time derivatives of various orders. The coefficients are only a function of n and thus a solitary wave of any amplitude and time delay can be generated with just one set of coefficients for a given n. Sen's solution also demonstrated a significant improvement over the Nesterenko's solution.

In ordered heterogeneous granular media, Jayaprakash et al. [39] conducted detailed studies on 1:1 dimer (repeating units of one heavy and one light sphere) granular chains demonstrating a new family of solitary waves in the system. The solitary waves, whose dynamics satisfy antiresonance properties, were obtained for a discrete set of normalized mass ratios. The velocity profiles of the spheres in a dimer unit vary depending on the mass ratio. An asymptotic analysis based on separation of time scales and using the mass ratio as a small parameter predicted some of the solitary wave cases with a reasonable accuracy. Further, another set of mass ratios showed attenuation of the primary pulse, which was reported in a separate study [40], thus paving way for applications that require wave mitigation or transmission. Also, Potekin et al. [41] experimentally verified the resonances and antiresonances in the dimer chain. The experimental setup was distinct from other studies in that the spheres were left hanging using flexures thus making it relatively easier to align the dimer system. The study on 1:1 dimer chains was further extended to a more general class of 1:N dimers [42] where qualitatively different solitary waves were demonstrated for the case of $N = 2$ while such 1:1 or 1:2 solitary waves were absent for $N > 2$.

Most studies have so far focused on nonrandom systems although randomness is unavoidable in experiments due to a variety of sources such as manufacturing limitations leading to variance in geometric and material properties, and alignment of spheres. Although several studies have reported results on dynamics of 1D and 2D granular media, few have focused on wave propagation in random or disordered granular systems. Manciu et al. [43] simulated a 1D chain of elastic spheres with randomness included in their masses, and found an exponential decay in maximum kinetic energy of the spheres. Ponson et al. [44] studied the dynamics of a 1D disordered dimer chain where the orientation of the dimer units (heavy-light or light-heavy spheres) was chosen randomly. The results revealed the presence of a

critical disorder level beyond which the wave propagation became independent of the level of disorder. Furthermore, the spatial decay in maximum kinetic energy and peak force was shown to transition from an exponential to a power law at the point of critical disorder. In the present work, we extend the above two studies by conducting numerical simulations on wave propagation in 1D elastic chains incorporating randomness in mass, Young's modulus and radius of the spheres, and analyze the energy distribution. Long chains investigated in the study demonstrate the existence of two regimes of decay - exponential and power law - for any level of randomness.

There have been fewer studies on wave propagation in two-dimensional (2D) granular media. Shukla et al. [45, 46] conducted dynamic photoelastic experiments to study load-transfer paths and contact forces in cubic and hexagonal packing of disks. A key aspect of these studies was to predict the angular dependence of the load transfer between two neighboring contacts. Results from their study indicate the presence of two distinct chains in hexagonal packing, i.e., primary chains originating from the impact location and secondary chains that are in contact with the primary chains. The experiments also showed that the load transfer from one contact to a neighboring contact occurs only if the angle between the normals at the contacts is obtuse. In a related study [47], the aforementioned packings were simulated using a discrete element method (DEM) and the results captured key features of the experiments reasonably well. The parameters for the linear contact law used in the simulations were determined from photoelastic experiments. In another study, Sadd et al. [48] employed a dynamic finite-element model to study wave propagation by including both the normal and tangential force components at each contact. However, the contact law was assumed to be linear in displacements and therefore some of the features of wave propagation were not captured accurately.

More recently, several researchers have performed systematic investigation of

wave propagation in 2D granular media. Leonard et al. [49, 50] performed experiments and numerical simulations to study anisotropy of response in square packing of spheres and cylinders. Depending on the material properties of the larger and smaller spheres, several wavefront shapes were identified ranging from directional to uniform propagation. Although there is variability in experiments due to randomness and other sources of error the mean experimental results were in good agreement with the numerical results. Awasthi et al. [51] also conducted various simulations on 2D square packing of spheres with intruders at interstitial locations to produce a wave propagation map based on the shape of the wavefront. The map is particularly useful to identify regimes where impact energy can be redirected in certain directions to create a wave-tailoring material. Szelengowicz et al. [52, 53] analyzed equipartition and distribution of energy in the presence of one or more intruders in 2D square packing system and revealed more efficient ways to distribute energy. In particular, the equipartition in 2D systems was found to be more complex than observed in other nonlinear lattices and a reduced 1.5D model predicted the 2D response reasonably well.

Some preliminary studies were also undertaken on wave propagation in a random packing of monodisperse spheres [46, 54]. Sadd et al. [54] found that the maximum tangential load was about two times that of a hexagonal packing due to the packing being irregular. As expected, the photoelastic fringes were asymmetric [46] in a random packing due to the presence of tangential or shear load. In another study [55], experiments and simulations were conducted to evaluate the effect of diameter tolerances on wave propagation response of square lattices with cylinders at interstitials. This study shows that even small changes in sphere diameters can cause significant deviation from ideal (perfectly ordered) response. The key effect comes from the fact that the granular packing is altered when the spheres' diameters are changed. As part of this thesis, we investigate the effect of randomness in

density of the spheres in 2D granular media and show its potential in designing optimum granular crystals depending on the objective function. We also demonstrate the effect of the degree or level of randomness wherein the response of the system "saturates" after a certain degree of randomness.

In 2D granular media, most studies in the open literature have focused on wave propagation associated with a point impact. These point impact studies address some fundamental aspects such as shape of the wavefront and decay of the force amplitude due to dimensionality [51]. There are few studies that focus on the other "extreme" case in which a granular medium is subjected to a plane impact, either uniform perpendicular or oblique impact. Plane wave propagation studies have focused on topics such as acoustic wave propagation and nonlinear dispersive waves. Chang et al. [56] derived a stress-strain model for granular media and applied it to plane wave propagation. Anfosso et al. [57] performed experiments to investigate planar impact on granular media under precompression to study acoustic wave propagation. In particular, the experiments demonstrated the effect of surface waves in 3D cubic and hexagonal granular packings. Tichler et al. [58] conducted theoretical and numerical studies on the effect of solitary waves planar front at the interface between two dissimilar hexagonal granular lattices. The interface was either perpendicular or oblique to the propagating front, and an analogue of Snell's law was derived for the oblique case. Although the Snell's law was derived by approximating the solitary wave as a quasiparticle with an effective mass, a reasonable comparison was nonetheless obtained. In the current work, we conduct a numerical and analytical study of planar normal or oblique impact on 2D and 3D monodisperse granular media such as hexagonal packing and face-centered cubic packing. For uniform normal impact, a universal relation between the wavefront speed and its force amplitude is derived based on 1D equivalence of higher dimensional structures.

1.2 Thesis Objectives and Outline

The thesis investigates some of the fundamental aspects of granular media and concludes with a study on practical application of granular systems. On that front, the thesis is organized into several chapters broadly addressing randomness, plane wave propagation and embedded granular systems. Some of the key questions, classified into the above areas, that we are interested to answer are as follows:

- Randomness in 1D and 2D granular media
  - Do solitary waves exist in random granular chains?
  - How do results of wave propagation due to variations in geometric and material properties differ qualitatively and quantitatively?
  - How does backscattering affect wave mitigation?
  - Can we employ randomness to tailor wave propagation?
  - Are there fundamental differences between wave propagation in 1D and 2D granular media?
  - What is the effect of randomness in 2D on wavefront profile, keeping nonrandom profile as the reference?
  - Is the force decay directional in 2D, and more importantly can we control it?
- Plane wave propagation in granular media
  - Does plane impact produce solitary waves in monodisperse (homogeneous) systems? What happens in dimer systems (alternating layers of larger and smaller spheres)?
  - Are there 1D equivalent chains for higher dimensional granular systems? If so, how do the responses relate to each other?

  - What happens if the impact is plane but coming at an angle relative to the granular system?
  - What are the similarities and differences between plane wave propagation in 2D/3D dimer systems and 1D dimer chains?
  - Can we control the response of a 2D/3D dimer system by selectively changing the geometric/material properties of the particles?

- Embedded granular systems
  - How do we utilize granular systems in reality?
  - What are the common and feasible ways to embed granular systems?
  - Can we take advantage of nonlinearity in granular systems in a practical way such as controlling the bending response of embedded granular systems?
  - What role does precompression play in the dynamic response of embedded granular systems?

The topics presented in this thesis will have a visible impact on the technology front where manufacturing remains a constraint even though several studies on granular media have shown potential engineering applications such as shock absorption devices, energy confinement or redirection and damage detection. Some of the models developed in the present work will enable commercial finite element solvers such as Abaqus® to significantly reduce computational cost for larger and nonperiodic domains. Successful implementation of the models into finite element solvers will further spark an interest in communities both in academia and industry to identify newer material designs. The studies will also open various avenues for future researchers in the areas of optimization of granular networks in matrix system and plasticity.

A brief outline of the thesis is as follows. Chapter 2 describes the effect of randomness on wave propagation in 1D granular chains. Randomness can be present in any of the material and geometric properties and correspondingly affects the amount of transmitted force or energy. In the present work, the focus is on randomness in mass of the particles but the influence of randomness in Young's modulus and radius is discussed as well. The distribution of the total compressive force amplitude and maximum kinetic energy are analyzed both numerically and analytically. In the absence of randomness, the force amplitude of the leading wave remains constant whereas it evolves in different ways depending on the degree (or level) of randomness. We use the virial theorem with Hertzian potential to analyze the distribution of kinetic and potential energies for nonrandom and random systems. The results of the above study has been published as "Wave propagation in random granular chains." *Physical Review E* 85.3 (2012): 031308.

Chapter 3 extends the study of randomness in 1D granular chains to 2D systems particularly discussing the effect of randomness in density in square packing system with intruders. Wavefronts in 2D granular systems provide a visual way to identify the directionality of wave propagation and therefore we present snapshots of wave propagation with a brief discussion on the shape of the wavefront. Unlike 1D granular chains, 2D granular systems require a detailed understanding of surface contours to come to meaningful conclusions about the force distribution. Major part of the investigation is dedicated to study of contours of peak force distribution in the whole domain to analyze the isotropy or anisotropy of the wave propagation. And finally, the evolution of energy components is compared with the virial theorem and with the corresponding response of 1D random granular chains. The results of the above study has been published as "Wave propagation in 2D random granular media." *Physica D: Nonlinear Phenomena* 266 (2014): 42-48.

Chapter 4 complements the previous studies on point impact by considering plane impact and provides a novel way of reducing higher dimensional periodic granular structures to 1D equivalent systems. Planar impact on a granular system could be either normal or oblique to the impacting surface. We discuss the normal impact case for 2D and 3D granular media and provide analytical derivation and verification for equivalent 1D chains. We also describe the angular impact case where the effect of shear loading on wave propagation is demonstrated. Also, some analytical predictions for some of the key phenomena observed in the angular impact case are derived and compared with numerical observations. The results of the above study has been published as "Plane wave propagation in 2D and 3D monodisperse periodic granular media." *Granular Matter* 16.1 (2014): 141-150.

Chapter 5 presents the effect of planar impact on periodic dimer (inhomogeneous) granular structures. A new family of plane solitary waves is demonstrated in the 2D dimer granular crystals similar to the solitary waves in a 1D dimer chain. We determine an equivalent 1D nonlocal dimer chain for the 2D bidisperse (dimer) system and verify its formulation. Some of the analytical methods used to study wave propagation in homogeneous systems can be employed in the present case since the 2D dimer system permits solitary waves in special cases. Analytical techniques such as the quasi-continuum approximation and asymptotic analysis are used to predict some of the primary phenomena observed numerically. The results of the above study has been published as "Family of plane solitary waves in dimer granular crystals." *Physical Review E* 90.3 (2014): 032209.

In Chapter 6, we conduct preliminary numerical studies on vibration response of a granular chain embedded in a linear elastic beam. The granular chain is modeled by 1D nonlinear bar elements derived from the Hertzian contact law, whose contribution is added to the linear quadrilateral elements for the beam. We verify the finite element formulation and summarize the results for the bending behavior

of a embedded granular system. We also include precompression in the granular chain and determine the vibration response for different levels of precompression.

Chapter 2

Randomness in 1D granular chains

The nonlinear nature of the classical Hertzian contact law in granular media opens up a wide spectrum of applications in engineering ranging from acoustic lenses to shock absorption. Numerous studies have been performed to understand the underlying physics as well as tuning material properties for specific applications [3]. However, there are very few studies that address disorder or randomness in granular systems although, in reality, randomness can lead to substantial variations in data due to variety of sources. Some of these sources are variations in geometric and material properties and those due to experimental/human error. Therefore, in design of new granular material systems, randomness is expected to play a crucial role due to its ubiquitous presence. In this chapter, our aim is to understand the effect of randomness on wave propagation in 1D granular media.

We perform a numerical study on wave propagation in 1D elastic chains of spherical beads in contact. Randomness is incorporated in masses, Young's moduli or radii of the particles using either uniform or normal distribution. We investigate both low- as well as high-disorder systems and in particular quantify the level of randomness on the spatial decay in force and kinetic energy. The study demonstrates the presence of two decay regimes, exponential and power law, for all the aforementioned cases. By employing the analytical relation between the wave speed and the force amplitude, we predict the evolution of the location of the wavefront and its force amplitude. We also analyze the energy distribution in the system by applying the virial theorem for random systems where we observe a gradual

transfer from potential to kinetic energy.

The chapter is organized as follows: Section 2.1 contains the equations of motion for a system of elastic spheres in contact and describes the setup used in the simulations. Sections 2.2.1 and 2.2.2 describe the effect of randomness in the mass of the particles on the distribution of the total compressive force amplitude and maximum kinetic energy. In Sec. 2.2.3, we perform a parametric study of the effect of the impact velocity on the force amplitude for different levels of randomness. In Sec. 2.2.4, semi-analytical expressions are derived for the location of the leading pulse and the evolution of the force amplitude. Section 2.2.5 analyzes the distribution of kinetic and potential energies using the virial theorem. In Sec. 2.3, the influence of randomness in Young's modulus and radius is compared with that of randomness in masses. The results of the above study has been published in the journal *Physical Review E* where the remainder of the sections are extracted from: "Wave propagation in random granular chains." *Physical Review E* 85.3 (2012): 031308.

2.1 Problem description and numerical setup

Consider a 1D chain of N elastic spheres (beads) of mass m_i, radius R_i, Young's modulus E_i and Poisson's ratio ν_i in contact with no precompression. Under compression, the Hertzian contact force [4] is assumed between adjacent spheres and, denoting the displacement of i^{th} sphere by u_i, the equation of motion for sphere i is given by

$$m_i\ddot{u}_i = k_{i-1,i}\left\langle u_{i-1} - u_i\right\rangle^{3/2} - k_{i,i+1}\left\langle u_i - u_{i+1}\right\rangle^{3/2}, \tag{2.1}$$

with $k_{i,j} = (4/3)E^*\sqrt{R^*}$, where $E^* = E_iE_j/[E_j(1-\nu_i^2) + E_i(1-\nu_j^2)]$ is the effective elastic modulus and $R^* = R_iR_j/(R_i + R_j)$ is the effective radius. In Eq. (3.1), $\langle a\rangle = a$ if $a \geq 0$ and $\langle a\rangle = 0$ otherwise.

Spheres are assigned the following mean properties: radius $R_0 = 5.0$ mm, den-

sity $\rho_0 = 7850$ kg/m^3, Young's modulus $E_0 = 200$ GPa and Poisson's ratio $\nu_0 = 0.30$. Randomness is introduced in the properties using either uniform or normal distribution. For the uniform distribution case, randomness in property p (where p is one of mass, Young's modulus or radius) for sphere i is defined as [43]:

$$p_i = p_0(1 + r_i\varepsilon), \tag{2.2}$$

where p_0 is the mean value, $-1 \leq r_i \leq 1$ is a uniformly distributed random number and $0 \leq \varepsilon < 1$ is the degree of randomness with the case $\varepsilon = 0$ corresponding to the nonrandom system. For the normal distribution case, the property p is normally distributed with mean p_0 and standard deviation $p_0\varepsilon/3$. Here, there is a possibility of the property p to become negative. In such a case, the normal distribution is truncated so as to lie between $p_0(1 - \varepsilon)$ and $p_0(1 + \varepsilon)$.

One of the main objectives of the present study is to analyze the evolution of a solitary wave as it propagates through a random chain. To that effect, we combine a nonrandom chain with a random chain so as to fully establish a solitary wave before entering the random chain. Both chains are chosen long enough to avoid end effects and capture the dynamics in long random chains. The nonrandom chain is composed of beads of equal mass and radius and identical material properties, and the random chain is composed of beads with randomly distributed properties with the same mean values as the nonrandom chain. The initial conditions correspond to an initial velocity V_0 imparted to the first bead in the nonrandom sub-chain far away from the interface. The solitary wave formed travels toward the interface, enters the random chain, and due to impedance mismatch gets partly transmitted and partly reflected. We report the results treating the interface of the two sub-chains as the origin.

The evaluation of influence of randomness over wave propagation is largely

governed by the distribution of randomness, controlled by the parameter r_i. Each realization generated using r_i gives a unique evolution of wave propagation, and thus we evaluate the response of several such realizations and take the average. The results are averaged over 10 realizations for each degree of randomness (ε) based on the observed convergence for the force amplitude (tolerance of 2% for $\varepsilon = 0.9$). The numerical simulations are performed using the fourth-order Runge-Kutta method with a time step of 10^{-7} s. The present setup does not include any dissipation effects, thus the sum of the potential and kinetic energy of the system remains constant over time.

2.2 Randomness in mass

Figure 2.1(a) shows snapshots of the total compressive force distribution for a typical simulation with $\varepsilon = 0.3$ and uniformly distributed masses. The total compressive force on a sphere is defined as the sum of the compressive forces experienced at left and right contacts, i.e.,

$$F_i = \left|F_{i-1,i}\right| + \left|F_{i,i+1}\right|. \tag{2.3}$$

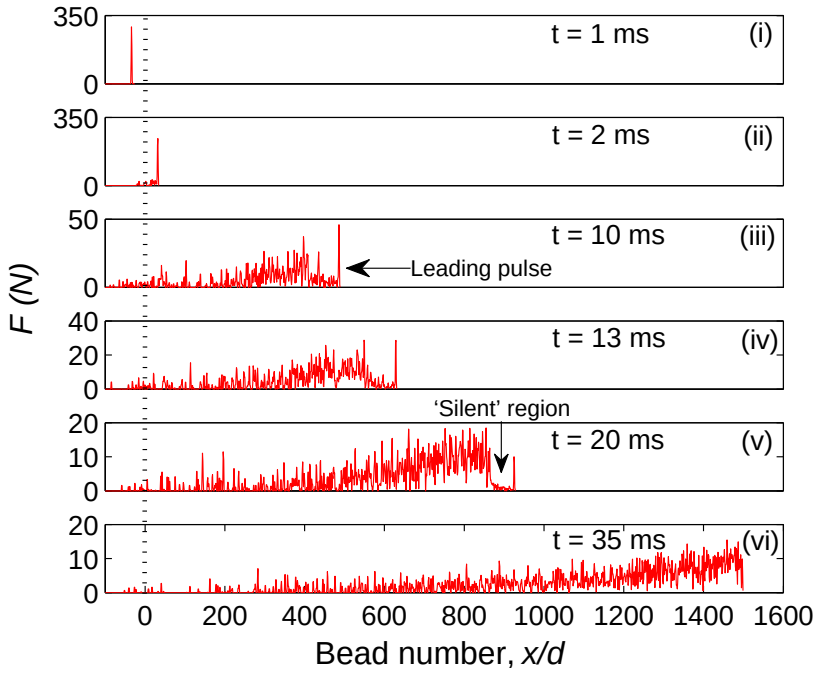

(a)

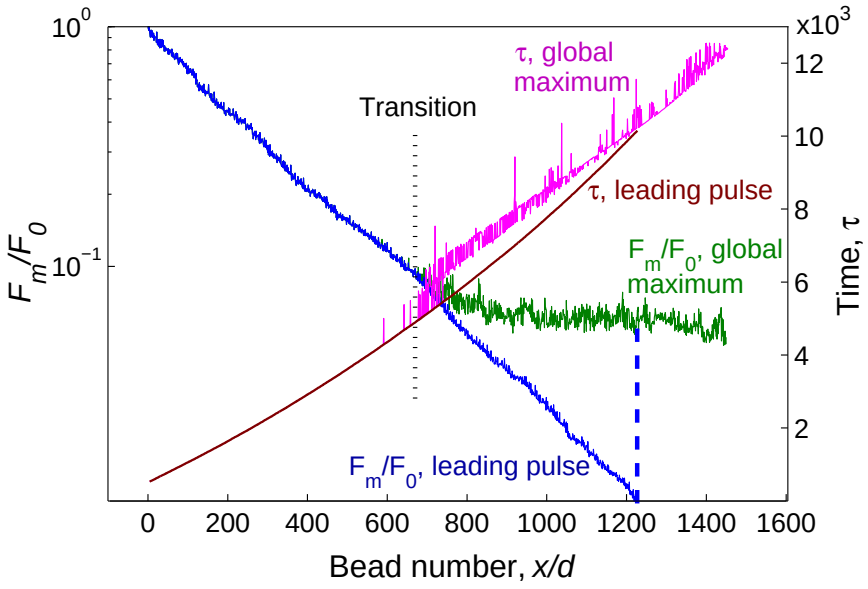

(b)

Figure 2.1: (a) Snapshots of total compressive force acting on each bead, showing the decay of the amplitude of the leading pulse for $\varepsilon = 0.3$, uniform distribution (note the change in the scale of the vertical axis). The dotted line at the origin represents interface between the nonrandom and random sub-chains. Here, $d = 2R_0$ is the diameter of the beads. (b) Left ordinate depicts force amplitude in the random chain (F_m) normalized by force amplitude in the nonrandom chain (F_0). The right ordinate represents the normalized time ($\tau = (k_0\sqrt{R_0}/m_0)^{1/2}t$). The force amplitude and corresponding time for the leading pulse and the global maximum are considered.

The solitary wave first propagates in the nonrandom sub-chain at constant amplitude without backscattering since all of incident energy is transmitted at each contact [Fig. 2.1(a)(i)]. However, in the random segment, part of the incident energy is transmitted, another part is reflected because of impedance mismatch at each contact. These numerous reflection/transmission phenomena at successive contacts lead to a rapid attenuation of the amplitude and the creation of noise behind the wave as the disturbance propagates [Fig. 2.1(a)(ii)-(vi)] [43]. After a certain distance, the amplitude of the leading pulse decreases below the amplitude of the scatter (noise behind the leading pulse), snapshot of which is shown in [Fig. 2.1(a)(iv)]. This transitional behavior will be further explored in the next section. As observed in Fig. 2.1(a)(v), a small region of low-amplitude scatter is observed just behind the leading pulse, which we refer to as the 'silent' region. The occurrence of the 'silent' region can be qualitatively explained as follows. During the initial stages of propagation in the random segment, the amplitude of the leading pulse is higher than that of the scatter and thus the leading pulse travels faster than the scatter. Since the amplitude of the leading pulse attenuates with distance, the reflected waves generated by it at larger distances have amplitude smaller than that of those generated closer to the interface (dotted line in Fig. 2.1(a)). Simultaneously, owing to higher speed of the leading pulse, the size of the 'silent' region increases. However, when the amplitude of the leading pulse reduces below that of the scatter [Fig. 2.1(a)(iv)], the scatter propagates faster than the leading pulse and, with a sufficiently long chain, the leading pulse merges with the scatter [Fig. 2.1(a)(vi)]. The trailing scatter catching up with the leading pulse stems from the nonlinearity at inter-particle contacts which leads to the aforementioned relation between the wave velocity (V_s) and force amplitude (F_m), $V_s \propto F_m^{1/6}$. We find the behavior illustrated in Fig. 2.1(a) to be characteristic for low degrees of randomness, where we observe a solitary wave-like shape propagating through the chain. For higher degrees of randomness,

the state in Fig. 2.1(a)(vi) is reached earlier since the amplitude of the leading pulse decreases more rapidly to below the amplitude of the scatter. This quick attenuation leaves no time for a noticeable size of the 'silent' region to appear and thus the leading pulse merges with the scatter very quickly. Figure 2.1(b) illustrates the normalized force amplitude distribution of wave propagation in random chain with $\varepsilon = 0.3$. The normalizing factor, F_0, is the force amplitude in the nonrandom sub-chain [Fig. 2.1(a)(i)]. As shown in Fig. 2.1(a), the amplitude of the leading pulse progressively decays and, at some point ($t \approx 13$ ms) becomes lower than that of the trailing scatter. To characterize the transition, the amplitude distributions of the leading pulse (blue curve) and of the global maximum (green curve) are presented. The dotted line labeled 'Transition' in Fig. 2.1(b) refers to the location at which the global maximum curve deviates from the leading pulse. Further inquiry into this transition shows that the location corresponds to the instant at which the amplitude of the leading pulse begins to reduce below that of the scatter [Fig. 2.1(a)(iv)]. Later, the amplitude of the leading pulse experiences a sudden jump (dashed vertical line) due to the merger of the leading pulse with the scatter [Fig. 2.1(a)(vi)]. Figure 2.1(b) also presents the x-t diagram for the propagation of the disturbance in the random chain. Two times are monitored, one corresponding to the global maximum and another that to the leading pulse. Before the transition, the curves for the leading pulse and the global maximum overlap as the amplitude of the leading pulse is equal to the global maximum. After the transition, the global maximum occurs in the trailing scatter and since there is no well-defined peak for the trailing scatter, we observe fluctuations in the curve. The quantification of the force amplitude decay in the two regimes of propagation is discussed next.

2.2.1 Decay in force amplitude

The attenuation of the pulse amplitude can be characterized by studying the distribution of the total compressive force amplitude. Figure 2.2 shows the spatial variation of the force amplitude (F_m) normalized by that of the nonrandom segment (F_0). The data is presented for different degrees of randomness ranging from $\varepsilon = 0.1$ to 0.8. The case for $\varepsilon = 0$ (nonrandom chain) corresponds to a horizontal line as the solitary wave propagates without decay in the force amplitude. In the presence of randomness, we observe two distinct regimes of decay. In regime I, the decay of amplitude is approximately exponential [43] described by $F_m(x) = F_{01}exp[-\alpha_F(\varepsilon)x]$. In regime II, the decay of amplitude follows a power-law behavior characterized by $F_m(x) = F_{02}x^{-\beta_F}$. Here, F_{01} and F_{02} are constants which are functions of the material properties and the radii of the particles. Ponson et al. [44] observed a similar power-law decay of the force amplitude after a certain critical disorder level in a chain of dimer units with random orientations. As shown in Fig. 2.2, the transition between exponential and power-law decay depends on ε. For lower degrees of randomness, the transition can be noticed only if the chain is sufficiently long, as also noted in [44]. The power-law behavior is universal, as the decay follows the same law for all degrees of randomness. Thus, the decay parameter β_F is a constant whereas the decay parameter α_F is a function of ε, as discussed later. Furthermore, Fig. 2.2 shows that the decay in regime I is also independent of ε beyond a certain value of ε, as indicated by the peak force distribution of $\varepsilon = 0.7$ and $\varepsilon = 0.8$, and will be discussed in the next section.

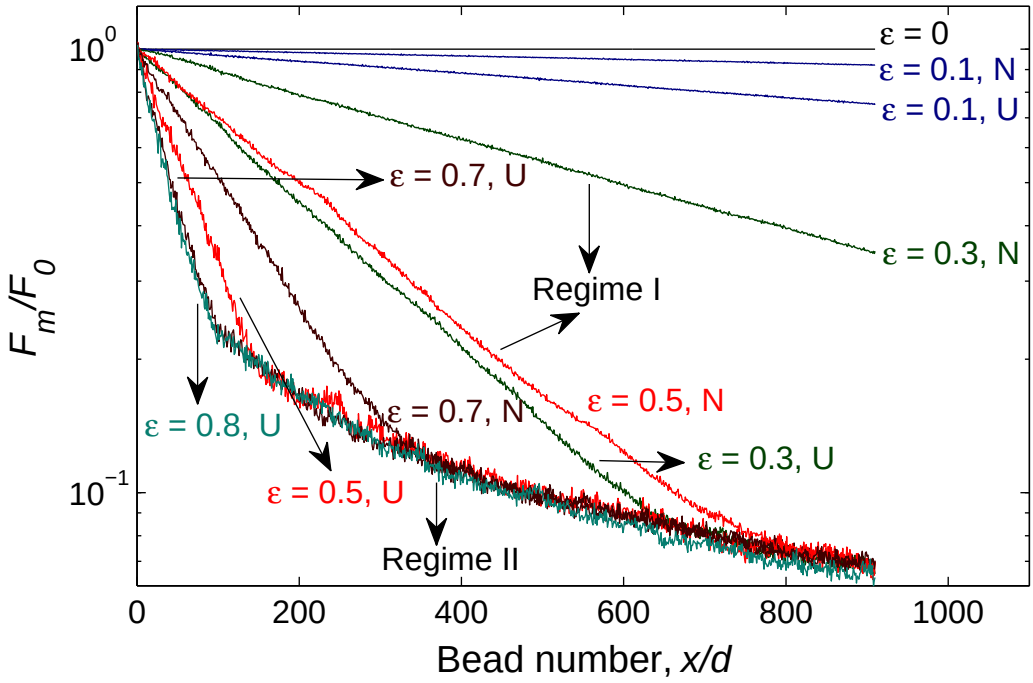

Figure 2.2: The spatial distribution of the peak compressive force (normalized by the amplitude F_0 of the incident solitary wave) for uniform (U) and normal (N) distributions with impact velocity V_0 = 1 m/s for various degrees of randomness ε, showing two regimes of decay: exponential (regime I) and power-law (regime II).

The transition from the exponential regime to the power-law regime occurs when the amplitude of the leading pulse reduces below that of the scatter, as evident in Fig. 2.1(a)(iv) and Fig. 2.1(b). This implies that the regime II, i.e., the power-law decay, is governed entirely by the propagation of the scatter instead of the leading pulse since we are monitoring the force amplitude of the scatter. As shown in Fig. 2.1(a)(v) and Fig. 2.1(b), the leading pulse is sustained for a short period of time after its amplitude decays below that of the scatter. During this short period, it continues to decay exponentially before merging with the scatter. We observe that the transition occurs earlier for cases with high randomness because the leading pulse decays faster, rapidly leading to its disappearance. We can obtain the distance, $x_0(\varepsilon)$, at which transition occurs by equating the forces in the two regimes, leading

to

$$x_0(\varepsilon) = -\frac{\beta_F}{\alpha_F(\varepsilon)} W\left(-\frac{\alpha_F(\varepsilon)\,(F_{01}/F_{02})^{-1/\beta_F}}{\beta_F}\right), \tag{2.4}$$

where W is the Lambert W function (or product log function) [59].

2.2.2 Decay of the maximum kinetic energy

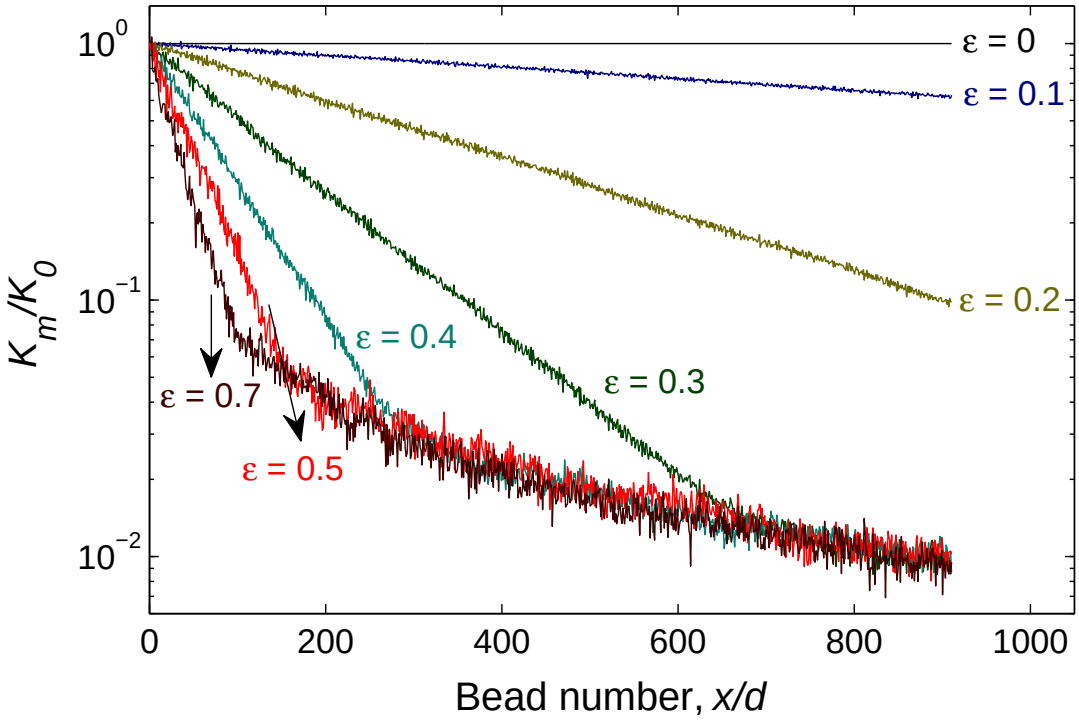

Figure 2.3: Normalized maximum kinetic energy versus bead number for impact velocity $V_0 = 1$ m/s and different degrees of randomness ε, showing the two regimes described in Fig. 2.2. The fluctuations around the mean decay are greater for maximum kinetic energy than for the peak force because of the energy-force scaling.

In Fig. 2.3, we present the maximum kinetic energy (KE) distribution (K_m), normalized by the maximum KE in the nonrandom sub-chain (K_0), and we note that the decay is similar to that of the peak compressive force (Fig. 2.2). From Fig. 2.2 and Fig. 2.3, we observe that the transition from regime I to regime II occurs at the same distance, implying that the maximum KE and the peak compressive force of the solitary wave reduce below that of the scatter at the same distance. Figure 2.3 also

suggests that the amplitude of the fluctuations around the mean decay is greater in the case of the maximum KE than for the peak compressive force, especially in the power-law regime. These two effects arise from the scaling relation between the kinetic energy and the force, given by $K \propto F^{5/3}$ [3]. As before, denoting the decay parameters in the maximum KE for regime I and regime II as α_K and β_K, respectively, we can then write the maximum KE in the corresponding regimes as $K_m(x) = K_{01}exp[-\alpha_K(\varepsilon)x]$ and $K_m(x) = K_{02}x^{-\beta_K}$. The constants K_{01} and K_{02} scale with the corresponding constants (F_{01} and F_{02}) in the force amplitude. Substituting these expressions in the scaling law, we obtain the following relations for α_K and β_K:

$$\alpha_K(\varepsilon) = \frac{5}{3}\alpha_F(\varepsilon), \qquad \beta_K = \frac{5}{3}\beta_F. \tag{2.5}$$

In our simulations, we find the power-law decay parameter, β_F, to be approximately 0.57, which is close to the 0.6 value predicted in [44] for high disorder. In that study, the value was derived theoretically by assuming the energy to be equally distributed among all the spheres. However, in our study, the distribution of the total energy, defined as the sum of potential and kinetic energies, is not uniform across the beads, as the beads close to the advancing pulse shared more energy than those far behind the pulse. This behavior is depicted in Fig. 2.4, where we consider the total energy distribution for $\varepsilon = 0.8$ at an instant when the leading pulse (in this case, scatter) is well into the power-law regime. Although Fig. 2.4 does not agree with the predictions in [44], we expect the assumption of uniform distribution of energy (high delocalization) to hold after a sufficiently long time as attenuation continues to occur.

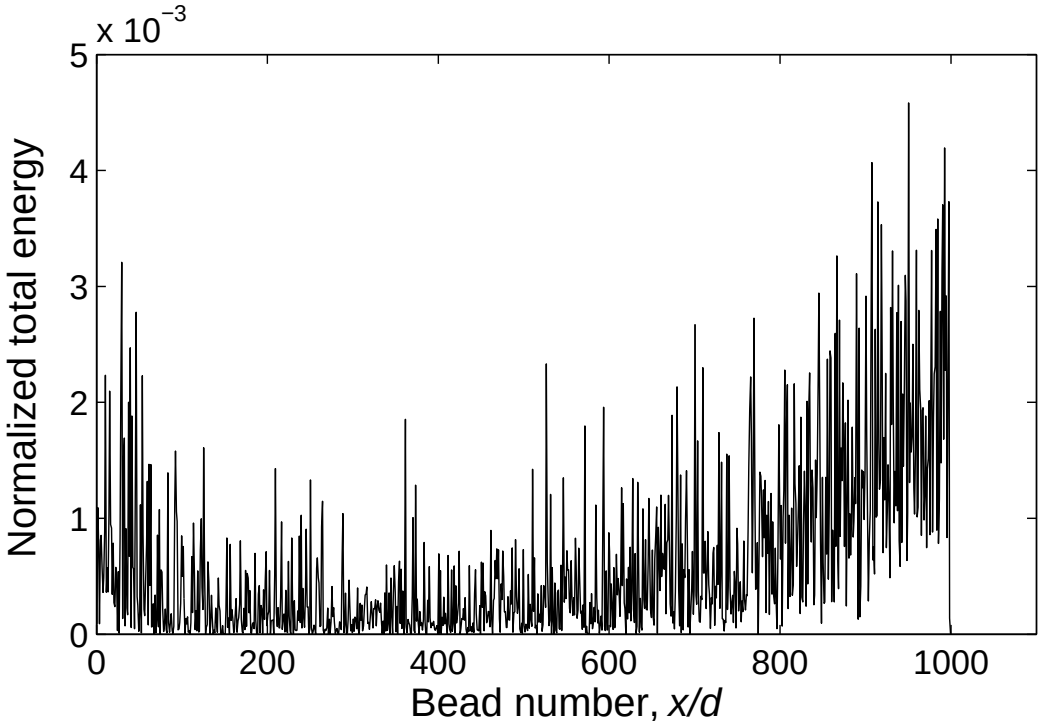

Figure 2.4: Total energy (sum of potential and kinetic energies), normalized by the impact energy, as a function of distance for $\varepsilon = 0.8$ at a time when the leading pulse is well into the power-law regime.

Figure 2.5 shows the ε-dependence of the regime I decay parameters α_F and α_K of the peak compressive force and the maximum KE, respectively. The data is presented for both uniform and normal distributions, with ε ranging from 0 to 0.9. Here the decay parameters exhibit quadratic dependence [43] up to a certain ε, referred to hereafter as the critical randomness (ε_c), beyond which the parameters approach a plateau. For large ε, the system is insensitive to the heterogeneities present and thus does not depend on the level of disorder (Fig. 2.2), leading to an approximately constant value. For high randomness ($\varepsilon > \varepsilon_c$), the system quickly reaches a state where the propagation is governed by the scatter [Fig. 2.1(e)]. However, to reach this state, the system requires a certain number of beads to saturate, and hence the constant decay rate. The saturation is not observed in the case of normal distribution because, for the system considered, the decay is sufficiently lower than

that of uniform distribution. The decay parameters from Fig. 2.5 and the power-law decay parameters extracted by fitting power-law curve in Fig. 2.2 (β_F) and Fig. 2.3 (β_K) agree well with the relations in Eq. (2.5). In Section 2.2.5, we present another procedure for characterizing and predicting the critical randomness using energy concepts associated with the virial theorem.

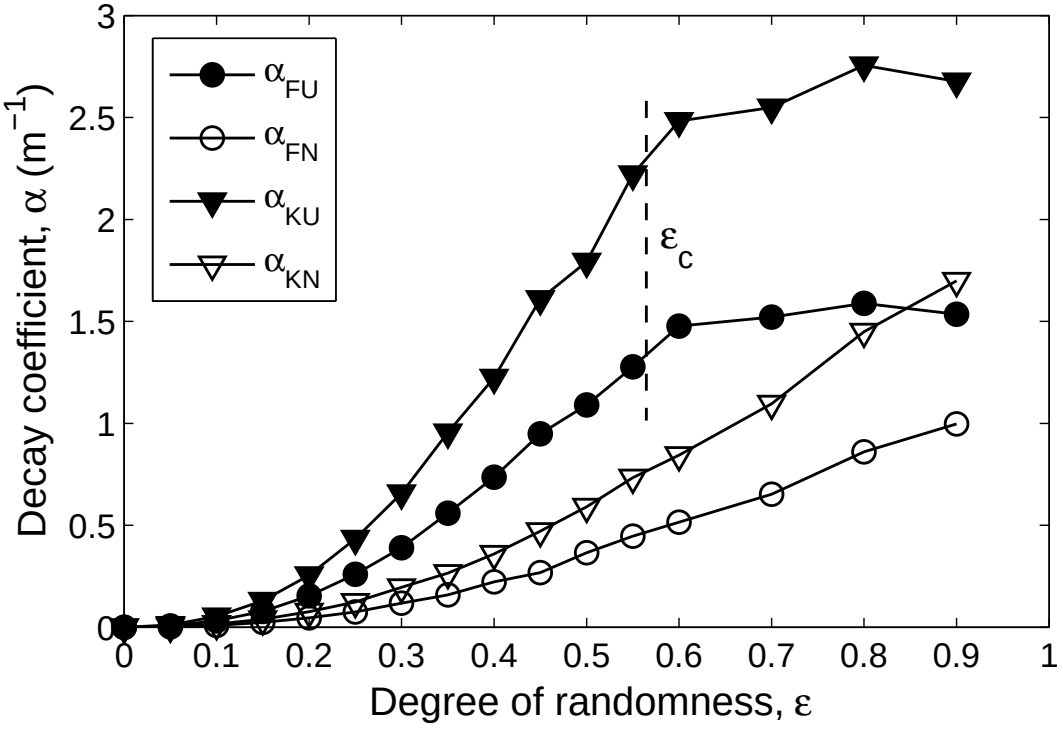

Figure 2.5: The decay parameters (α_F and α_K) as a function of ε for uniform (α_{FU} and α_{KU}) and normal (α_{FN} and α_{KN}) distributions. The dotted line corresponds to the critical randomness (ε_c), beyond which the decay is approximately a constant for the uniform distribution.

2.2.3 Normalization of response over different impact velocities and Young's moduli

The scaling relation between the force amplitude (F_m), particle velocity (v_i) and Young's modulus (E) can be derived using dimensional analysis [3]. The equation of motion provides a scaling law between the length (L), time (T) and Young's

modulus as

$$\frac{L}{T^2} \propto EL^{3/2} \implies L \propto E^{-2}T^{-4}. \tag{2.6}$$

Noting that the particle velocity scales as L/T, the phase velocity (V_s) scales as $1/T$, and using the above scaling law, we obtain

$$v_i \propto \frac{L}{T} \propto E^{-2}T^{-5} \implies V_s \propto \frac{1}{T} \propto E^{2/5}v_i^{1/5}. \tag{2.7}$$

Finally, using the force equation for Hertzian contacts, we get

$$F_m \propto EL^{3/2} \propto E^{-2}T^{-6} \propto E^{2/5}v_i^{6/5}. \tag{2.8}$$

Since the impact velocity (V_0) scales with the particle velocity (v_i), the above relation can be employed to obtain the ratio of the peak forces associated with two different values of V_0 (V_{01} and V_{02}):

$$\frac{F_{m_2}}{F_{m_1}} = \left(\frac{V_{02}}{V_{01}}\right)^{6/5}. \tag{2.9}$$

We illustrate the normalization in Fig. 2.6, where we present the peak force distribution for V_0 = 10 m/s normalized by that of V_0 = 1 m/s with ε = 0.3 and ε = 0.9. We then calculate the mean for each ε in the range of 0.1 to 0.9, and the average of all the means is found to be 15.87, in good agreement with Eq. (2.9). In Fig. 2.6, we note that the statistical variation not only depends on the degree of randomness but also on the regime in which the bead is present. The deviation can be particularly observed for the case of ε = 0.3, where, after the point of transition (bead number 650), the deviation increases to the order of ε = 0.9.

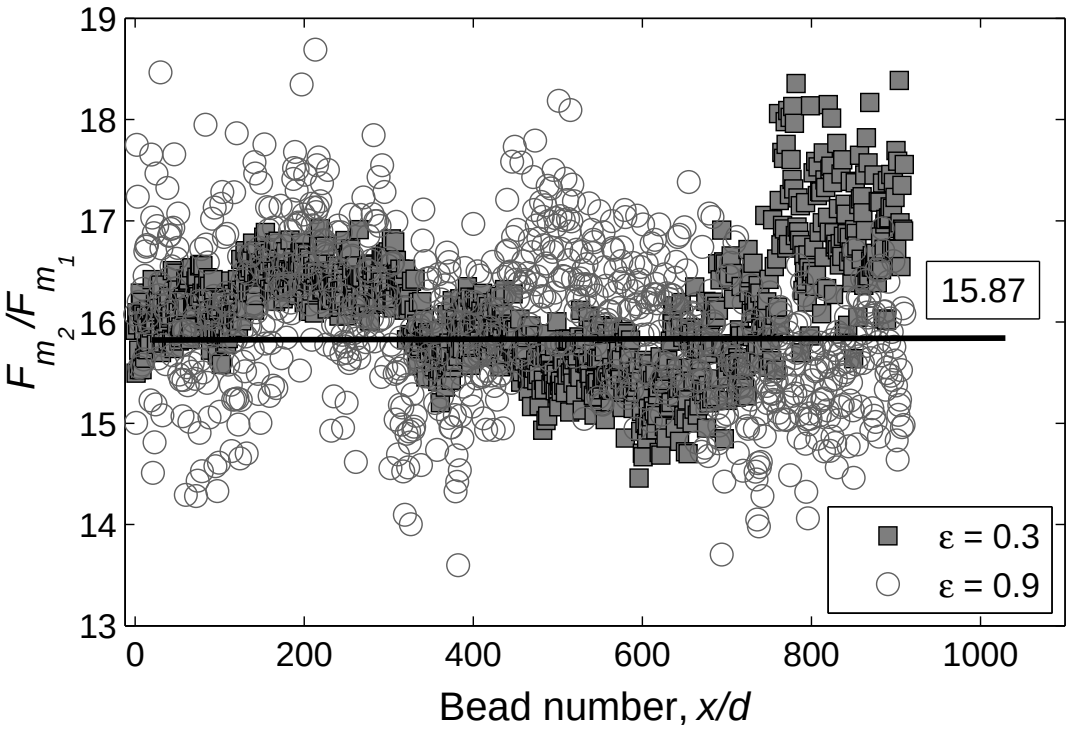

Figure 2.6: Peak compressive force distribution for V_0 = 10 m/s (F_{m_2}) normalized by the corresponding peak force obtained with V_0 = 1 m/s (F_{m_1}) for two values of ε. The horizontal line denotes the average value.

Equation (2.8) can also be used to obtain the normalization with respect to Young's modulus:

$$\frac{F_{m_2}}{F_{m_1}} = \left(\frac{E_2}{E_1}\right)^{2/5}. \tag{2.10}$$

The above procedure can be extended to study the normalization behavior for any of the parameters stated in Section 2.1.

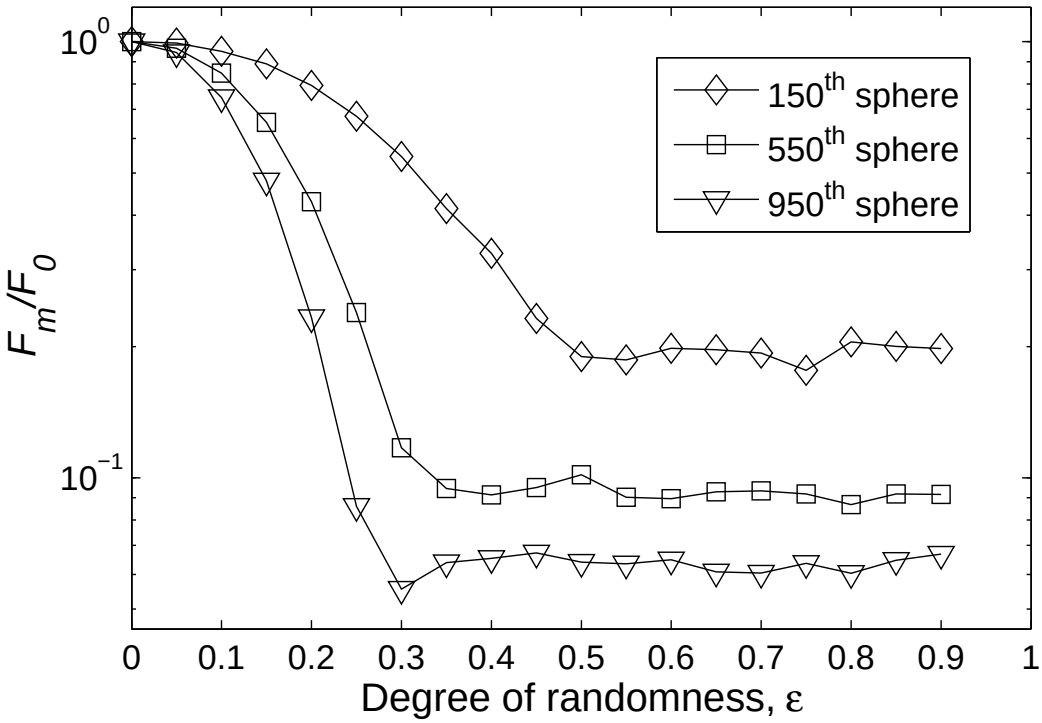

Figure 2.7: The ε-dependence of the peak force for three beads in the random chain.

Figure 2.7 shows the ε-dependence of the peak force (averaged over 10 realizations), normalized by the peak force in the nonrandom chain, for three beads in the random chain (uniform distribution). The figure indicates that the peak force initially decreases with increase in randomness and reaches a plateau after a certain ε. This confirms the earlier observation that the regime II of power-law dependence is the same for any level of randomness (Fig. 2.2). Thus, we note that the plateau is reached earlier as we proceed along the chain.

2.2.4 Evolution of the force amplitude

The force decay relations described in Section 2.2.1 can be combined with the classical relation between phase velocity V_s and force amplitude F_m obtained for a

monodisperse nonrandom chain [12],

$$V_s = 0.68\left(\frac{E_0}{R_0\rho_0^{3/2}(1-\nu_0^2)}\right)^{1/3} F_m^{1/6} = AF_m^{1/6}, \tag{2.11}$$

to derive the expected location of the main compressive pulse and the time evolution of the force amplitude in the random chain. For regime I characterized by an exponential decay, we get [43]

$$x_1(t) = \frac{A}{B}\ln\left(1 + BF_{01}^{1/6}t\right), \tag{2.12}$$

where $B(\varepsilon) = \alpha_F(\varepsilon)A/6$. Equation 2.12 can be used to obtain the force amplitude as a function of time, leading to

$$\frac{F_{m1}(t;\varepsilon)}{F_{01}} = \left[1 + B(\varepsilon)F_{01}^{1/6}t\right]^{-6}. \tag{2.13}$$

In regime II, where $F_{m2} = F_{02}x^{-\beta_F}$, one gets

$$\frac{x_2(t)}{x_0} = \left[1 + (1+\beta_F/6)AF_{02}^{1/6}x_0^{-1-\beta_F/6}(t-t_0)\right]^{1/(1+\beta_F/6)}, \tag{2.14}$$

where x_0 is the distance at which transition occurs [Eq. (2.4)] and t_0 is the corresponding time obtained from Eq. (2.12) with $x_1(t_0) = x_0$. In that regime, the time evolution of the force amplitude is

$$F_{m2}(t;\varepsilon) = \left[\gamma_F C(t-t_0) + \left(B(\varepsilon)t_0 + F_{01}^{-1/6}\right)^{6\gamma_F}\right]^{-1/\gamma_F}, \tag{2.15}$$

where $\gamma_F = 1/6 + 1/\beta_F$ and $C = A\beta_F F_{02}^{-1/\beta_F}$.

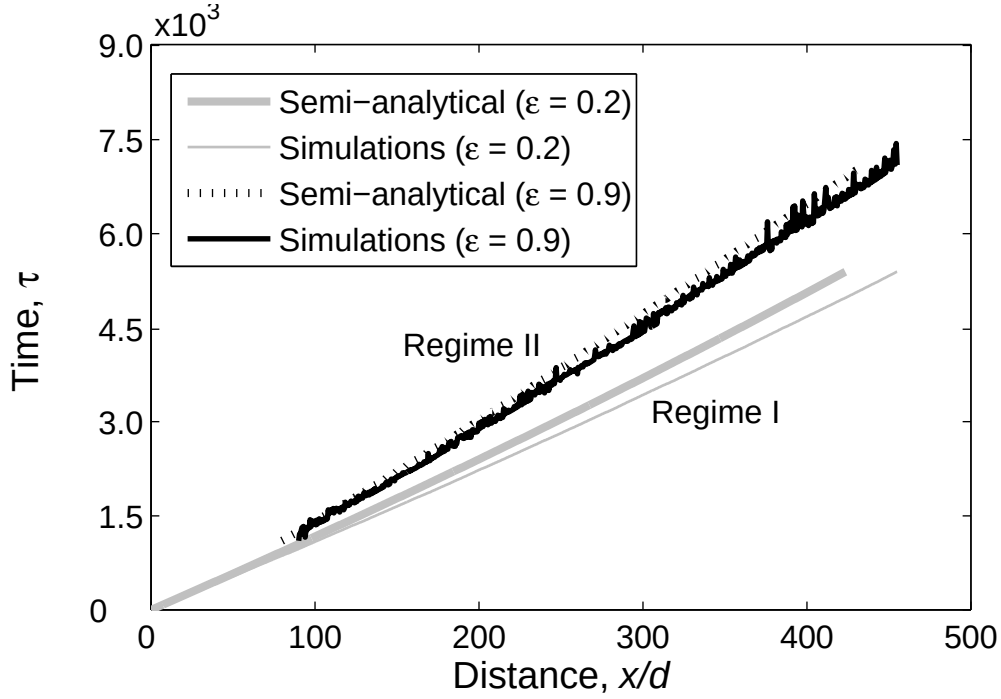

(a)

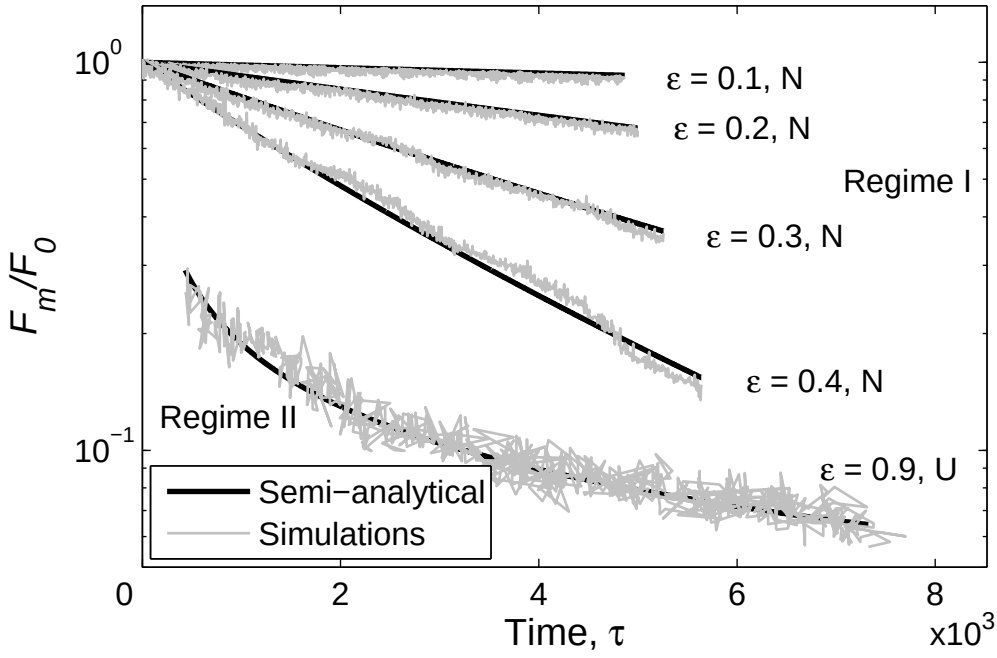

(b)

Figure 2.8: (a) Normalized time ($\tau = (k_0 \sqrt{R_0}/m_0)^{1/2} t$) of arrival of the wave (defined by the force amplitude) for two values of ε: comparison between semi-analytical predictions [Eqs. (2.12) and (2.14)] and numerical values. (b) Semi-analytical predictions [Eqs. (2.13) and (2.15)] and numerical results for the evolution of the force amplitude for various values of ε, showing the progressive temporal decay associated with the two regimes.

Figure 2.8(a) shows the evolution of the location of the pulse for $\varepsilon = 0.2$ (regime I) and $\varepsilon = 0.9$ (regime II). A slight deviation is observed for the regime I solution due to the small (7%) difference between analytical [Eq. (2.11)] and numerical values of the coefficient A, as noted in [51]. If, as it is the case in [43], we adopt the numerical value for the phase velocity of the nonrandom chain, a closer match is obtained in Fig. 2.8(a) between semi-analytical and numerical values. In Fig. 2.8(b), we present the variation of the amplitude of the peak force with time for $\varepsilon = 0.1$ to $\varepsilon = 0.4$ in regime I, and for $\varepsilon = 0.9$ in regime II. We find a very good agreement between the semi-analytical expressions [Eqs. (2.13) and (2.15)] and the simulation results. We adopt here the term *semi-analytical* because we do not have an explicit expression for α_F as a function of ε, although we know the behavior to be approximately quadratic (Fig. 2.5). A closer look into Fig. 2.8(b) reveals the decreasing nature of the speed of the impulse with increase in randomness, as suggested by the time at which the pulse reaches a particular location.

2.2.5 Distribution of energy during wave propagation

The dynamic system can be described by the evolution of the ensemble kinetic (potential) energy which is defined as the sum of the kinetic (potential) energies of all the beads at a particular time. In Fig. 2.9, we present the variation of the ensemble kinetic and potential energy with time for varying ε, normalized with the initial ensemble energy, which is equal to the impact kinetic energy of the first bead. Note that, since the system is conservative, the total ensemble energy, i.e., the sum of ensemble kinetic and potential energies, is equal to the impact kinetic energy throughout the simulation. In the nonrandom segment (denoted by A in Fig. 2.9), we note that the solitary wave is established very quickly, and that the ensemble kinetic and potential energies oscillate around a mean value as shown by

the inset of Fig. 2.9. However, when the wave enters the random segment, the energy components deviate from the mean. Since the ensemble kinetic (potential) energy includes the corresponding energy of the nonrandom chain as well, we observe a small transient region (denoted by B in Fig. 2.9) near the interface. Beyond the region *B*, with further increase in time, the ensemble kinetic energy increases due to the impedance mismatch at inter-particle contacts. This progressive increase in kinetic energy is accompanied by a corresponding decrease in ensemble potential energy, which reflects the progressive decay of the inter-particle contact forces. The rate of this progressive transfer from potential to kinetic energy increases with increase in ε.

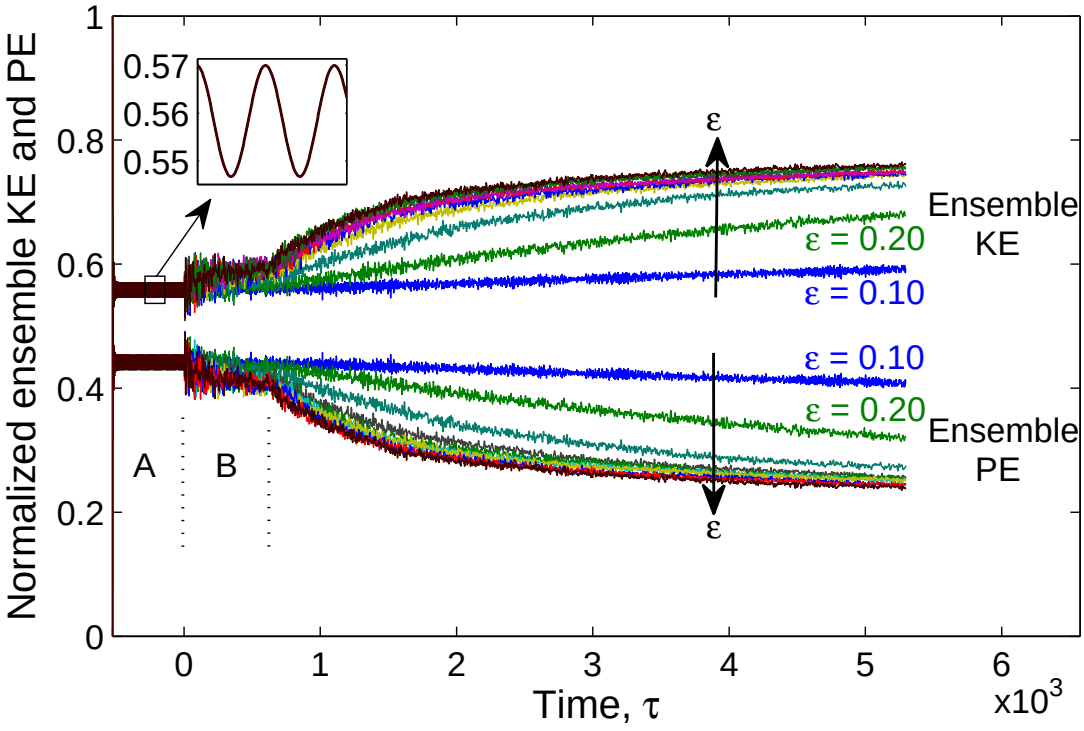

Figure 2.9: Evolution of the ensemble kinetic and potential energies for various degrees of randomness (ε) in particle mass. The inset shows the oscillations of ensemble KE as the solitary wave propagates in the nonrandom chain ($\tau < 0$). The evolution in the random chain shows the progressive transfer of energy from potential to kinetic energy.

The mean values of the ensemble kinetic and potential energies obtained in

the nonrandom segment can be compared with the values predicted by the virial theorem, which states that, for a stable system of N particles interacting via the potential $V = a\delta^n$, the time-averaged ensemble kinetic energy is equal to $n/2$ times the time-averaged ensemble potential energy. For the nonrandom system, the mean value of the oscillations is taken to be the time-averaged value. For conservative systems interacting via the Hertzian potential, $n = 5/2$. The virial theorem therefore suggests that the time-averaged kinetic and potential energies represent 5/9 and 4/9 of the total impact energy, respectively. The corresponding values obtained from simulations are 0.5583 and 0.4416, which agree very well with the virial theorem predictions [5].

To apply the virial theorem to the random chain, we define the total kinetic (potential) energy as the sum of the ensemble kinetic (potential) energies over all time steps. Consider the virial G defined as [60]

$$G(t) = \sum_{i=1}^{N} p_i(t) r_i(t) = \sum_{i=1}^{N} m_i v_i(t) r_i(t), \tag{2.16}$$

where N is the number of beads in the chain, while $p_i(t)$ and $r_i(t)$ are the momentum and position vector of the i^{th} bead, respectively. Taking the time-averaged value over the interval $[0, \tau]$ of the time derivative of the virial (Eq. 2.16), and applying to Hertzian interaction yields

$$\begin{aligned}\left\langle \frac{dG}{dt} \right\rangle_\tau &= \frac{G(\tau) - G(0)}{\tau} \\ &= \frac{2}{\tau} \int_0^\tau \left(\sum_{i=1}^{N} \frac{1}{2} m_i v_i^2 \right) dt - \frac{5}{2\tau} \int_0^\tau \left(\sum_{i=1}^{N} \sum_{j<i} V_{ij} \right) dt,\end{aligned}$$

where V_{ij} is the potential energy of inter-particle interaction. Simplifying the above expression by denoting $G(\tau)$ as G_τ, $\sum_{i=1}^{N} (1/2) m_i v_i^2$ at the k^{th} time step as $T^{(k)}$,

$\sum_{i=1}^{N} \sum_{j<i} V_{ij}$ at the k^{th} time step as $V^{(k)}$, and discretizing the integrals, we get

$$\frac{G_\tau}{\Delta t} = 2\sum_{k=1}^{M} T^{(k)} - \frac{5}{2}\sum_{k=1}^{M} V^{(k)}, \tag{2.17}$$

where Δt denoted the time step. Since the impact energy (C) is conserved at every time step, we have $T^{(k)} + V^{(k)} = const. = C$ for any k^{th} time step. Denoting $\sum_{k=1}^{M} T^{(k)}$ as T_{sum} and $\sum_{k=1}^{M} V^{(k)}$ as V_{sum}, we obtain $T_{sum} + V_{sum} = MC$. The expressions for T_{sum} and V_{sum} are then

$$T_{sum} = \frac{1}{9}\left(5MC + \frac{2G_\tau}{\Delta t}\right), \tag{2.18}$$

$$V_{sum} = \frac{1}{9}\left(4MC - \frac{2G_\tau}{\Delta t}\right), \tag{2.19}$$

where $\tau = M\Delta t$.

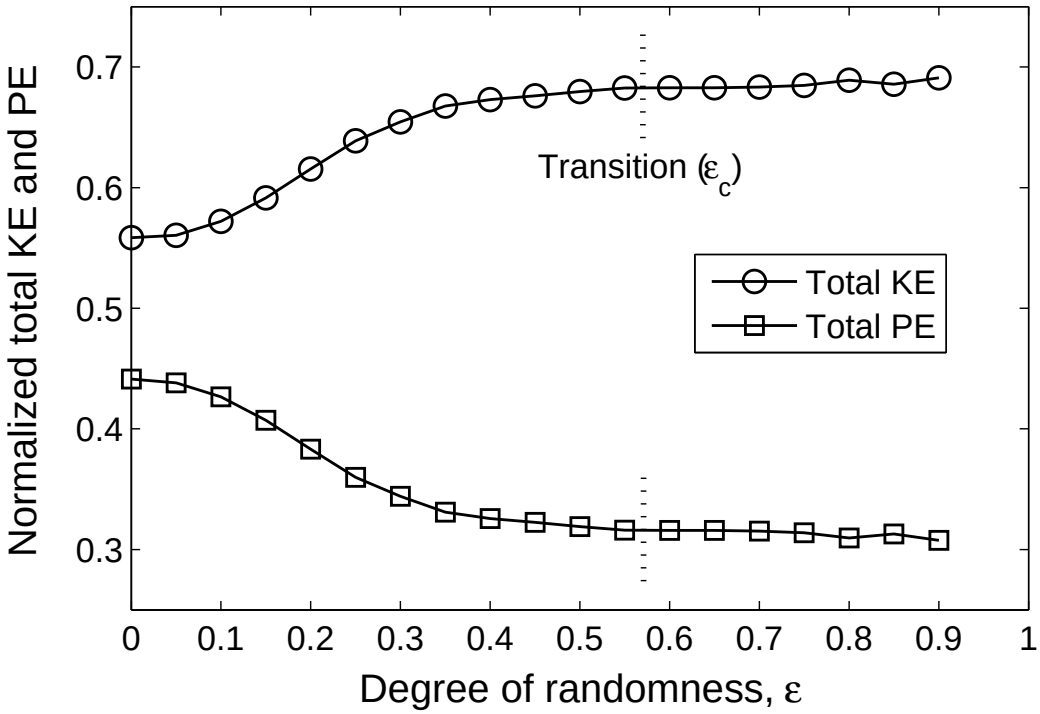

Figure 2.10: The total kinetic and potential energies, defined as the sum of the ensemble energies, normalized by the sum of the total energies for $\varepsilon = 0$, as a function of degree of randomness (ε) for a uniform distribution, showing the transition to the approximately constant values.

The ε-dependence of T_{sum} and V_{sum} obtained numerically is presented in Fig. 2.10 for a constant value of M corresponding to the time of travel of the solitary wave through a 1100-particle nonrandom chain. The results suggest that the total kinetic and potential energies reach a constant value after a certain degree of randomness, as highlighted by the dotted line. This transition pertains to the critical randomness defined earlier (Fig. 2.5), as the region right of the dotted line is insensitive to the level of randomness. Equations (2.18) and (2.19) suggest that the transition solely depends on the virial (G_τ) since it is the only parameter that depends on ε. The equations also include the source of the transfer of energy from potential to kinetic with increase in randomness, as indicated by the positive and negative signs in T_{sum} and V_{sum}, respectively. As the randomness increases, the transition from

exponential to power-law occurs earlier, and thus the power-law regime dominates after the critical randomness.

2.3 Randomness in Young's modulus and radius

In this section, we start by studying the effect of randomness in Young's modulus on the wave attenuation, and compare the response with that of randomness in mass developed earlier. Randomness is incorporated in Young's modulus using a similar law to that used earlier, i.e., $E_i = E_0(1 + r_i\varepsilon)$, where E_0 is the mean Young's modulus. With all the properties kept the same (with the mass of each bead denoted by m_0), randomness in Young's modulus affects the nonlinear spring constant for adjacent beads defined in Section 2.1. In Fig. 2.11, we show the spatial attenuation of the peak force for different levels of randomness in Young's modulus superimposed on the results obtained earlier for randomness in mass (underlined). We observe similar decay regimes: exponential and power-law. The decay parameter in regime I (α_F) is found to be greater than that obtained with mass randomness for the same value of ε, while the regime II decay (β_F) is approximately the same for the two cases.

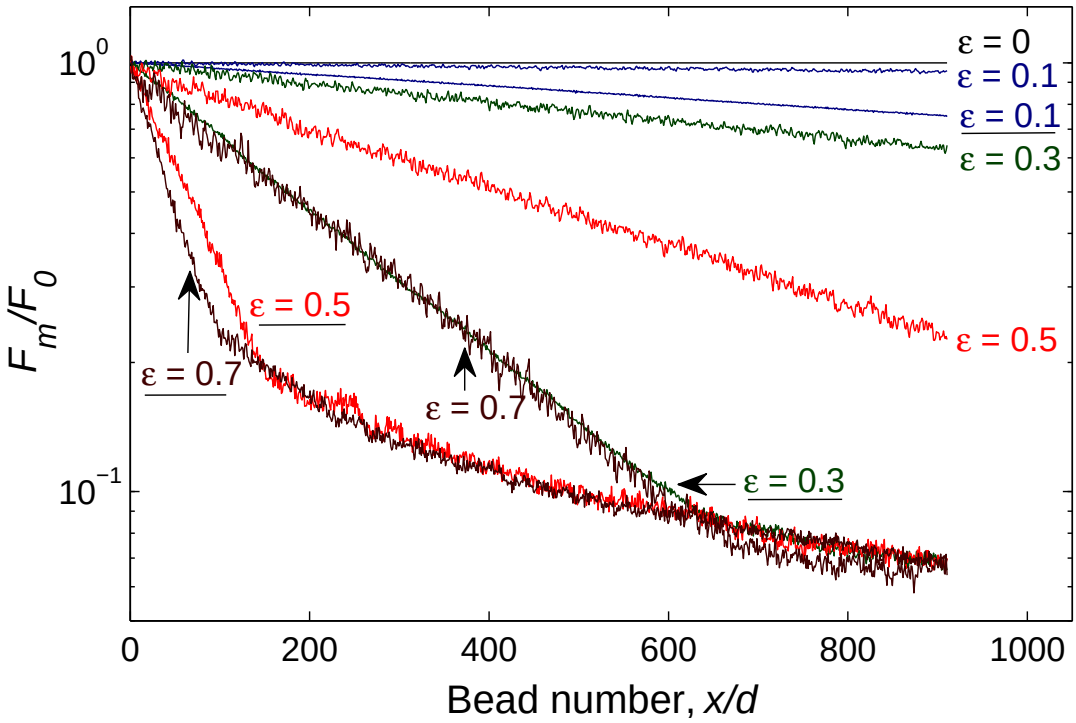

Figure 2.11: The peak compressive force distribution for randomness in Young's modulus superimposed over that for randomness in mass. ε ranges from 0.1 to 0.7 with results of mass randomness labeled with underline. Randomness in Young's modulus leads to a lower decay compared to that in mass.

To conclude this study, we investigate the spatial attenuation due to the presence of randomness in radius. For a constant density, introducing randomness in the size of the particles leads to randomness in both the particle mass and the inter-particle contact stiffness. As before, randomness in radius is implemented using $R_i = R_0(1 + r_i\varepsilon)$, where R_0 is the mean radius. In Fig. 2.12, we show the spatial attenuation of the peak force for this case superimposed with that of randomness in mass, showing a decay which is substantially higher. As was observed in Fig. 2.11, the two decay regimes are evident with the regime II having approximately the same decay parameter as that of randomness in mass or Young's modulus.

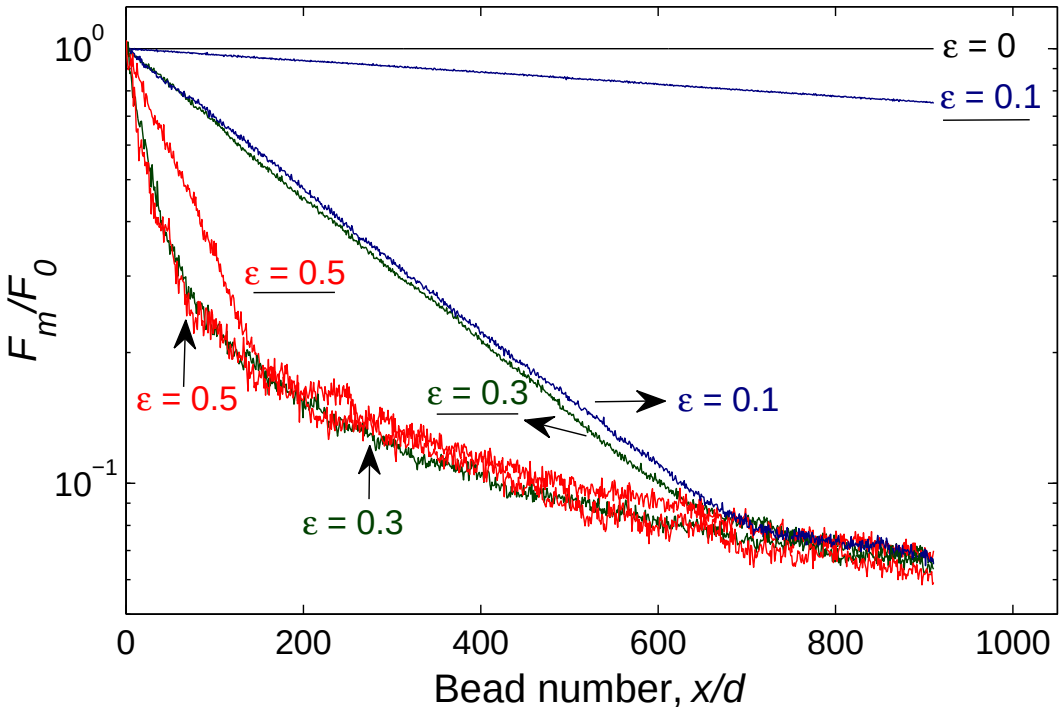

Figure 2.12: Spatial variation of the peak force for randomness in radius compared with the results of mass randomness (labeled with underline).

Figure 2.13 shows the ε-dependence of the regime I decay parameter α_F for different sources of randomness (mass, Young's modulus and radius), showing in all cases a quadratic dependence for smaller values of ε. We also note that randomness in radius leads to a higher decay rate in the pulse amplitude and hence the critical randomness (ε_c) occurs much earlier compared to the other two sources. Since the transition to the power-law regime also occurs earlier, α_F is difficult to predict accurately for large ε. For the case of randomness in Young's modulus, the critical randomness does not appear owing to its slower rate of decay.

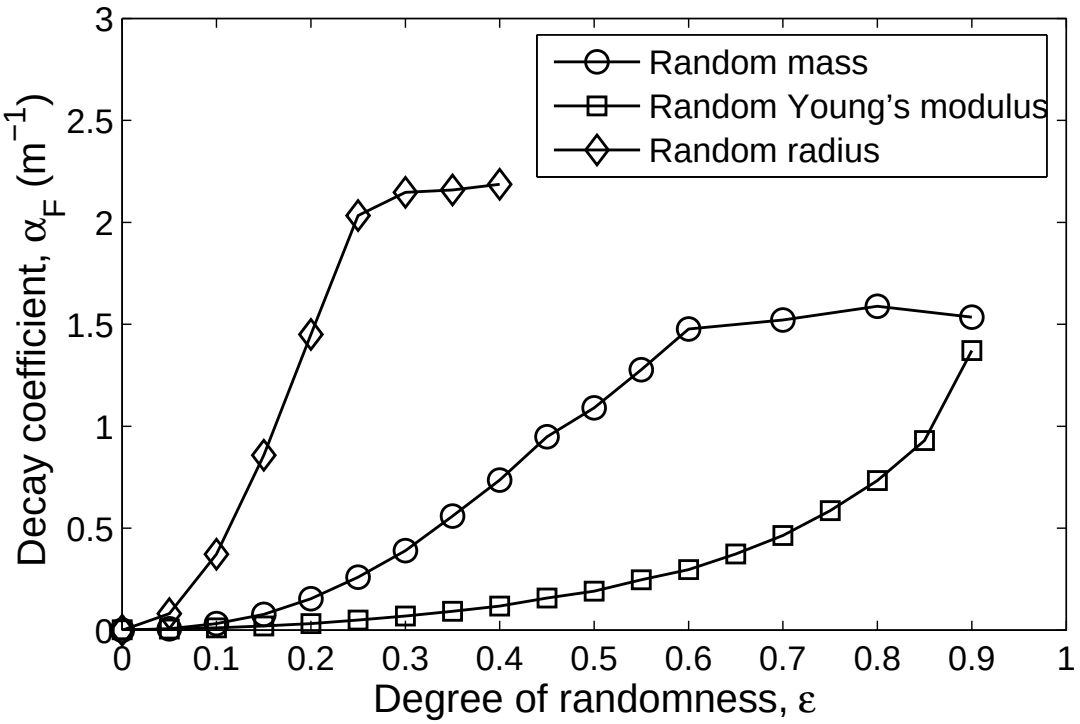

Figure 2.13: Decay parameter α_F as a function of ε for randomness in mass, Young's modulus and radius for uniform distribution, showing the highest rate of decay for randomness in radius.

2.4 Conclusions

The effect of randomness on wave propagation in 1D chains of granular media interacting via the Hertzian potential was investigated numerically. Randomness was introduced separately in the masses, Young's moduli and radii of the particles using uniform and normal distributions. The simulations revealed the presence of two distinct regimes of decay in force amplitude and maximum kinetic energy. The first regime is characterized by an exponential decay with the decay coefficient strongly dependent on the degree of randomness. The second regime is well described by a power law and dominates the propagation response for a wide range of randomness. The decay in the power-law regime is independent of the level of randomness. The study also demonstrated the formation of a 'silent' region behind

the leading pulse, and was found to disappear for sufficiently long chains. Semi-analytical expressions were derived for the evolution of the force amplitude in the two regimes by combining the extracted decay coefficients with the expression of the phase velocity of the wave derived for a nonrandom chain with the same average properties. Investigation into the energetics of random granular chains showed that there is a progressive transfer of energy from potential to kinetic energy and the rate of transfer increases with increase in randomness. The application of the virial theorem to the random system led to the characterization of the critical randomness beyond which the system no longer depends on the randomness. The attenuation characteristics of force amplitude showed that randomness in radius led to a considerably higher decay than the other two sources of randomness. However, force response occurring in the power-law decay regime was essentially identical in systems having randomness in mass, Young's modulus or radius.

Chapter 3

Randomness in 2D granular media

The work presented in this chapter is an extension of the aforementioned study on 1D granular chains (Chapter 2), as we perform numerical simulations on wave propagation in a square packing of spheres with smaller spheres at interstitial locations. The current study focuses on single pulse-like impact events on granular structures without precompression. Randomness is incorporated in densities of the spheres using a uniform distribution. Randomness in Young's modulus will have a qualitatively similar response as discussed in Chapter (2) but, unlike 1D systems, randomness in radius may lead to a different response due to the presence of gaps and misalignments in the 2D packing [55]. The goal is to study the similarities and differences between wave propagation in 2D and 1D random granular media. One of the key questions is to determine whether the regimes of decay are similar to those reported in 1D random chains in Chapter (2). Unlike 1D chains, 2D systems introduce a component of decay due to dimensionality, which is found to closely follow a power law. Decay in force due to randomness alone is isolated by normalizing it with the decay of the force in the nonrandom system. Here too we notice similar decay regimes as in 1D chains, i.e., exponential and power law. A continuum representation of the system is obtained through linear interpolation for characterizing the decay along different directions. The isotropy or anisotropy of the force distribution is also analyzed and quantified which is critical for creating optimized material designs for tailoring force propagation. Furthermore, contour representations of peak force show that the decay transitions from anisotropic to

isotropic for large distances or high randomness.

The chapter is organized as follows: Section 3.1 provides the problem definition, the setup used in the simulations and the relevant parameters. In Sec. 3.2.1, snapshots of wave propagation are illustrated for different levels of randomness, and a brief discussion on the shape of the wavefront is presented. Section 3.2.2 demonstrates the force amplitude distribution for granular systems with varying randomness, and characterizes the force amplitude evolution over the entire range of propagation. In Sec. 3.2.3, contours of peak force distribution in the whole domain are presented to analyze the isotropy or anisotropy of the wave propagation and the peak force variation along different directions is quantified. In Sec. 3.2.4, the computed evolution of energy components is compared with the virial theorem and with the corresponding response of 1D random granular chains. The results of the above study has been published in *Physica D: Nonlinear Phenomena* ("Wave propagation in 2D random granular media." *Physica D: Nonlinear Phenomena* 266 (2014): 42-48) and the remainder of this chapter follows that publication.

3.1 Problem definition

We model a 2D square packing system of elastic spheres with intruders located at interstitial positions as shown in Fig. 3.1. The radius of an intruder is chosen such that the neighboring spheres are in contact with zero precompression. The ratio of the radius of the smaller spheres (R_s) to that of the larger spheres (R_b) is thus $\sqrt{2}-1$. The Hertzian contact law [4] is used to calculate the force on the spheres under compression. The equations of motion for sphere i of mass m_i with N_i neighboring contacts are written as

$$m_i \ddot{\mathbf{u}}_i = \sum_{j=1}^{N_i} \mathbf{F}_{j,i}, \tag{3.1}$$

where the amplitude of the contact force between spheres i and j is given by $\left|\mathbf{F}_{j,i}\right| = k_{i,j} \langle\delta\rangle_{j,i}^{3/2} = (4/3)E_{i,j}^{*} \sqrt{R_{i,j}^{*}} \langle\delta\rangle_{j,i}^{3/2}$ and is directed along the line joining the centers of the two spheres. The parameters in these relations were defined in Sec. 2.1. Dissipation effects, including friction, are neglected.

Randomness is introduced in the masses of both larger (m_b) and smaller (m_s) spheres according to the following relation (similar to Eq. (2.2)):

$$m_i = m_0(1 + r_i\varepsilon), \tag{3.2}$$

where m is m_b or m_s. The mean mass ratio of the spheres (m_{0s}/m_{0b}) is calculated using a density ratio (ρ_{0s}/ρ_{0b}) equal to one. The ratios of Young's moduli (E_s/E_b) and Poisson's ratios (ν_s/ν_b) are also taken equal to one. In the simulations, the material and geometric properties of the larger spheres are as follows: radius $R_b = 5$ mm, mean density $\rho_{0b} = 7850$ kg/m^3, Young's modulus $E_b = 200$ GPa and Poisson's ratio $\nu_b = 0.3$. The corresponding values for the smaller spheres are evaluated using the aforementioned ratios.

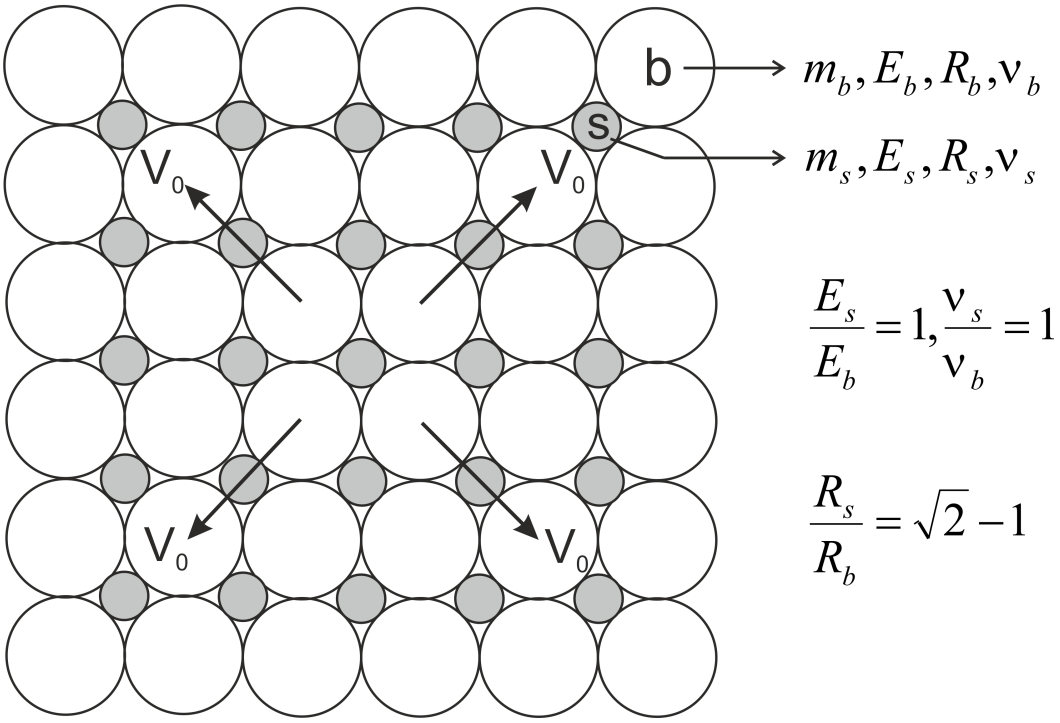

Figure 3.1: 2D setup of spheres investigated in the present study. The interstitial spheres ('s') fit exactly between the larger particles ('b'). The mean mass ratio of the spheres (m_{0s}/m_{0b}) is calculated using density ratio equal to one. The four larger spheres at the center of the packing are given an initial velocity $|\mathbf{V}_0|$ along the diagonal directions as shown.

The molecular dynamics package LAMMPS (Large-scale Atomic/Molecular Massively Parallel Simulator [61]) is employed to simulate the granular system by modeling the spheres as point masses interacting via the nonlinear Hertz potential. LAMMPS was specially adapted for granular media, mainly in the capability to work with different materials. The parallel processing capability of LAMMPS was utilized to simulate the large granular systems considered in the present study.

Since the system is conservative, i.e., the sum of potential and kinetic energies of all the spheres is constant at all times, we use the NVE (i.e., constant number of spheres (N), volume (V) and energy (E) of the system) ensemble option in LAMMPS in all our simulations. The total number of spheres are about $80,000$ (200 by 200 larger spheres, 199 by 199 smaller spheres). The spheres on the boundary are free to

move, but the domain size is large enough to avoid any influence of the boundary. The system is then given a symmetric impact at the center by providing an initial velocity of magnitude $|\mathbf{V}_0| = \sqrt{2}$ m/s to four large spheres along ±45° directions as shown in Fig. 3.1. The total compressive force on each sphere and ensemble kinetic energy at every time step are monitored. The total compressive force is defined by [51]

$$F_i = \sqrt{\left[\sum_{j=1}^{N_i} \left|\mathbf{F}_{x_j}\right|\right]^2 + \left[\sum_{j=1}^{N_i} \left|\mathbf{F}_{y_j}\right|\right]^2}, \tag{3.3}$$

where the summation of absolute values of x or y components of forces is carried over all the neighboring contacts (N_i). In all the simulations, the time step is chosen to be 10^{-8} s.

The presence of randomness inherently introduces variability in the wave propagation response, and the study is conducted over a large sample set (15 simulations yielding 60 realizations) to derive meaningful conclusions. Samples for each degree of randomness are created by generating different set of uniform random numbers (r_i in Eq. 3.2) for different realizations. The results are then averaged over all the realizations for the entire domain. We further take advantage of the symmetric nature of the loading conditions by averaging the previous result over the four quadrants in the domain. Unless mentioned otherwise, all the results presented herein are averaged over fifteen realizations and over the four quadrants, thus yielding a total of sixty realizations. This number of samples was chosen to limit the contact force values on an average to a 2% error bar around their mean values for the worst case scenario, i. e., the most random system ($\varepsilon = 0.9$).

3.2 Results and discussion

3.2.1 Characteristics of wave propagation

Figures 3.2(a)(i)–(iv) show snapshots of total compressive force, taken at t = 1.7 ms, for a typical simulation for ε ranging from 0 to 0.8. For the nonrandom system, as shown in Fig. 3.2(a)(i), the wavefront shape is well defined. We also notice some amount of backscattering behind the leading front due to radius mismatch between larger and smaller spheres. In the presence of randomness in densities [Figs. 3.2(a)(ii)–(iv)], however, the number of secondary (trailing) waves increases, as indicated by the smaller number of spheres with a total compressive force close to zero. There is no clear leading front due to impedance mismatch at contacts associated with randomness. The additional reflections occurring in random systems lead to the decay of the force amplitude. The decaying force also affects the speed of the wave due to the characteristic scaling relation between the force amplitude (F_m) and the speed of the wave (V_s), $V_s \propto F_m^{1/6}$ [22]. As apparent in Figs. 3.2(a)(i)–(iv), this decrease in the wavefront speed increases with randomness.

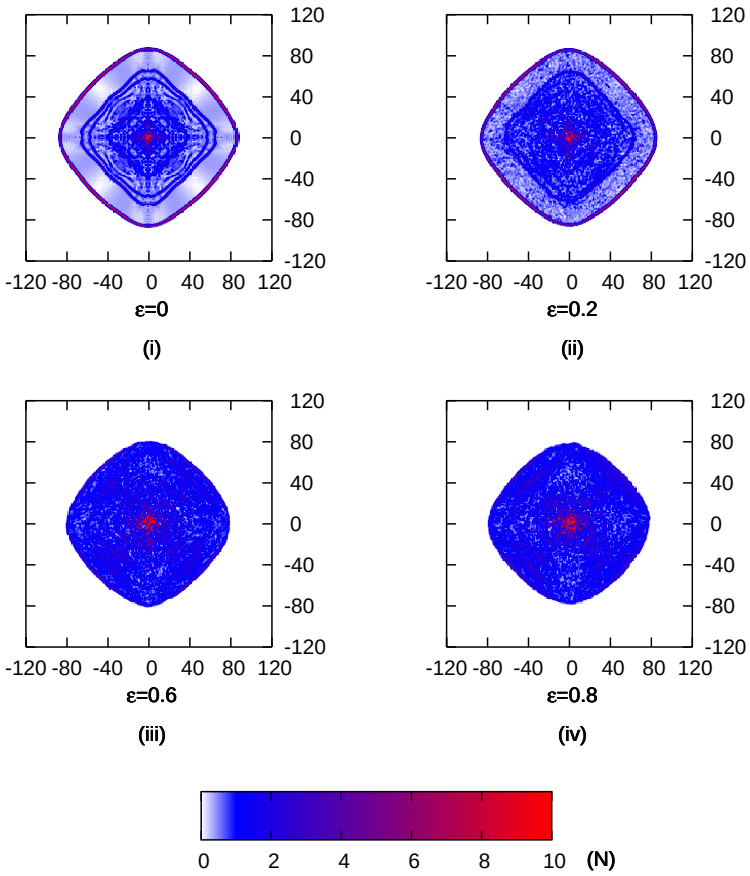

(a)

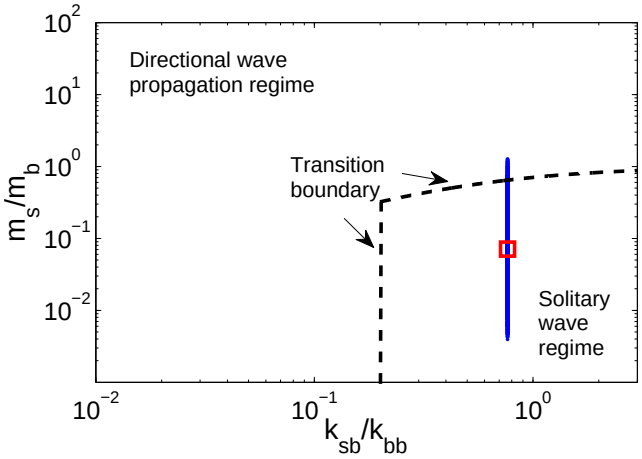

(b)

Figure 3.2: (a) (i)–(iv) Snapshots of total compressive force (in N) distribution (x- and y-axis labels represent distances normalized by larger sphere diameter) for different degrees of randomness at time t = 1.7 ms. (b) Range of values of the mass ratio m_s/m_b for the chosen value of stiffness ratio k_{sb}/k_{bb} (Eq. 3.4) for $\varepsilon = 0.9$ and $E_s/E_b = 1$. The dashed curves show the approximate transition boundary between the regimes, while the square marker shows the average properties.

Figures 3.2(a)(i)–(iv) also demonstrate that the shape of the wavefront remains approximately the same for all the cases. The shape invariability can be explained with the aid of the wave propagation map produced by Awasthi *et al.* [51] and shown in Fig. 3.2(b). The map illustrates the two key regimes of wave propagation - "directional" and "solitary wave" regimes - in 2D square packed systems for different mass and stiffness ratios denoted by m_s/m_b and k_{sb}/k_{bb}, respectively. The stiffness ratio is a function of Young's moduli ratio (E_s/E_b) given by

$$\frac{k_{sb}}{k_{bb}} = \frac{2E_s/E_b}{1 + E_s/E_b}\sqrt{\sqrt{2}(\sqrt{2} - 1)} \approx 0.765 \tag{3.4}$$

for the case analyzed in the present study. The dashed curves on the map correspond to the theoretically predicted approximate transition between the two wave propagation regimes. On the map, the entire range of m_s/m_b is depicted with a mean mass ratio of 0.071 for $E_s/E_b = 1$ ($k_{sb}/k_{bb} \approx 0.765$) and $\varepsilon = 0.9$. Thus the map shows that most of the data lie in the solitary wave regime and thus the wavefront shape remains approximately the same (square wavefront according to the map in Ref. [51]). Furthermore, by noting the similarity between cases $\varepsilon = 0.6$ [Fig. 3.2(a)(iii)] and $\varepsilon = 0.8$ [Fig. 3.2(a)(iv)], we observe that there appears to be a critical degree of randomness beyond which the response of the system does not change anymore. This critical randomness level, also noted in [44] and Chapter (2), is discussed further in later sections.

3.2.2 Force amplitude decay

Prior studies [43] have shown that the amplitude of the leading pulse decays with propagation distance in random 1D elastic chains. Furthermore, the decay in the peak force with distance transitions from an exponential to power law and the transition gets closer to the point of impact as ε increases (see Chapter (2)).

Figure 3.3 shows the peak force distribution of the larger spheres averaged over ±45° and multiple realizations. The peak forces (F_m) are depicted for ε ranging from 0 to 0.9, and are normalized by the peak force on the fifth larger sphere (i. e., after a transient response in the initial few spheres) in the nonrandom system (denoted by F_{05}). As shown in the figure, there is a decay in peak force in the nonrandom system ($\varepsilon = 0$) due to the effect of dimensionality. In the presence of randomness in densities, the force amplitude of the transmitted wave decreases further with increase in ε as more reflections occur due to density mismatch. Figure 3.3 also suggests the existence of a value of ε beyond which the transmitted force amplitude becomes independent of ε. This independence was also reported and characterized in 1D random chains (see Ref. [44] and Chapter (2)) where the value of ε is referred to as critical randomness (or disorder). As observed in Fig. 3.3, the critical randomness is around 0.6, which is approximately equal to that in 1D random chains with randomness in mass (Chapter (2)). This leads us to conclude that the critical randomness is independent of the configuration of the system, but rather depends only on the source of randomness (Chapter (2)).

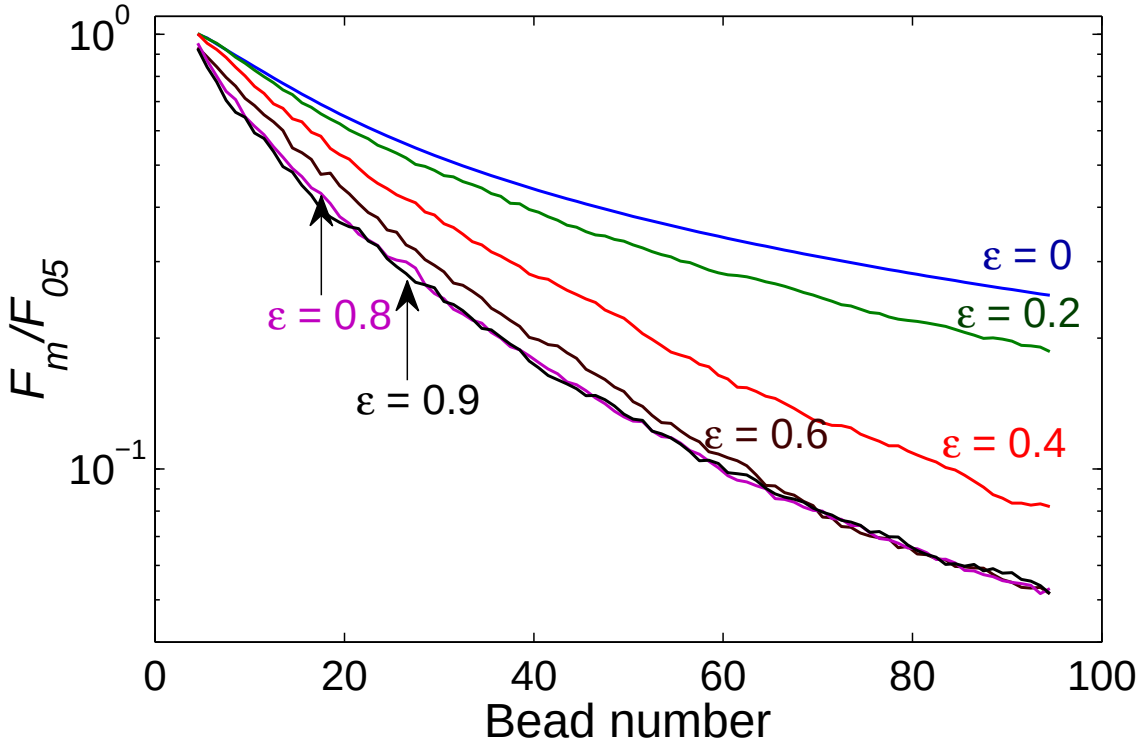

Figure 3.3: Spatial distribution of peak compressive force (F_m) on larger spheres averaged over the diagonals (±45°) for different degrees of randomness normalized by peak force of the fifth larger sphere for $\varepsilon = 0$, denoted as F_{05}. Decay in the nonrandom system ($\varepsilon = 0$) is due to the 2D nature of the wave propagation event.

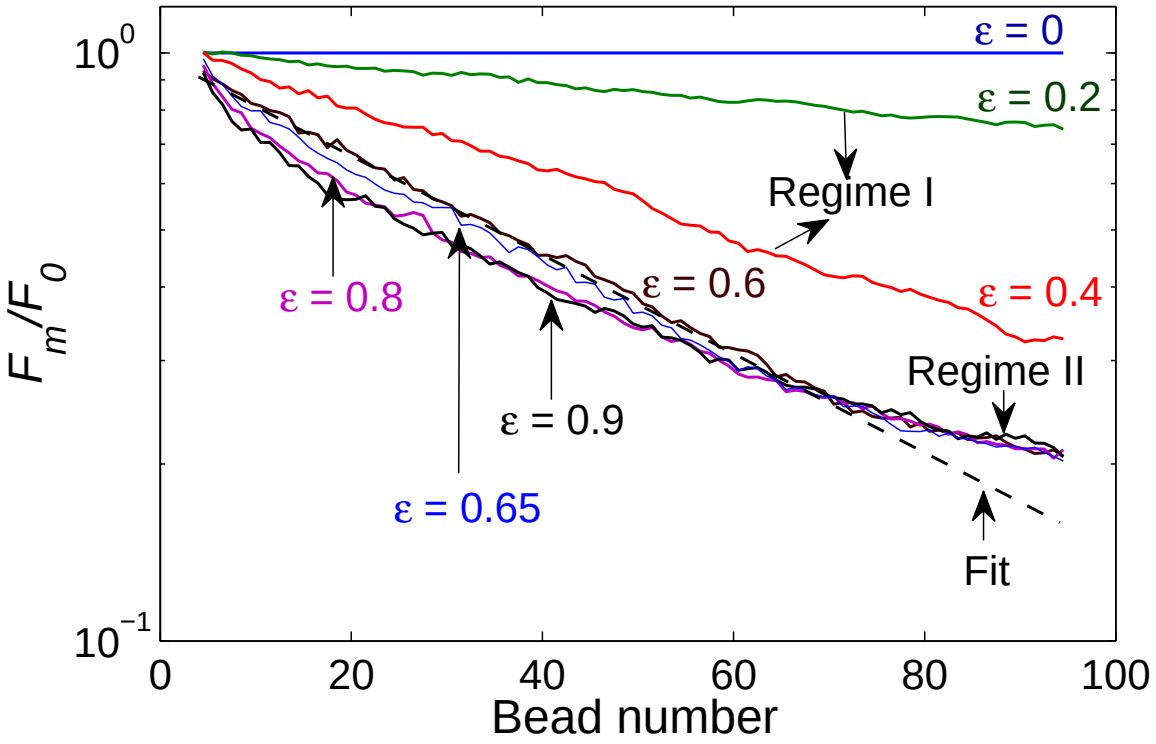

Figure 3.4: Peak force (F_m) distribution on larger spheres averaged over the diagonals (±45°) for various ε normalized by peak force distribution of $\varepsilon = 0$ (F_0). The two decay regimes, exponential (regime I) and power law (regime II), are now apparent.

As indicated in Fig. 3.3, the decay for $\varepsilon = 0.6$ overlaps with the decay of $\varepsilon = 0.8$ and $\varepsilon = 0.9$ after a certain distance (approximately around sphere number 70), suggesting a transition into the second regime of decay. Noting that the force amplitude decay shown in Fig. 3.3 (as indicated by the decay of $\varepsilon = 0$) includes the contribution of decay due to dimensionality, we normalize in Fig. 3.4 the peak force distribution (F_m) of larger spheres along ±45° for different ε by that of $\varepsilon = 0$, denoted by F_0.The error bars associated with the various curves shown in Fig. 3.4 are very small. For example, the average standard error for $\varepsilon = 0.65$ is about 1.7% of the mean value. Two regimes of decay are then clearly observed in the 2D random systems, exponential and a power law, similar to 1D random chains (Chapter (2)). The transition is made more clear by fitting an exponential curve for $\varepsilon = 0.6$ (dashed

line in Fig. 3.4) and extending it beyond the observed transition. The existence of regimes similar to 1D case also strengthens the assumption of decoupling the effect of dimensionality and randomness.

Observing that the 'dimensional decay' of the peak compressive force for $\varepsilon = 0$ is captured effectively by a power law, and separating the responses of dimensionality and randomness, the spatial dependence (on the distance z along the diagonal) of the peak force can be written as

$$\begin{aligned} F_m(z) &= D_m(z)R_m(z) \\ D_m(z) &= F_D z^{-\gamma_0} \\ R_m(z) &= \begin{cases} F_{R_1} e^{-\alpha_F(\varepsilon)z} & \text{regime I} \\ F_{R_2} z^{-\beta_F} & \text{regime II.} \end{cases} \end{aligned} \tag{3.5}$$

In Eqs. 3.5, $D_m(z)$ and $R_m(z)$ refer to the components of force amplitude due to dimensionality and randomness, respectively. F_D, F_{R_1} and F_{R_2} are parameters that depend only on material and geometric properties of the spheres, while γ_0 (≈ 0.5), α_F and β_F indicate decay coefficients due to dimensionality, exponential decay (regime I) and power-law decay (regime II), respectively. As apparent from Fig. 3.4 and also noted in 1D random chains, α_F is a function of ε while β_F is a constant. Characterization of decay in force amplitude for smaller spheres is similar to Eqs. 3.5, and is not discussed here.

Insight on the transition from the exponential decay to power-law regime in Figs. 3.3 and 3.4 can be obtained by monitoring snapshots of the forces acting on the spheres along 45°. Figure 3.5(a) shows snapshots for the nonrandom system ($\varepsilon = 0$) at $\tau = 355$, $\tau = 532$, $\tau = 710$ and $\tau = 887$, where τ is the nondimensional time defined as $\tau = (k_{bb}\sqrt{R_b}/m_{0b})^{1/2}t$. Here, a gradual decay in the force amplitude of the leading pulse is observed, which was described by a power law in the previous section. We also note the backscattering in the tail due to impedance mismatch between larger

and smaller spheres. There is also appearance of a small region of almost zero force between the head of the backscatter and the leading pulse. The "gap", referred to as the *silent region*, was also noted in 1D random chains (see Chapter (2)). The silent region is formed owing to a higher speed of the leading pulse associated with the aforementioned nonlinear relation between the wave speed V_s and the force amplitude F_m, $V_s \propto F_m^{1/6}$. As the amplitude of the leading pulse reduces further, the silent region is expected to reduce in length, and ultimately disappear.

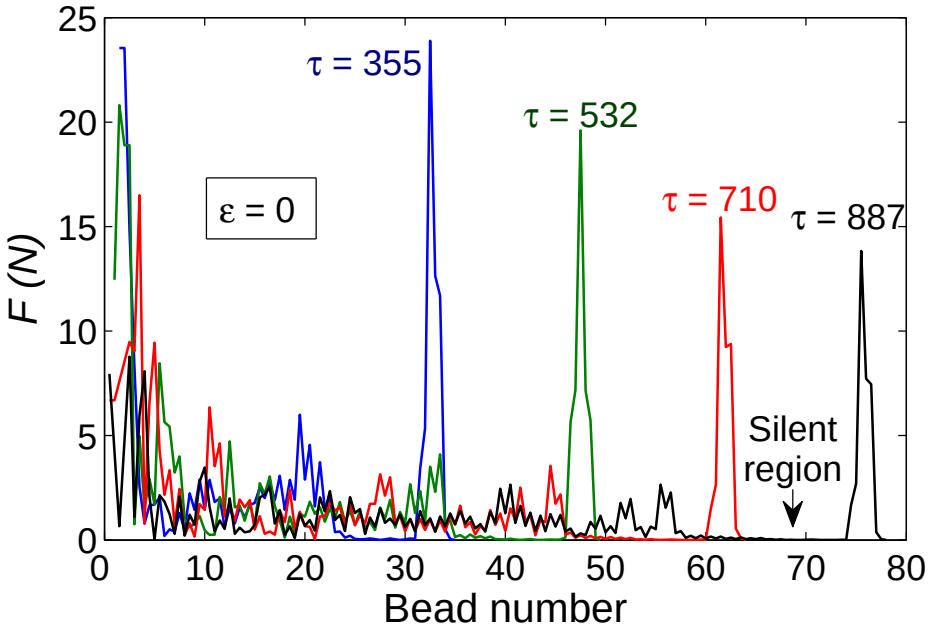

(a)

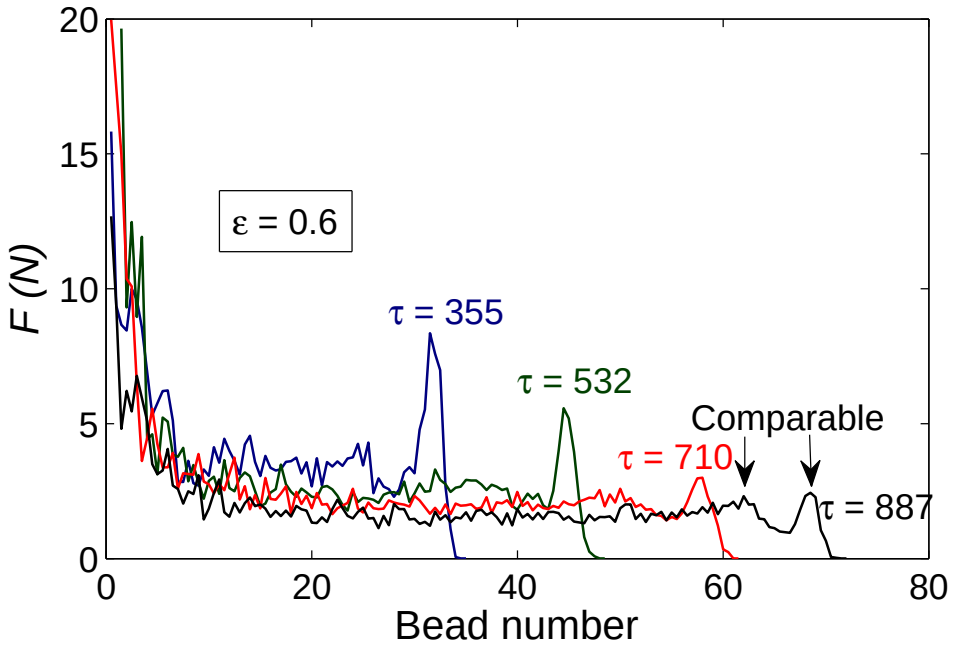

(b)

Figure 3.5: Total compressive force distribution for different instants of time [$\tau = (k_{bb}\sqrt{R_b}/m_{0b})^{1/2}t$] for larger spheres (averaged over ±45°) showing the progressive decay of the contact force for $\varepsilon = 0$ (a) and $\varepsilon = 0.6$ (b). Snapshot for $\tau = 887$ shows the instant when the force amplitude of the leading pulse becomes comparable to that of the backscatter. The location of the wavefront at that instant is also found to be equal to the distance at which transition from regime I to regime II occurs.

Figure 3.5(b) presents snapshots at the same time instants as in Fig. 3.5(a) for $\varepsilon = 0.6$. An enhanced decay of the leading pulse amplitude is observed in the presence of randomness in densities. As the leading pulse attenuates, there is an instant at which the amplitude of the leading pulse becomes equal to that of the backscatter. The instant ($\tau = 887$) is marked with the label "comparable" in Fig. 3.5(b). The corresponding sphere number exactly corresponds to the distance at which transition from exponential to power-law occurs. This proposition can be verified from Fig. 3.4 where the transition for $\varepsilon = 0.6$ occurs at about sphere number 70, which is equal to the transition sphere number shown in Fig. 3.5(b). Also, the backscatter behind the leading pulse becomes approximately constant in amplitude as the wave propagates. This result is different from 1D random chains described in Chapter (2), where the state of high delocalization is only achieved after much longer time (chain length > 1000 spheres).

3.2.3 Spatial distribution of peak compressive force

In this section, maps of peak compressive forces are generated in a quadrant to quantify the angular dependence of the spatial decay alluded to in the previous section. Starting with a structured initial grid of 100 by 100 points defined at the coordinates of the larger spheres, the peak forces are linearly interpolated to obtain values over the entire quadrant. The results are illustrated in Fig. 3.6 for degrees of randomness ε ranging from 0 to 0.8 with x- and y-axes showing the larger sphere numbers. As shown in Fig. 3.6(a), the contours for $\varepsilon = 0$ are initially concave (sharper corners), and then gradually become straight. The first few particles along 45° experience a rapid decay in peak force, after which the rate of decay is smaller (Fig. 3.3), thus leading to the transformation in the contour shape. With increase in degree of randomness, however, the contours become straight at smaller distances

from the point of impact because the decay is enhanced in all directions. Also, the contours transition from straight to approximately circular shape at larger distances, as visible for $\varepsilon = 0.4$ and $\varepsilon = 0.8$, suggesting an increasingly isotropic nature of the peak force distribution, as further analyzed in Fig. 3.7.

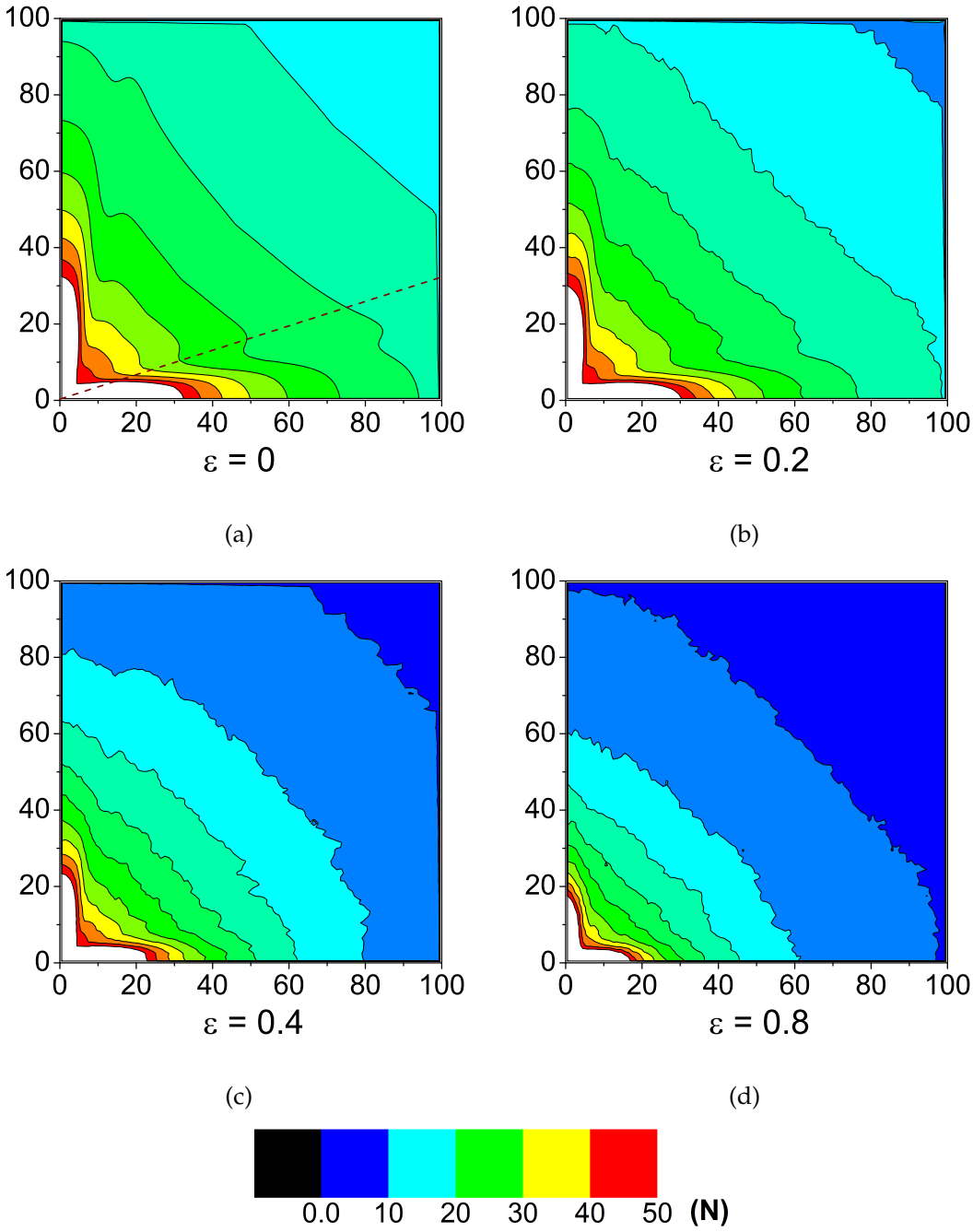

Figure 3.6: Spatial distribution of total compressive force on larger spheres in the first quadrant (x- and y-axis labels are larger sphere numbers) for different degrees of randomness, ε, ranging from 0 to 0.8. The results, averaged over sixty realizations, show a transition from concave to straight to convex contour shape as ε and the distance from the point of impact increase. The white zone depicts forces higher than 50 N near the initial impact area.

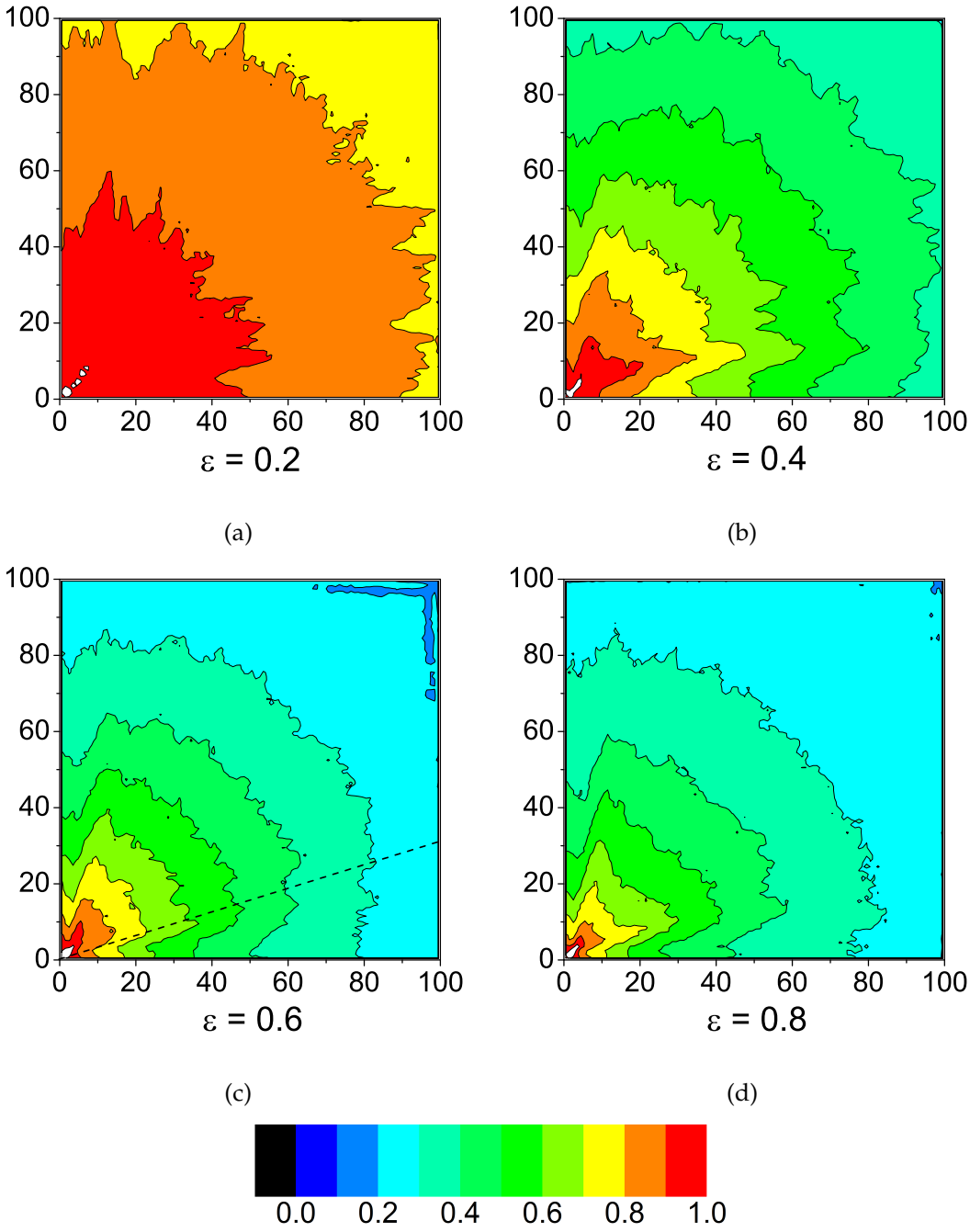

Figure 3.7: Spatial distribution (x- and y-axis labels are sphere numbers) of peak compressive force acting on the larger spheres for different degrees of randomness normalized by the force distribution of the nonrandom system.

Focusing on the effect of randomness in densities, Fig. 3.7 shows the spatial distribution of peak compressive forces for various degrees of randomness normalized

by those of the nonrandom system as done previously in Fig. 3.4. As apparent there, the peak force attenuates more in the 0° and 90° directions, as noted by the steepening of the contours in these directions. The enhanced attenuation also confirms the earlier observation in Fig. 3.6 where the contours changed from concave to straight shape. For smaller distances from the point of impact, as apparent in Fig. 3.7, the decay is anisotropic while the contours become circular at larger distances for all the degrees of randomness, indicating the attenuation due to randomness to be isotropic in this regime.

The anisotropic nature of the decay is further quantified in Fig. 3.8, which shows the peak force distribution for various angles in the first quadrant for $\varepsilon = 0.6$. As observed there, the peak forces at smaller distances from the point of impact are higher for angles close to 0°, as was noted in Fig. 3.6. At larger distances, the curves for all the angles merge, indicating that contours of peak force are approximately circular leading to the aforementioned isotropic decay.

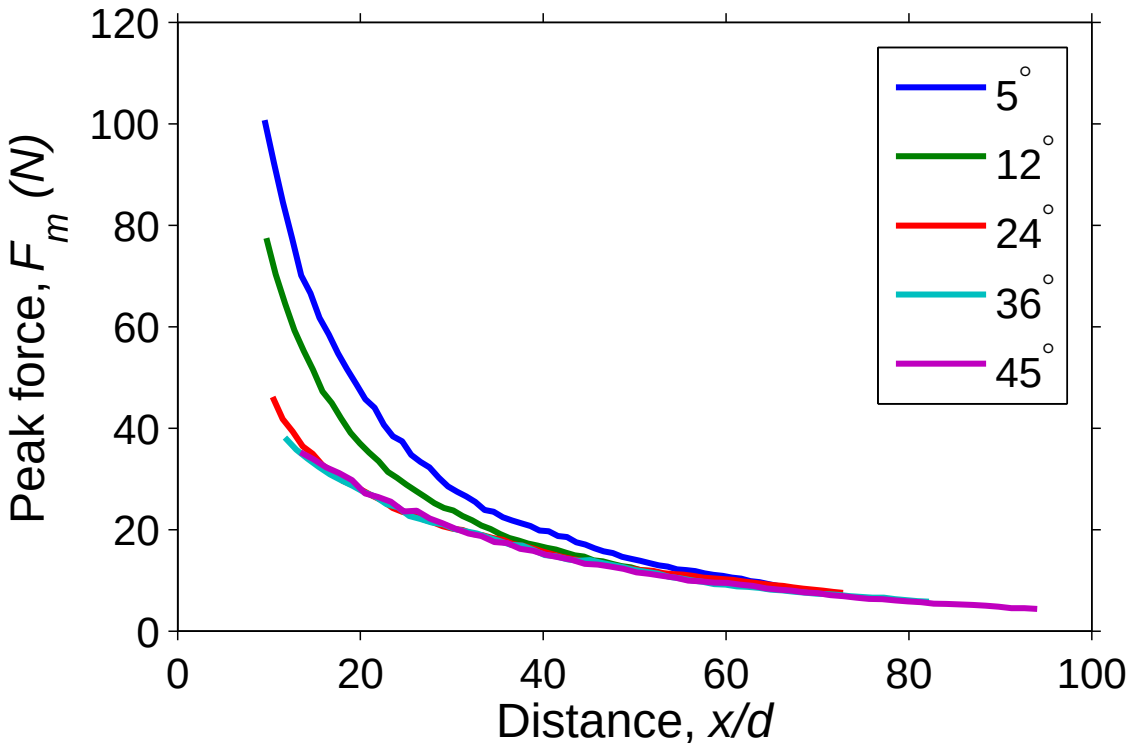

Figure 3.8: Variation of peak force with distance for $\varepsilon = 0.6$ along different directions. The peak forces are essentially the same along all directions at larger distances from the point of impact, indicating that the decay becomes increasingly isotropic.

Using the contour maps shown in Figs. 3.6 and 3.7, the decay coefficient α_F can be extracted for different degrees of randomness and various angles θ ranging from 0° to 90° in intervals of 1°. For each θ, the peak force values are first interpolated based on the initially generated peak force values on the 100 by 100 grid. Then the decay coefficients are extracted by fitting an exponential curve to the peak force data from a distance from the point of impact equal to about sum of five larger and smaller bead diameters up to the transition to regime II. Figure 3.9 shows the dependence of the decay coefficient α_F on angle θ for $\varepsilon = 0.2$, 0.4 and 0.6. As expected, the curves are symmetric about 45°, except for small deviations due to the finite number of realizations. The results demonstrate mainly three different regions, viz., an initial region of high decay, minimum decay and approximately

constant decay. The region of high attenuation for small angles corresponds to steeper contours at the corners in Fig. 3.7. Then the decay decreases to a minimum which occurs in the range $15 - 20^\circ$ for all ε, which can be explained by referring to the kinks associated with the presence of intersecting wavefronts in the nonrandom case [51] and denoted by dashed lines in Figs. 3.6(a) and 3.7(c). The decay coefficient later increases to reach a constant value, as the contours are approximately circular in this regime where peak force decay of 24°, 36° and 45° overlapped (Fig. 3.8). This decay depends on the underlying granular structure but the anisotropy of decay will be qualitatively maintained even if the direction of impact is other than 45°. These results identify potential ways to optimize granular systems for objective functions such as minimizing the rate of decay or inducing an isotropic force decay. In the absence of intruders, however, the impact event would generate waves that propagate along 0° and 90° directions [51]. In that case, since wave propagation is basically 1D, the force decay is expected to be substantially slower than in the system with intruders.

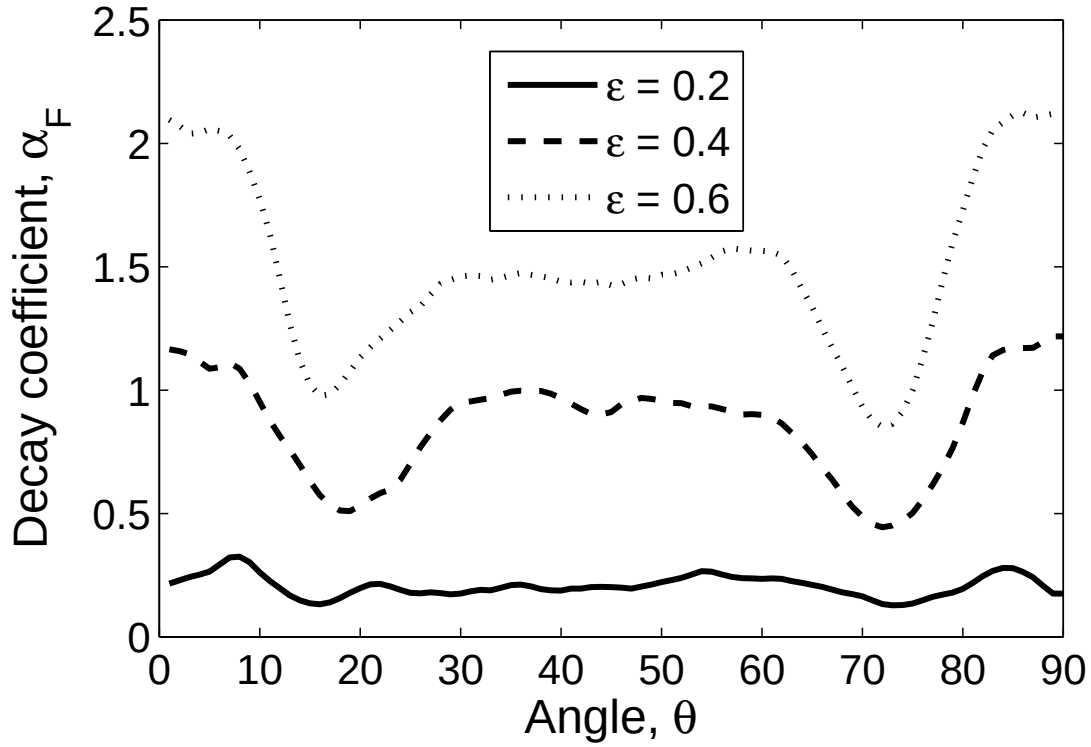

Figure 3.9: Decay coefficient α_F in the exponential regime as a function of angle θ for different degrees of randomness.

3.2.4 Evolution of ensemble kinetic energy

We now turn our attention to the evolution of ensemble kinetic energy, defined as the sum of kinetic energies of all the spheres in the system, for various degrees of randomness. The ensemble kinetic energy gives a measure of the particle vibrations, while the compressive forces are accounted for by the ensemble potential energy evaluated by summing the potential energy of each interaction. Since the energy of the system is conserved, this analysis provides insight on the exchange of energy between potential and kinetic energies as the wave propagates through the different regimes discussed earlier. The relevant data is compared with the virial theorem discussed in Chapter (2), which relates the time-averaged kinetic energy to the time-averaged potential energy for a system of particles interacting via potentials such

as the Hertzian potential used in the present study.

Figure 3.10 describes the evolution of ensemble kinetic energy (KE), normalized by the initial impact energy, with ε ranging from 0 to 0.8. For periodic and/or spatially bound conservative systems [62, 63], the virial theorem predicts the time-averaged kinetic energy for particles interacting via the Hertzian potential to be 0.555. For solitary wave propagation in 1D homogeneous nonrandom elastic chains, that quantity was found to be very close to 0.555, since the wave is confined to about five particle diameters and travels without decay or dissipation [5]. In the present 2D case, however, the mean value of ensemble kinetic energy for $\varepsilon = 0$ is found to be 0.571 in the simulations. This deviation from the virial theorem prediction is due to the absence of spatial boundedness, as the pulse is no longer confined to small number of particles due to dimensionality and backscattering (see Fig. 3.2(a)(i)).

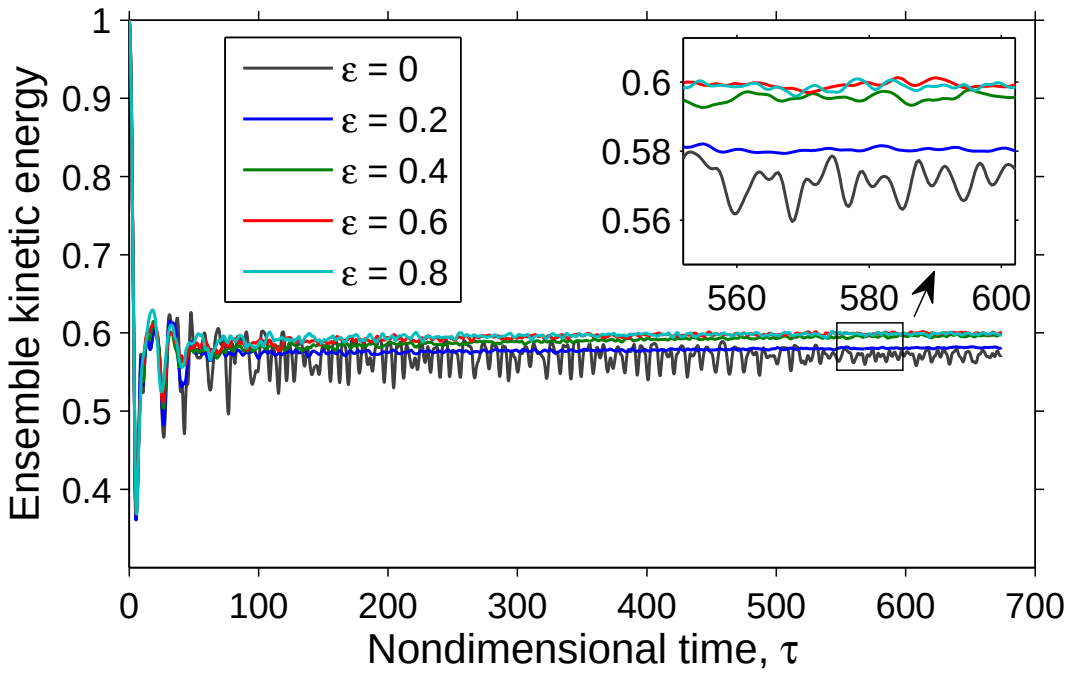

Figure 3.10: Evolution of ensemble kinetic energy normalized by the initial impact energy for different degrees of randomness. The ensemble KE increases with increase in randomness. The inset shows a portion of the curves, enlarged for clarity, showing the overlap between $\varepsilon = 0.6$ and $\varepsilon = 0.8$.

With increase in ε, an increase in ensemble KE is observed due to higher impedance mismatch at contacts. The increase in ensemble KE obtained here is not as pronounced as in 1D random chains described in Chapter (2) mainly because of the boundary conditions. In the 1D study, the initial impact sphere was not fixed and thus the reflected waves caused the first few spheres to freely move *away* from the system, leading to enhanced increase in ensemble KE. In the present 2D case, the impact is provided at the center of the system, and thus the initial spheres are confined to vibrate with small amplitudes essentially forcing them to stay *within* the system. Mean values for different ε are provided in Table 3.1, showing the increase in ensemble KE with randomness. The role of critical randomness is also apparent from the table, where we note the values for $\varepsilon = 0.6$ and $\varepsilon = 0.8$ are approximately the same.

Table 3.1: Computed mean values of ensemble KE normalized by the impact energy for various degrees of randomness.

Degree of randomness (ε)	Mean ensemble KE
0	0.571
0.2	0.578
0.4	0.588
0.6	0.594
0.8	0.595

3.3 Conclusions

The effect of randomness in densities on nonlinear wave propagation in 2D granular systems composed of closely packed spherical particles was investigated numerically. The two main features of wave propagation in such systems - effect of dimensionality and randomness - were characterized for different levels of randomness. Force amplitude decay due to dimensionality closely followed a power law, and a separation of variables was employed to extract the force transmission response

due to randomness alone. The resulting variation showed two regimes of decay, exponential and power law, similar to observations made in 1D random chains. The transition from exponential to power-law regime occurred when the amplitude of the leading pulse was equal to that of the backscatter, also consistent with 1D results. Contours of peak forces on the larger spheres were obtained by linear interpolation and contour shapes were characterized for different distances from impact and degrees of randomness, showing an increasingly isotropic nature of force decay. Decay in the exponential regime of propagation was quantified by extracting decay coefficients for various angles, showing regions of minimum or constant decay rate. Evolution of ensemble kinetic energy was found to be consistent with 1D random chain, with a progressive increase in kinetic energy.

Chapter 4

Plane wave propagation in monodisperse granular media

In the previous chapters, we studied the effect of randomness on wave propagation in 1D and 2D granular media. We essentially demonstrated how randomness can be taken advantage of in applications where energy decay is the key objective. Randomness was found to enhance the decay due to dimensionality in 2D granular media. In this chapter, we focus on another practical aspect in applications which is the loading area. If ordered or disordered granular media were to be deployed in practical applications, the loading area would likely be spread over a large number of spheres since the typical diameter of a sphere is of the order of a few millimeters. The present study complements the work done in previous years on the effect of point impact on granular layers with spheres arranged in hexagonal packing or square packing with intruders (see [49, 50, 51, 55]). The focus of our study is on the other 'extreme' loading condition, i.e., uniform planar impact on 2D and 3D periodic granular media. Qualitatively, randomness is expected to play a similar role as in the case of point impact and therefore the current study excludes randomness to specifically address the effect of planar impact.

One of the objectives is to establish an equivalence between a uniformly loaded 2D or 3D granular layer and a 1D chain. Some of the advantages of such a simplification include a drastic reduction in computational cost when simulating large systems, and a theoretical prediction of the force transmission response of higher-dimensional structures based on 1D numerical or theoretical results. Another key objective of the present study is to investigate the mixed compression/shear dynamic

response of granular media. In the first part of the study, analytical solutions are derived for various periodic granular structures such as 2D/3D hexagonal packing and 3D face-centered cubic packing under uniform perpendicular loading. Owing to the symmetry and periodic conditions of the domain, the motion of the spheres is in the direction of impact and the response is thus compared to that of 1D granular chains. The nonlinear dependence between the wavefront speed and its force amplitude for 2D and 3D systems are related to that of 1D chains and are found to be in very good agreement with the simulations. The analytical predictions are also applicable to dimer systems made up alternating layers of spheres of different radius or Young's modulus.

Finally, numerical studies are performed on force transmission response of 2D hexagonal packing under uniform angular impact. The shearing component in the impact loading leads to the motion of the spheres in the horizontal direction, but the shearing effect decays very quickly after just a few layers. The amplitude of the horizontal component of velocity of the spheres is found to decay exponentially in the initial layers and further decay in a series of linear regimes with different decay rates. After the complete decay of shearing effect, the wavefront propagates in a way similar to that of the perpendicular impact case. A semi-analytical study based on two layers in contact is adopted to predict the gradual transformation of direction of propagation of spheres from the impact angle to the perpendicular case.

The present chapter is divided into a number of sections as follows. In Sec. 4.1, the equations of motion for a granular system and the simulation procedure are described. Section 4.2 discusses the normal impact case for 2D and 3D granular media and provides analytical derivation and verification (Secs. 4.2.1 and 4.2.2) for the equivalent 1D chains. Section 4.3 describes the angular impact case. The numerical observations are discussed in Sec. 4.3.1, while Sec. 4.3.2 reports analytical predictions for some of the key phenomena observed in the angular impact case

and a comparison with numerical results. The results of the above study has been published in *Granular Matter* ("Plane wave propagation in 2D and 3D monodisperse periodic granular media." *Granular Matter* 16.1 (2014): 141-150) and the remainder of this chapter follows in most part that publication.

4.1 Numerical setup

In this study, various 2D and 3D ordered granular packings made up of elastic monodisperse spherical particles are considered. Initial conditions in the form of velocity impulses transmit compressive pulse(s) in the domain. The equations of motion for sphere i and definitions for the relevant parameters are given in Sec. 3.1.

Figure 4.1 shows the four packings investigated in the present study: 2D hexagonal (Fig. 4.1(a)), 3D face-centered cubic (Fig. 4.1(b)), 3D hexagonal close packing (Fig. 4.1(c)) and 3D body-centered cubic packing (Fig. 4.1(d)). The spheres in the topmost layer are given an initial impact velocity of magnitude v_{p0} along direction θ as shown. In the following sections, the analysis is divided into two cases, viz., planar perpendicular (or normal) impact ($\theta = 90^\circ$) and angular impact (arbitrary θ). We model the systems using periodic boundary conditions in the direction(s) 'x' for 2D and 'x' and 'y' for 3D packings. The prominent direction of propagation of compressive pulses ('y' in 2D and 'z' in 3D) is modeled as a semi-infinite system, i.e., the transmission response is free from the influence of the boundary.

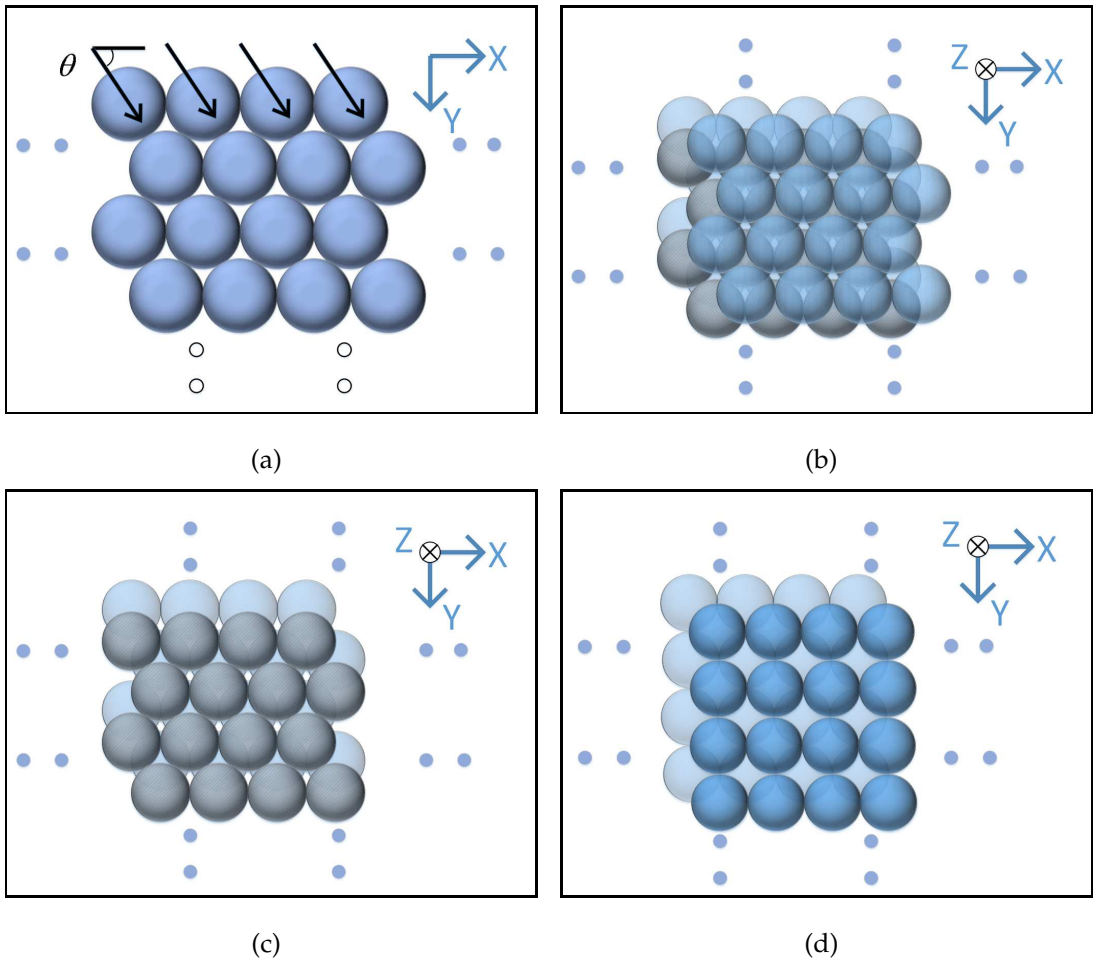

(a) (b)

(c) (d)

Figure 4.1: Different granular structures of spherical particles considered in the present study: (a) 2D Hexagonal packing where θ is the angle of impact, (b) face-centered cubic (FCC) packing, (c) hexagonal close packing (HCP) and (d) body-centered cubic (BCC) packing. Figures (b), (c) and (d) show top views (x-y plane) of the free surface of the semi-infinite granular structures. Filled circles indicate periodic directions, while open circles indicate semi-infinite directions.

All the numerical results are presented using nondimensional quantities, where displacement and distance are normalized by the radius of a sphere (R), while time (t) is normalized as

$$\tau = \frac{t}{\beta} = \left(\frac{K\sqrt{R}}{m}\right)^{1/2} t. \tag{4.1}$$

Dissipative effects such as friction, plasticity and viscous damping are neglected. The numerical simulations are performed using the molecular dynamics package

LAMMPS [61] by considering spheres as point masses connected by nonlinear springs. Time step is chosen as $\tau \approx 3.55 \times 10^{-3}$. The total energy and linear momentum are conserved with a relative error less than 10^{-7} and 10^{-12}, respectively.

4.2 Normal impact

Consider different granular packings under uniform planar impact as shown in Fig. 4.1, where θ is the angle of impact. In this section, normal impact ($\theta = 90°$) is considered, and the periodic conditions imply that y-displacements (z-displacements) are the only nonzero components in 2D (3D) packings since all the spheres in each layer have equal displacements. The foregoing discussion applies to 2D hexagonal packing but can be generalized to 3D.

4.2.1 Analytical study

In order to predict analytically the force propagation response due to normal impact, one needs to first derive the equations of motion of a sphere for any packing. The forces acting on a sphere are obtained using the Hertzian contact law, with the deformation at a contact defined as follows: Let $\delta_{i-1,i}$ be the relative displacement between two neighboring spheres (in layers $i-1$, i) located at (x_1, y_{0i-1}) and (x_2, y_{0i}), respectively. If the corresponding y-displacements for these two spheres are denoted by v_{i-1} and v_i, then

$$\begin{aligned}\delta_{i-1,i} = &\sqrt{(x_2 - x_1)^2 + (y_{0i} - y_{0i-1})^2} \\ &- \sqrt{(x_2 - x_1)^2 + (y_{0i} - y_{0i-1} + v_i - v_{i-1})^2} \\ = 2R &- \sqrt{4R^2 + 2(y_{0i} - y_{0i-1})(v_i - v_{i-1}) + (v_i - v_{i-1})^2}.\end{aligned} \tag{4.2}$$

By assuming that the displacements are much smaller than the radius (R), one gets

$$\begin{aligned}\delta_{i-1,i} &\approx 2R\left[1-\sqrt{1-\frac{(y_{0i}-y_{0i-1})}{2R^2}(v_{i-1}-v_i)}\right] \\ &\approx \frac{(y_{0i}-y_{0i-1})}{2R}(v_{i-1}-v_i).\end{aligned} \tag{4.3}$$

In Eq. (4.3), $(y_{0i} - y_{0i-1})$ corresponds to the distance between adjacent layers, and thus its value depends on the packing under consideration. For example, for 2D hexagonal packing, the value is $\sqrt{3}R$, and similar values can be found for other packings. The contact force magnitude F (valid for spheres under compression) is given by

$$F_{i-1,i} = K\delta_{i-1,i}^{3/2} = (4/3)E^*\sqrt{R^*}\delta_{i-1,i}^{3/2}, \tag{4.4}$$

where E^* and R^* were defined in Sec. 4.1. The equation of motion for a sphere of mass m can then be written by considering all the contact forces. For 2D hexagonal packing, Eq. (4.3) yields

$$\ddot{v}_i = \sqrt{3}\frac{K}{m}(\delta_{i-1,i}^{3/2} - \delta_{i,i+1}^{3/2}) \tag{4.5}$$

$$= \sqrt{3}\left(\frac{\sqrt{3}}{2}\right)^{3/2} A[(v_{i-1}-v_i)^{3/2} - (v_i - v_{i+1})^{3/2}], \tag{4.6}$$

with $A = 2E/(\pi\rho(1-\nu^2)(2R)^{5/2})$, where ρ is the density of the particles. Equation (4.6) is indeed very similar to the equation of motion for a sphere in a 1D homogeneous chain with the factor $f = \sqrt{3}(\sqrt{3}/2)^{3/2}$ in Eq. (4.6) replaced by unity [5]. The above 1D equivalence also holds if the adjacent layers have different Young's moduli or radii (assuming packing remains the same), in which case an appropriate value of E^* or R^* should be used in K.

To derive the constant factor in the nonlinear dependence between the wavefront speed and the force amplitude in the 2D hexagonal system, a scaling analysis is

employed. Nesterenko's continuum approximation to the 1D chain of spheres [5] provides the scaling relation between the strain (ξ), the wave speed (V) and the factor f. This continuum definition of wave speed, which arises from traveling wave assumption, is calculated in the discrete case by monitoring the time difference between peak forces or velocities at adjacent contacts. Since the strain in the system is equal to the particle velocity (v_p) divided by the wave speed, one gets the relations

$$\xi_{2D} = \frac{1}{f^2}\frac{V_{2D}^4}{V_{1D}^4}\xi_{1D} \Rightarrow v_{p2D} = \frac{1}{f^2}\frac{V_{2D}^5}{V_{1D}^5}v_{p1D}. \tag{4.7}$$

Finally, the force amplitude (F_m) and the strain amplitude (ξ_m) are related by

$$F_m = K\delta^{3/2} \approx K(2R)^{3/2}\xi_m^{3/2}, \tag{4.8}$$

where the deformed length is assumed to be approximately the strain times the diameter of a sphere. Using Eqs. (4.3), (4.7) and (4.8), one obtains

$$\frac{F_{m2D}}{F_{m1D}} = \left(\frac{\sqrt{3}}{2}\right)^{3/2}\frac{\xi_{m2D}^{3/2}}{\xi_{m1D}^{3/2}} = \left(\frac{\sqrt{3}}{2}\right)^{3/2}\frac{1}{f^3}\frac{V_{2D}^6}{V_{1D}^6}. \tag{4.9}$$

We now define the *wavefront speed* ($\overline{V}$) as the component of the wave speed (V) along the direction of propagation. For example, for the 2D hexagonal packing, $\overline{V} = Vsin(60°) = (\sqrt{3}/2)V$. Employing the nonlinear dependence between the wave speed and the force amplitude for 1D chains, $V = BF_m^{1/6}$ [22], where

$$B \approx \left(\frac{384}{125\pi^3}\right)^{1/6}\left(\frac{E}{R\rho^{3/2}(1-\nu^2)}\right)^{1/3}, \tag{4.10}$$

we get

$$\overline{V}_{2D} = \frac{3}{2\sqrt{2}}BF_{m2D}^{1/6}. \tag{4.11}$$

Similarly, force-wavefront speed relations for the 3D systems of the present study are

$$\overline{V}_{FCC} = \frac{2}{\sqrt{3}} B F_{mFCC}^{1/6} \quad \text{and} \quad \overline{V}_{BCC} = B F_{mBCC}^{1/6}. \tag{4.12}$$

We note that the response of the HCP system will be equal to that of the FCC packing due to periodic boundary conditions in the in-plane directions.

4.2.2 Verification

Figure 4.2 shows the dependence of the wavefront speed and the force amplitude for various granular configurations. Numerical results are compared with the analytical predictions from the previous section along with results for a 1D chain. The wavefront speed and force amplitude are normalized as

$$\widetilde{V} = \frac{\beta}{R}\overline{V} = \left(\frac{m}{KR^{5/2}}\right)^{1/2}\overline{V} \quad \text{and} \quad \widetilde{F}_m = \frac{F_m}{KR^{3/2}}, \tag{4.13}$$

respectively. As apparent there, the analytical predictions are in very good agreement with the simulations. As alluded to in Eq. (4.12), the wavefront speed for the 3D BCC packing is exactly equal to the corresponding 1D chain, thus is represented by the same analytical curve in Fig. 4.2.

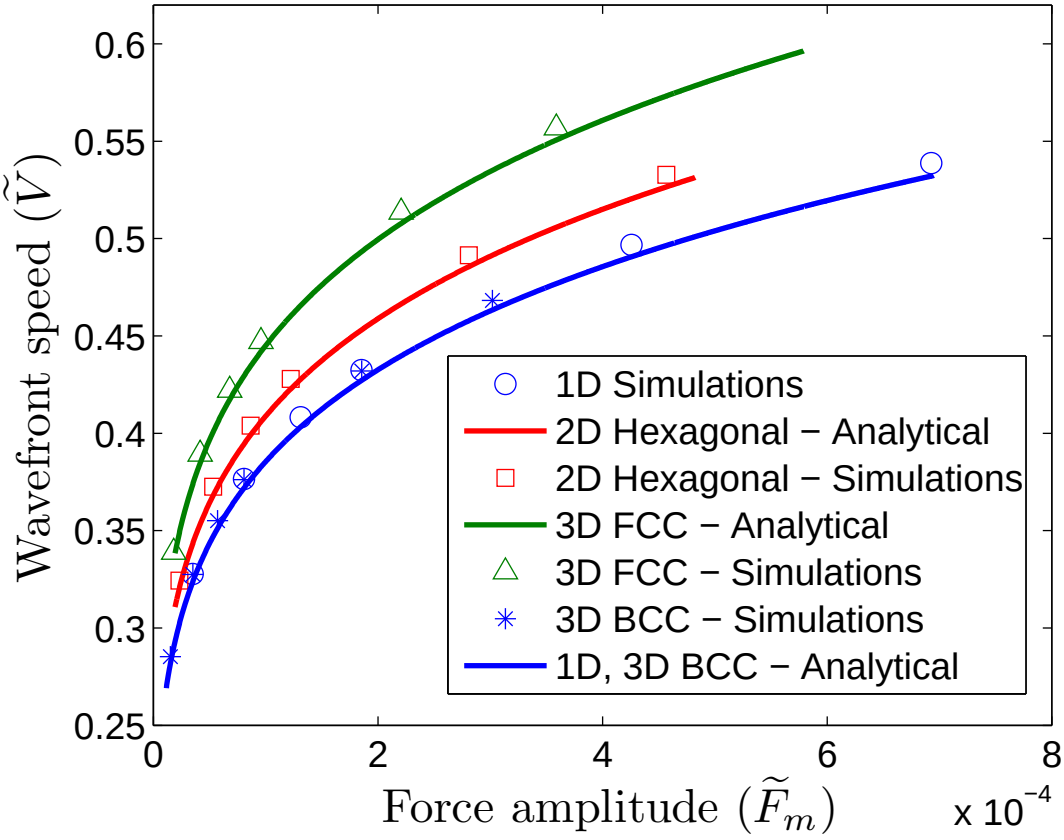

Figure 4.2: Normalized wavefront speed ($\widetilde{V}$) versus force amplitude ($\widetilde{F}_m$) for different granular systems. Solid curves correspond to the analytical relations Eq. (4.11) and (4.12) and symbols to numerical results. Note that a 3D BCC system and the 1D homogeneous chain show equivalent responses. $\widetilde{V}$ and $\widetilde{F}_m$ are defined in Eq. (4.13).

4.2.3 Normalization

The aforementioned equations of motion and scaling relations point to two parameters governing the constant factor entering the wave speed-force amplitude relations (Eqs. (4.11)-(4.12)). One is given by the number of contacts n_c between a sphere and an adjacent layer, and the other is the height h equal to the distance between adjacent layers. The scaling relations discussed in the previous section yield

$$\frac{\widetilde{V}}{n_c^{1/2}\tilde{h}^2} = \frac{\beta K^{1/6}}{R^{3/4}} B \widetilde{F}_m^{1/6}, \tag{4.14}$$

where B is given by Eq. (4.10) and $\tilde{h} = h/(2R)$. For 2D hexagonal packing, $n_c = 2$ and $\tilde{h} = \sqrt{3}/2$, and thus one recovers the wavefront speed relation in Eq. (4.11). Figure 4.3 demonstrates the normalized wavefront speed $(\widetilde{V}/(n_c^{1/2}\tilde{h}^2))$ as a function of its force amplitude $(\widetilde{F}_m)$ where all the curves previously separated in Fig. 4.2 collapse onto one curve, verifying the normalization described by Eq. (4.14).

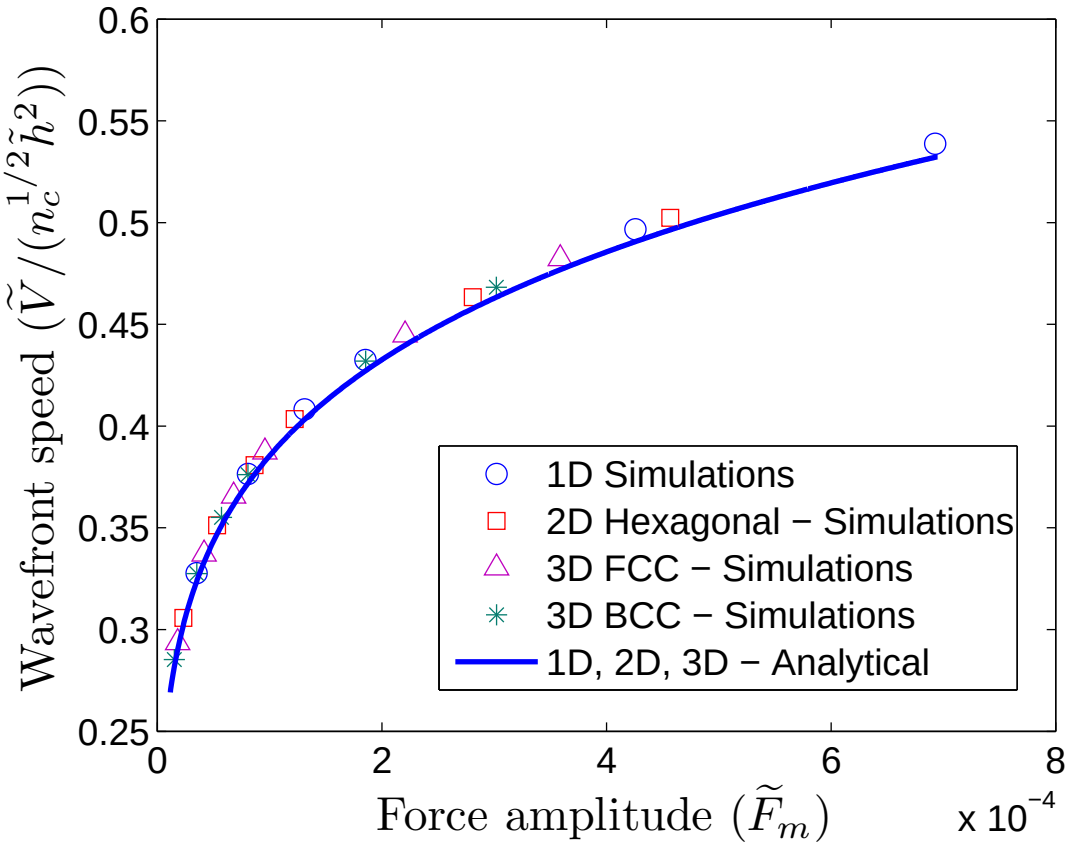

Figure 4.3: Normalized wavefront speed $(\widetilde{V}/(n_c^{1/2}\tilde{h}^2))$ as a function of force amplitude $(\widetilde{F}_m)$ given by the scaling relation in Eq. (4.14). All the curves in Fig. 4.2 collapse to the normalized curve.

4.3 Angular impact: 2D hexagonal packing

In this section, we discuss the force transmission response of a 2D hexagonal packing under angular impact, i.e., $0° \leq \theta < 90°$ (Fig. 4.1(a)). The key difference between the

angular impact and the normal impact is the presence of the shearing component in the former, with $\theta = 0^\circ$ corresponding to pure shear. Consequently, the spheres are expected to have also a motion in the horizontal ('x') direction.

4.3.1 Numerical observations

Consider a 2D hexagonal packing with impact angle $\theta = 60^\circ$. Figure 4.4 illustrates the history of the contact forces between neighboring layers as the disturbance propagates in the system. The contact forces labeled I and II correspond to the two distinct contacts taking place between any two layers as shown in the inset of Fig. 4.4. As expected, the force of contact I is initially lower than that of contact II as illustrated by the curves labeled 'layers 1-2'. However, the contact I force increases with depth while the contact II force decreases. As apparent in Fig. 4.4, the forces at contacts I and II become identical after a certain depth. The mechanism for the transformation of contact forces is explained as follows. For any θ, the presence of the contact forces between layers '1' and '2' induce layer '2' to start its motion along some $\theta \geq 60^\circ$ since the line joining the centers is along $\theta = 60^\circ$. Consequently, each successive layer starts its motion along an angle greater than the previous layer, gradually changing the direction of motion from the impact angle θ to 90° after a certain depth, where the forces at the two contacts become equal. The scenario is then similar to that of the normal impact case.

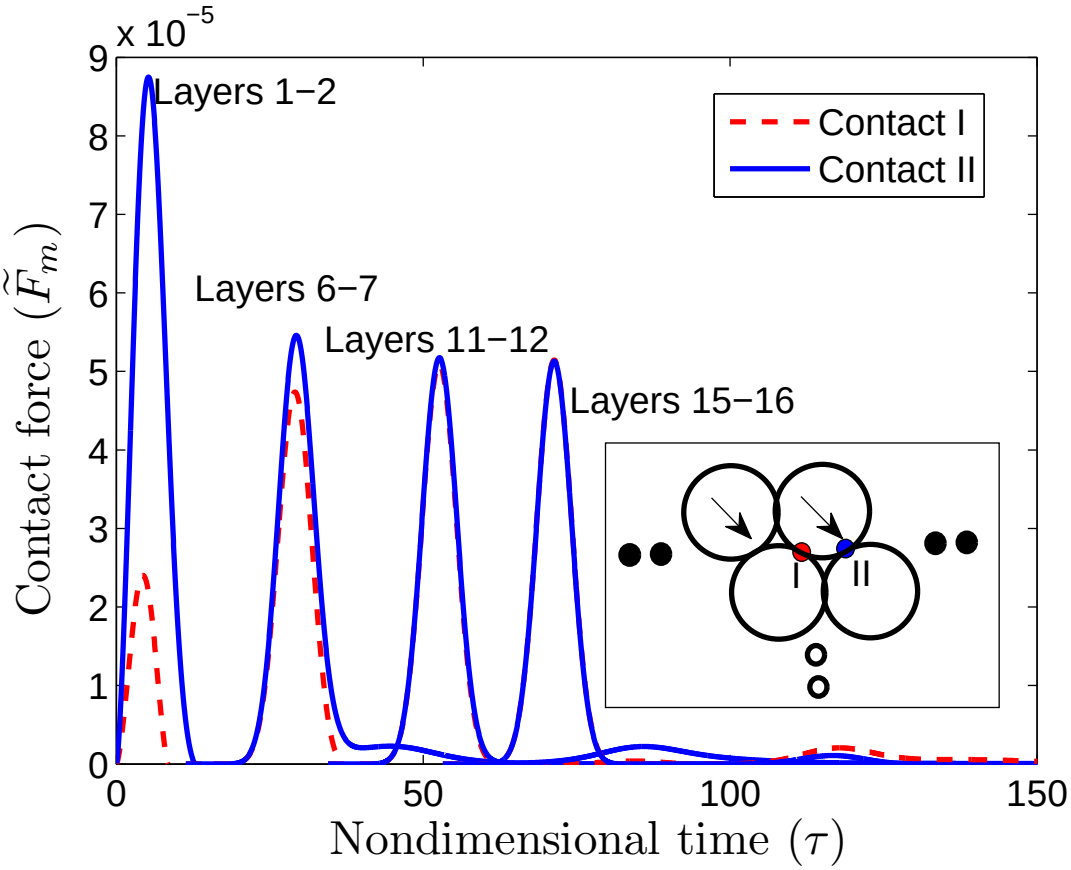

Figure 4.4: Force history of the two contacts I and II, illustrated by the dotted and solid curves, respectively, at different depths for the angular impact with $\theta = 60°$. Label 'layers $i - j$' refers to the two contact forces between layers i and j.

Figure 4.5 shows the variation of the history of the x-component of the particle velocity v_{px} for $\theta = 60°$ as a function of depth, normalized to show layer numbers. The particle velocity is nondimensionalized by the same factor as in the wavefront speed (Eq. (4.13)). Referring to the labels in Fig. 4.5, layer '2' is the layer below the impacting layer. As observed in Fig. 4.5, particle velocity v_{px} decreases with increase in depth. The decay of particle velocity follows from the mechanism described earlier where the system reaches a state similar to the normal impact case after a certain depth, resulting in only the vertical component of particle velocity. Figure 4.5 also shows that the spheres in the initial layers are in free flight after some time, which occurs due to oblique collisions between the layers. As expected,

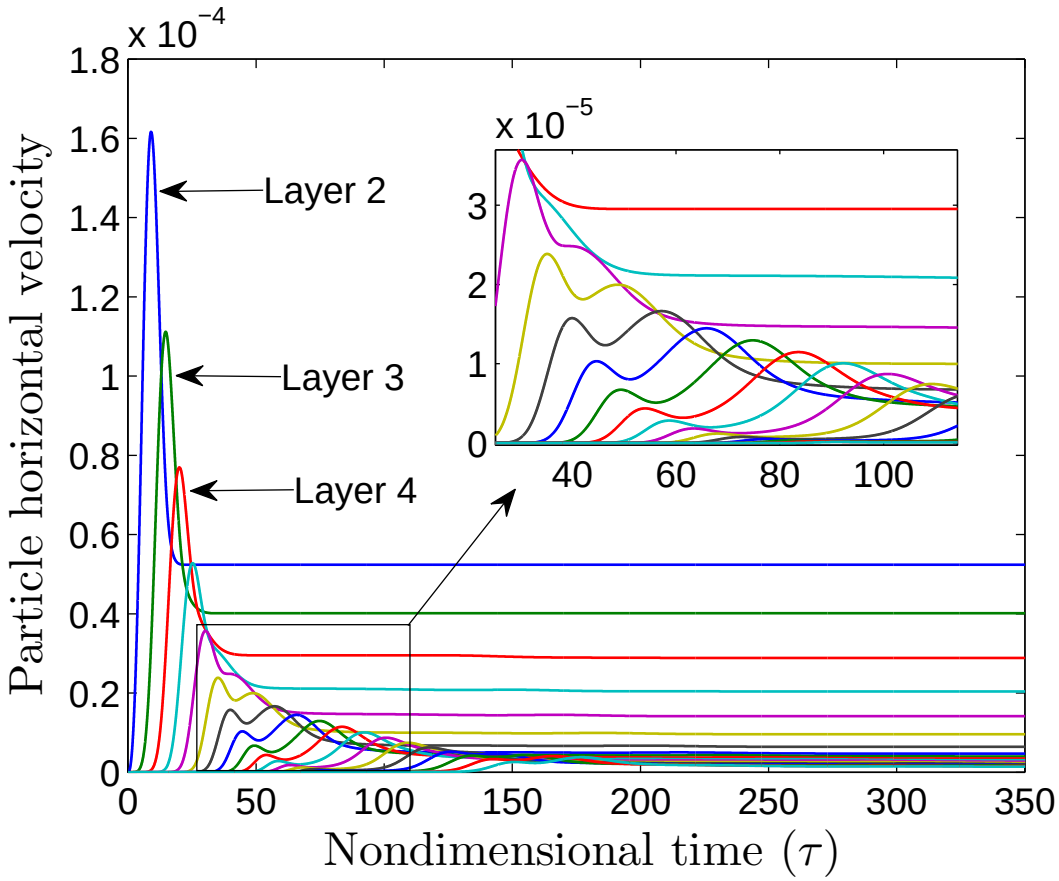

Figure 4.5: History of the x-component of particle velocity as a function of depth (layers) for $\theta = 60°$ showing a rapid decay in amplitude and the appearance of secondary peaks.

the horizontal component of the free-flight velocity ceases to exist after a certain depth. Furthermore, there is formation of secondary waves after few layers, the consequence of which will be discussed shortly.

Figure 4.6 shows the variation of the peak amplitude of v_{px} as a function of depth, extracted from Fig. 4.5. As apparent in Fig. 4.6, there are several regimes of decay in peak amplitude, as indicated by the labels 'R_1' to 'R_4'. The solid vertical lines mark the transition between different regimes. A simple curve fit demonstrates that the regime 'R_1' is very well described by an exponential decay while the regimes 'R_2' to 'R_4' are described by a linear decay. As seen in Fig. 4.5, secondary waves decay slower than the primary waves leading to higher amplitude of the former

after a certain depth. Similar secondary waves lead to the formation of other linear regimes. Although it appears that the transition has to be function of the primary wave's spatial width, the exact source is yet to be ascertained. As observed in the inset of Fig. 4.5, secondary waves begin to form at a certain depth. As the primary wave regime 'R_1' decays exponentially, there is a layer at which the secondary wave's amplitude becomes higher than that of the primary wave. However, the primary wave's amplitude continues to decay exponentially, as indicated by the square markers in Fig. 6, while the peak is dictated by the secondary regime (circular markers). The above explanation holds for the transition between 'R_2' and 'R_3' regimes as well, as indicated by the triangular markers in Fig. 4.6.

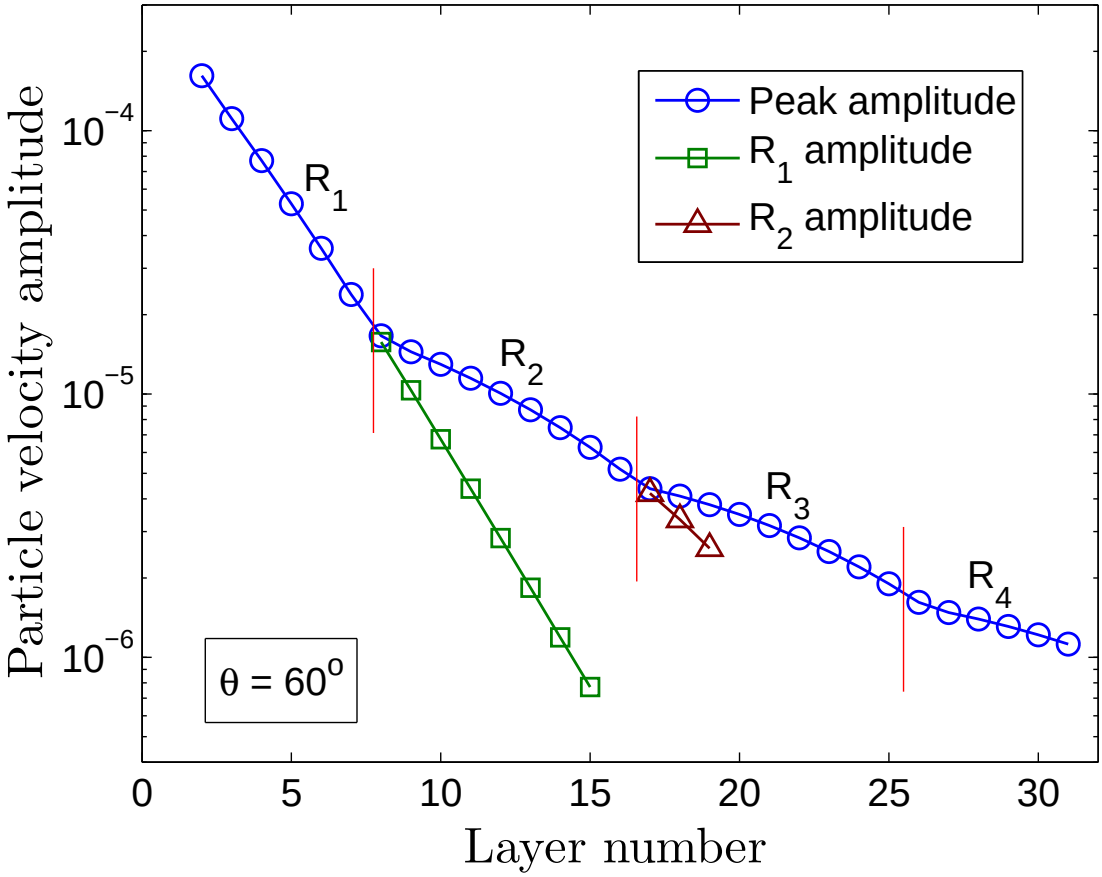

Figure 4.6: Variation of peak amplitudes of particle velocity v_{px} with depth demonstrating various regimes of decay R_1 to R_4. Regimes with square and triangular markers show amplitudes of R_1 and R_2, respectively, after the secondary waves govern the peak amplitude (Fig. 4.5).

Figure 4.7 illustrates the dependence of the wavefront speed on the contact force amplitude for various impact angles. We note that the wavefront refers to the leading pulse that propagates after the shearing component decays completely. Thus, the relations derived earlier for the normal impact case can be employed for wavefront speed prediction. The solid curve in Fig. 4.7 corresponds to the approximate analytical dependence given by Eq. (4.11), or equivalently the normalized curve in Fig. 4.3. As expected, there is a good agreement between the simulations and the analytical prediction. As the impact angle θ decreases, the force amplitude and the wavefront speed decrease since more energy is contributed to the horizontal motion

of the spheres in the initial few layers, as discussed earlier.

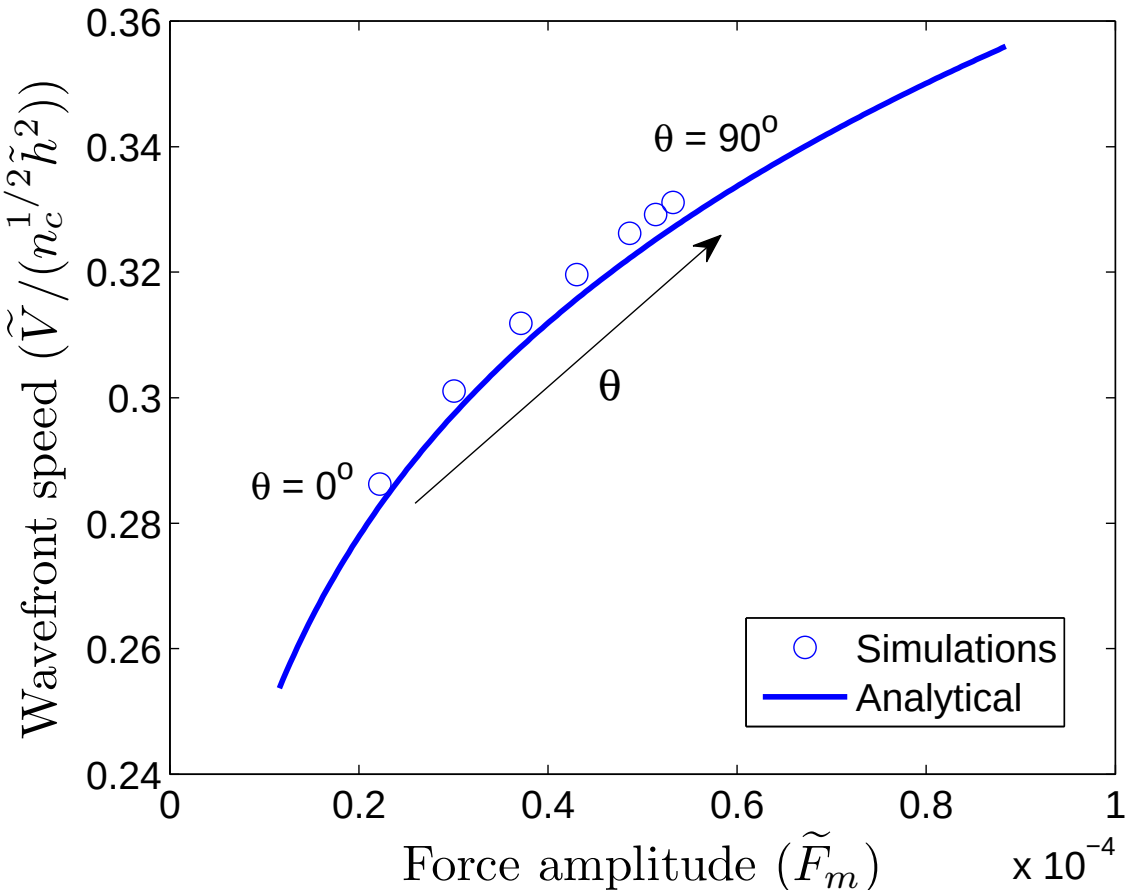

Figure 4.7: Wavefront speed as a function of its force amplitude for the 2D hexagonal packing for various impact angles θ ranging from 0° to 90°, comparing with the analytical (solid) normalized curve of Fig. 4.3.

4.3.2 Analytical predictions

Amplitude of leading pulse

The force amplitude of the leading pulse can be predicted by estimating the energy carried by the leading pulse after the impact of the topmost layer. To this end, consider a two-layered periodic system of hexagonal packing as shown in Fig. 4.8. The layer marked '1' impacts layer '2' at an angle θ to the horizontal, while layer '2' is free to move. The velocity of the second layer after impact can be obtained

for angles $0^\circ \leq \theta \leq 30^\circ$, where the problem is equivalent to an oblique impact of two spheres. The free-flight velocity of the second layer after impact can then be obtained by the conservation of linear momentum and energy as

$$v_{p2} = v_{p0}\cos(60^\circ - \theta) = \frac{v_{p0}}{2}\left(\cos\theta + \sqrt{3}\sin\theta\right), \tag{4.15}$$

where v_{p0} is the initial velocity magnitude of the topmost layer and θ is as defined in Fig. 4.1(a). Let us assume that the kinetic energy carried by the second layer in the above analysis is approximately equal to the energy carried by the leading pulse (denoted by E_θ) in the infinite-layer system. We then obtain

$$E_\theta \propto v_{p2}^2 = \frac{v_{p0}^2}{4}\left(3 - 2\cos^2\theta + \sqrt{3}\sin 2\theta\right). \tag{4.16}$$

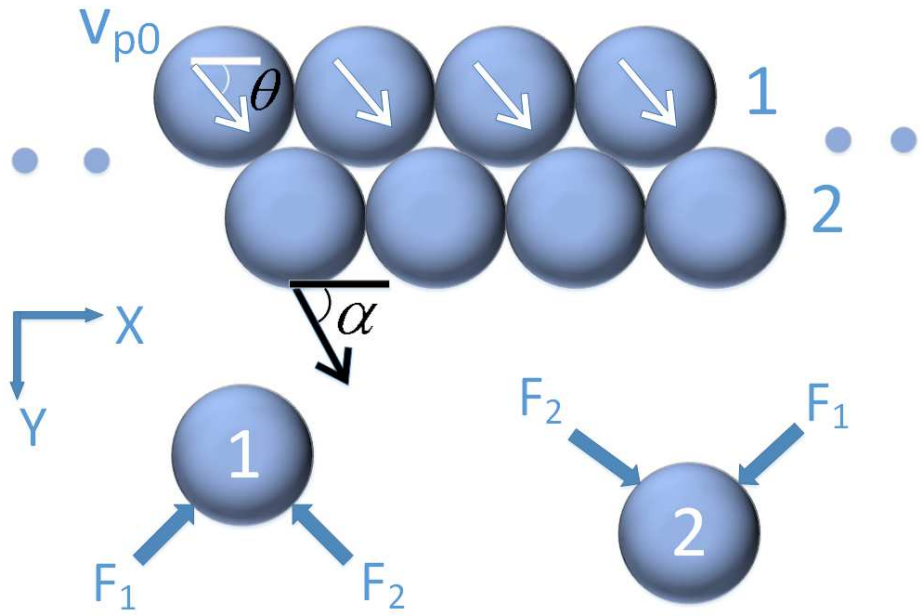

Figure 4.8: Two-layered hexagonal packing periodic in x-direction used in theoretical prediction of shear decay, and the resulting contact forces (marked F_1 and F_2) on the spheres in layers '1' and '2'. Layer '1' impacts at an angle θ to the horizontal and layer '2' is free to move.

The energy E_θ in Eq. (4.16) can be normalized with that of the normal impact case (E_0), for which the entire impact energy is transmitted (neglecting the small initial reflection), i.e., $E_0 \propto v_{p0}^2$. Finally, we introduce the scaling relation between the energy and the force amplitude of a solitary wave, $E \propto F_m^{5/3}$. The force amplitude of the leading pulse when $0^\circ \leq \theta \leq 30^\circ$ ($F_{m\theta}$) normalized by that of the normal impact (F_{m0}) is then given by

$$\frac{F_{m\theta}}{F_{m0}} \approx \left[\frac{1}{4}\left(3 - 2\cos^2\theta + \sqrt{3}\sin 2\theta\right)\right]^{3/5}. \tag{4.17}$$

Figure 4.9 shows a comparison between the force amplitude-impact angle dependence of the leading pulse obtained numerically and that described by Eq. (4.17). We find a good agreement between the simulations and the analytical result for angles $\theta \leq 30^\circ$ (left of dashed line), as expected. For $\theta > 30^\circ$, the spheres in the topmost layer will form two contacts with the corresponding spheres in the second layer, rendering the approximation (4.17) inapplicable. The analytical prediction gives an upper bound because the infinite-layer system "loses" energy at every interface of initial few layers due to oblique impact, whereas the analytical prediction accounts for only two layers. Nevertheless, the bulk of the rebound energy is carried by the topmost layer, as also confirmed by Fig. 4.9.

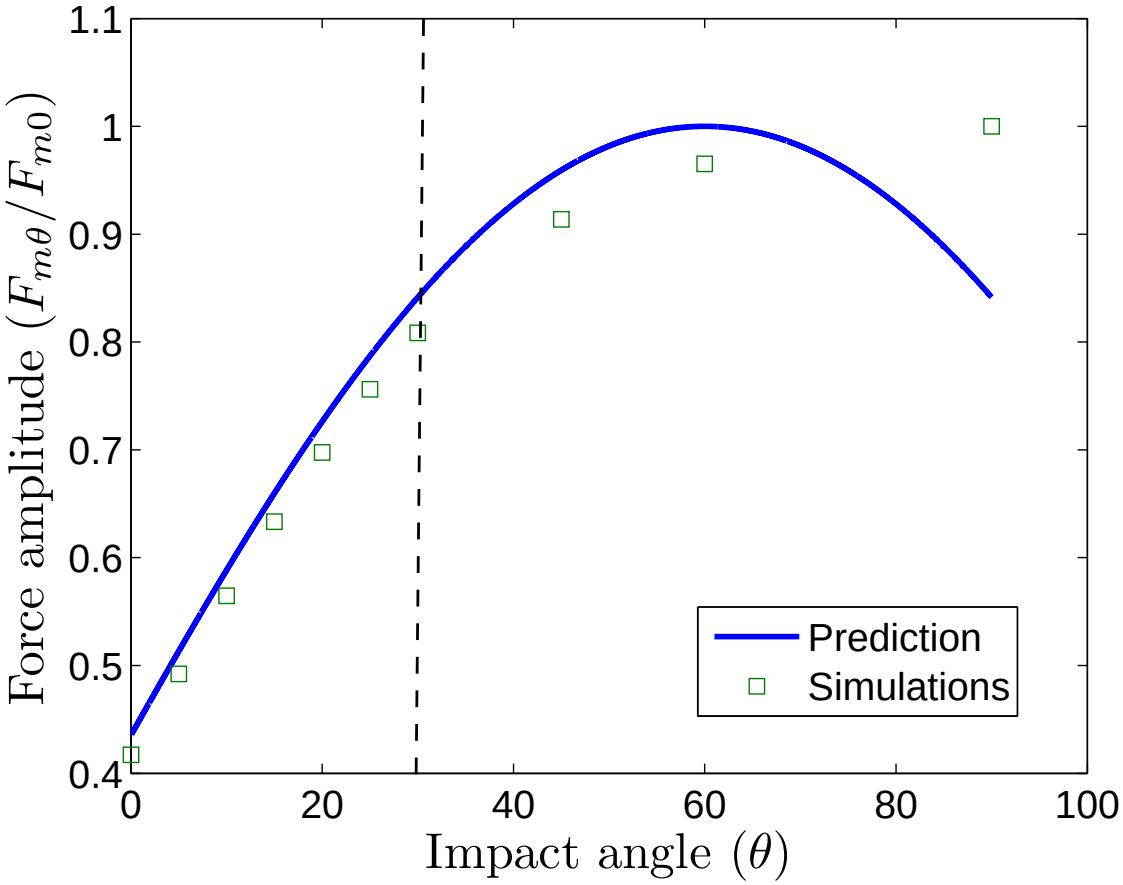

Figure 4.9: Force amplitude of the leading pulse for various impact angles θ ($F_{m\theta}$) normalized by that of normal impact case (F_{m0}). The dashed line denotes the maximum value of θ (= 30°) for which the theoretical prediction (4.17) is expected to be valid.

Shear component decay

In Sec. 4.3.1, we discussed the rapid attenuation of the shearing effect and Fig. 4.6 showed the rate of decay of the x-component of the particle velocity with depth. In this section, an iterative procedure based on the two-layered model (Fig. 4.8) is employed to predict the decay of the shearing effect. The idea is to find the direction of travel (based on acceleration vector) of layer '2', which would then be considered as layer '1' (coming at the new θ) in the second iteration. The above steps are repeated until the shearing component has decayed, i.e., until the impacted layer

'2' travels at an angle within a specified tolerance of 90°, which corresponds to the normal impact case.

Let us define α as the angle the force (or acceleration) vector of layer '2' in Fig. 4.8 makes with the horizontal. Writing the force vector with components F_x and F_y as a function of the contact forces F_1 and F_2, one gets

$$\tan\alpha = \frac{F_y}{F_x} = \sqrt{3}\left(\frac{F_1 + F_2}{F_2 - F_1}\right). \tag{4.18}$$

Then consider the force-particle velocity scaling relation given by $F \propto v_p^{6/5}$, where F is the contact force between any two spheres and v_p is the velocity of approach (defined as the difference between the two velocities). In Fig. 4.8, let the initial velocity magnitude of layer '1' be v_{p0}. As a first approximation, let us neglect the coupling effect of the two contact forces F_1 and F_2 and write the scaling relations independently. Thus, the velocities of approach for the two contact forces F_1 and F_2 are $v_{p0}cos(120^\circ - \theta)$ and $v_{p0}cos(60^\circ - \theta)$, respectively, leading to

$$\begin{aligned} F_1 &\propto [v_{p0}\cos(120^\circ - \theta)]^{6/5} \\ F_2 &\propto [v_{p0}\cos(60^\circ - \theta)]^{6/5}. \end{aligned} \tag{4.19}$$

Equation (4.18) becomes

$$\tan\alpha \approx \sqrt{3}\left(\frac{[\cos(60^\circ - \theta)]^{6/5} + [\cos(120^\circ - \theta)]^{6/5}}{[\cos(60^\circ - \theta)]^{6/5} - [\cos(120^\circ - \theta)]^{6/5}}\right). \tag{4.20}$$

In the second iteration, the α from Eq. (4.20) is taken as the new θ, where layer '2' impacts layer '3' and so on. Figure 4.10 illustrates the variation of angle α with depth (or layer number) comparing the results from the above iterative procedure (labeled 'prediction') with those of the simulations for two initial angles of impact $\theta = 60^\circ$ and $\theta = 80^\circ$. Simulations correspond to the full system in

Fig. 4.1(a), and α is calculated at the time step when the particles start moving in each layer. Overall, the analytical predictions and simulations agree reasonably well, particularly the analytical predictions for the distance to approach 90° correspond very well with the simulations. Small differences observed arise from the fact that there is coupling effect between the two contact forces (F_1 and F_2) and the analytical procedure considers only two layers at a time.

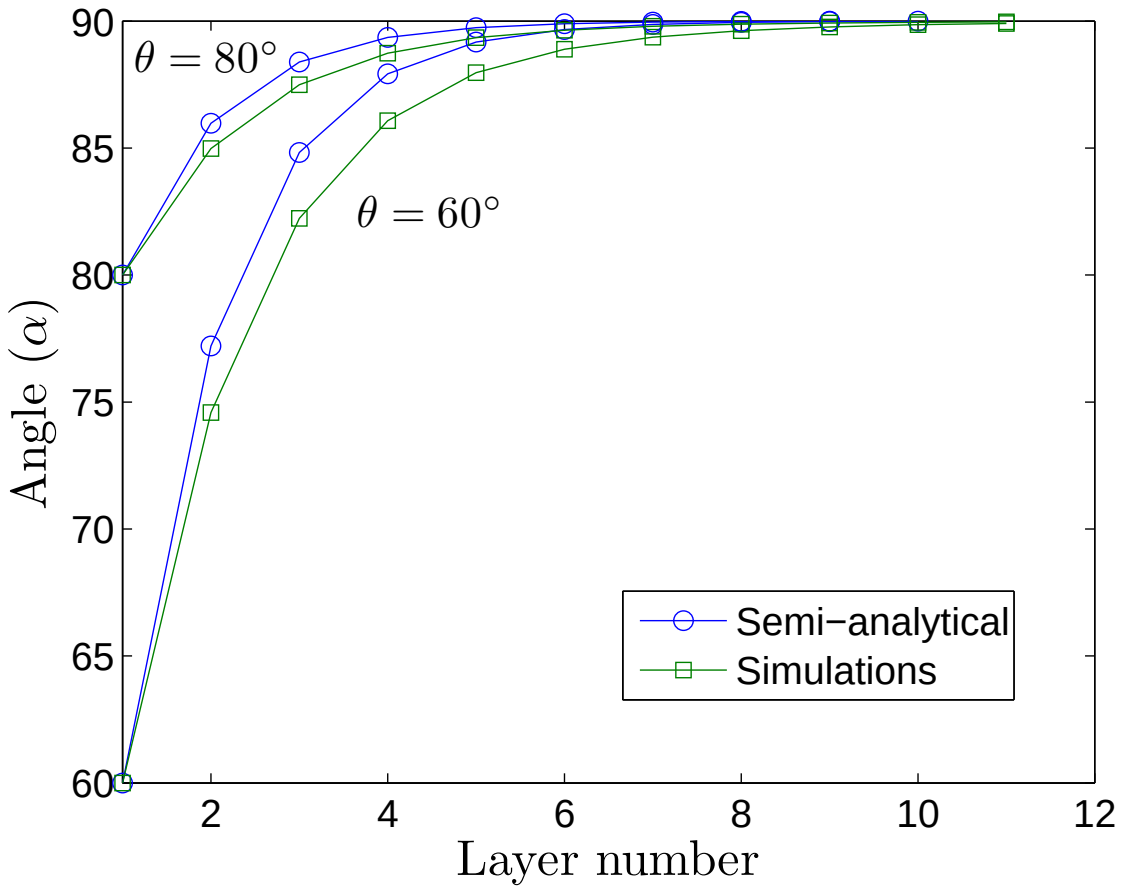

Figure 4.10: Semi-analytical predictions for the two-layered system of Fig. 4.8, showing the angle α as a function of depth for two different impact angles: $\theta = 60°$ and $\theta = 80°$. Simulations consider the full domain of Fig. 4.1(a).

Exponential regime decay rate

In this section, another iterative procedure is developed to predict the decay rate of the exponential regime, as observed in Fig. 4.6. As before, we consider the two-layered periodic system of hexagonal packing as shown in Fig. 4.8. Here, a set of ordinary differential equations are obtained to predict the free-flight velocity of layer '2', and the procedure is repeated iteratively. The exponential decay rate is then determined based on the ratio of final x-velocity of layer '2' to initial x-velocity of layer '1' at each iteration.

Let u_i and v_i be the x- and y-displacements of i^{th} layer ($i = 1, 2$). The equations of motion are therefore given by

$$\begin{aligned} m\ddot{u}_1 &= \frac{1}{2}(F_1 - F_2), \qquad m\ddot{u}_2 = \frac{1}{2}(F_2 - F_1), \\ m\ddot{v}_1 &= -\frac{\sqrt{3}}{2}(F_1 + F_2), \quad m\ddot{v}_2 = \frac{\sqrt{3}}{2}(F_1 + F_2). \end{aligned} \tag{4.21}$$

For convenience, let us define new variables $u = u_1 - u_2$ and $v = v_1 - v_2$. The Eqs. (4.21) reduce to

$$\begin{aligned} m\ddot{u} &= F_1 - F_2, \\ m\ddot{v} &= -\sqrt{3}(F_1 + F_2). \end{aligned} \tag{4.22}$$

The contact forces F_1 and F_2 can be written in terms of the displacements by using Eq. (4.4), where the relative displacement δ is derived similar to Eq. (4.3) by including

x-displacements as well. Finally, one gets

$$\begin{aligned} F_1 &= K\left[\frac{1}{2}\left(u_2 - u_1 + \sqrt{3}v_1 - \sqrt{3}v_2\right)\right]^{3/2} \\ &= \frac{K}{2^{3/2}}\left(-u + \sqrt{3}v\right)^{3/2}, \\ F_2 &= K\left[\frac{1}{2}\left(u_1 - u_2 + \sqrt{3}v_1 - \sqrt{3}v_2\right)\right]^{3/2} \\ &= \frac{K}{2^{3/2}}\left(u + \sqrt{3}v\right)^{3/2}. \end{aligned} \tag{4.23}$$

Substituting Eqs. (4.23) in the reduced equations of motion (Eq. (4.22)) leads to

$$\begin{aligned} m\ddot{u} &= \frac{K}{2^{3/2}}\left[\left(-u + \sqrt{3}v\right)^{3/2} - \left(u + \sqrt{3}v\right)^{3/2}\right], \\ m\ddot{v} &= -\sqrt{3}\frac{K}{2^{3/2}}\left[\left(-u + \sqrt{3}v\right)^{3/2} + \left(u + \sqrt{3}v\right)^{3/2}\right]. \end{aligned} \tag{4.24}$$

We can now consider the Taylor series expansion of the right hand side of Eqs. (4.24) with the assumption that $\sqrt{3}v \gg u$, later shown to be a good assumption. The first Eq. (4.24) yields

$$\begin{aligned} \ddot{u} &= \frac{K}{m}\frac{(\sqrt{3}v)^{3/2}}{2^{3/2}}\left[\left(1 - \frac{u}{\sqrt{3}v}\right)^{3/2} - \left(1 + \frac{u}{\sqrt{3}v}\right)^{3/2}\right] \\ &= \frac{K}{m}\frac{(\sqrt{3}v)^{3/2}}{2^{3/2}}\left[-3\frac{u}{\sqrt{3}v} + O\left(\frac{u^3}{v^3}\right)\right]. \end{aligned} \tag{4.25}$$

Similarly, the second Eq. (4.24) can be rewritten as

$$\begin{aligned} \ddot{v} &= -\frac{K}{m}\frac{\sqrt{3}(\sqrt{3}v)^{3/2}}{2^{3/2}}\left[\left(1 - \frac{u}{\sqrt{3}v}\right)^{3/2} + \left(1 + \frac{u}{\sqrt{3}v}\right)^{3/2}\right] \\ &= -\frac{K}{m}\frac{\sqrt{3}(\sqrt{3}v)^{3/2}}{2^{3/2}}\left[2 + \frac{1}{4}\frac{u^2}{v^2} + O\left(\frac{u^4}{v^4}\right)\right]. \end{aligned} \tag{4.26}$$

Retaining terms up to second order in u/v, the final form of the system of ordinary

differential equations (ODEs) is

$$\begin{aligned} \ddot{u} &\approx -\frac{3^{5/4}}{2^{3/2}}\frac{K}{m}\left(u\sqrt{v}\right), \\ \ddot{v} &\approx -\frac{3^{5/4}}{2^{3/2}}\frac{K}{m}\left(2v^{3/2}+\frac{1}{4}u^2v^{-1/2}\right). \end{aligned} \tag{4.27}$$

This system of coupled ODEs is then numerically integrated to obtain the evolution of the displacement variables (u and v) and the velocity variables ($\dot{u}$ and $\dot{v}$). The initial conditions are chosen corresponding to $v_{p0} = 1$ m/s ($v_{p0} = 5.6336 \times 10^{-4}$ in nondimensional units) and $\theta = 60°$, leading to

$$\begin{aligned} u(0) &= 0, \qquad \dot{u}(0) = v_{p0}cos(\theta), \\ v(0) &= 0, \qquad \dot{v}(0) = v_{p0}sin(\theta). \end{aligned} \tag{4.28}$$

Figures 4.11 and 4.12 show the evolution of displacement and velocity variables, respectively, and compare the solution of the ODEs (Eq. (4.27)) to those of the discrete simulations, showing a very good agreement. We are particularly interested in the velocity variable $\dot{u}$ to predict the decay rate of x-velocity, and thus we can proceed with the iterative procedure described earlier to obtain the exponential decay rate. We also note that, in Fig. 4.12, the final value of the velocity variable $\dot{v}$ from the ODEs is slightly different from that of the simulations. There are mainly two sources of this deviation. Firstly, the initial assumption that $\sqrt{3}v \gg u$ breaks down after a certain time in the displacement variable v (Fig. 4.11). And secondly, one of the contacts in Fig. 4.8 will separate before the other, and hence the system of equations (4.21) may not fully capture this effect.

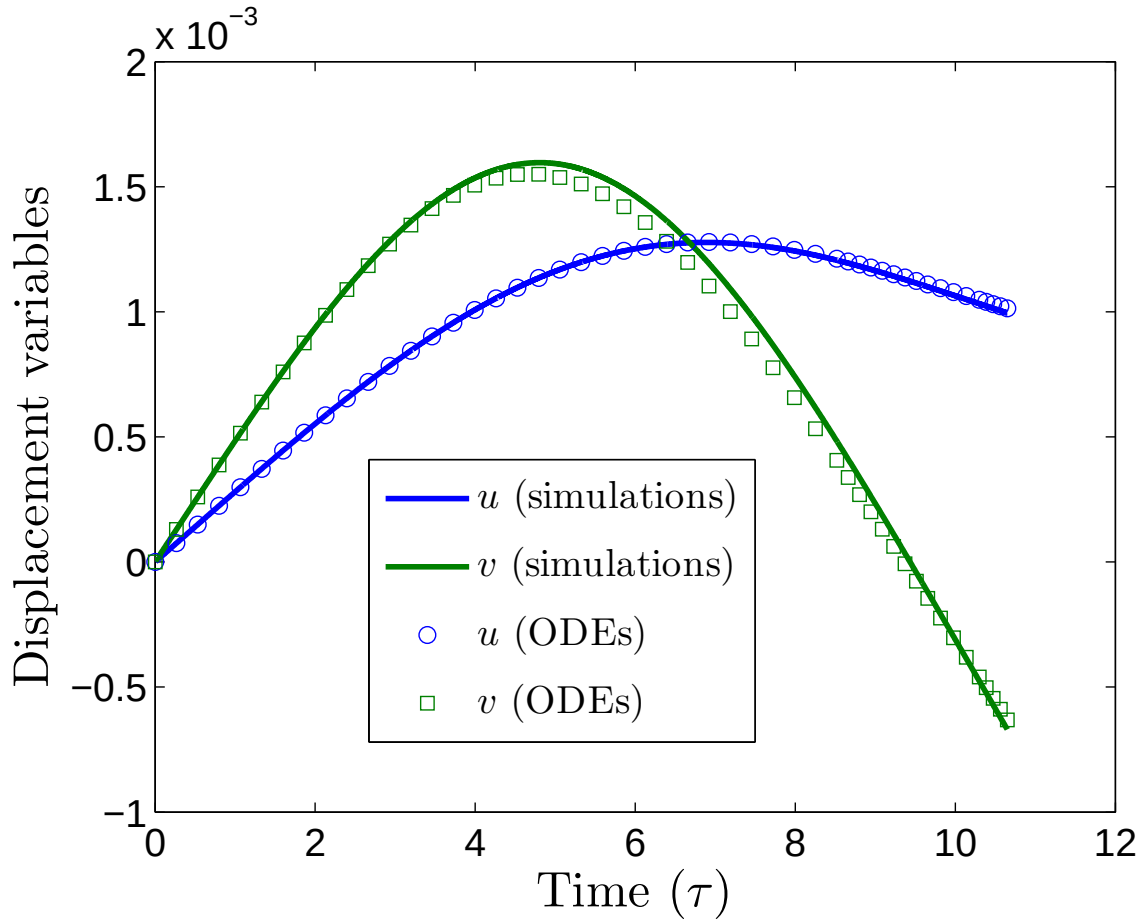

Figure 4.11: History of displacement variables u and v showing a comparison between the solution of the ODEs in Eq. (4.27) and that of the simulations for the same two-layered structure (Fig. 4.8).

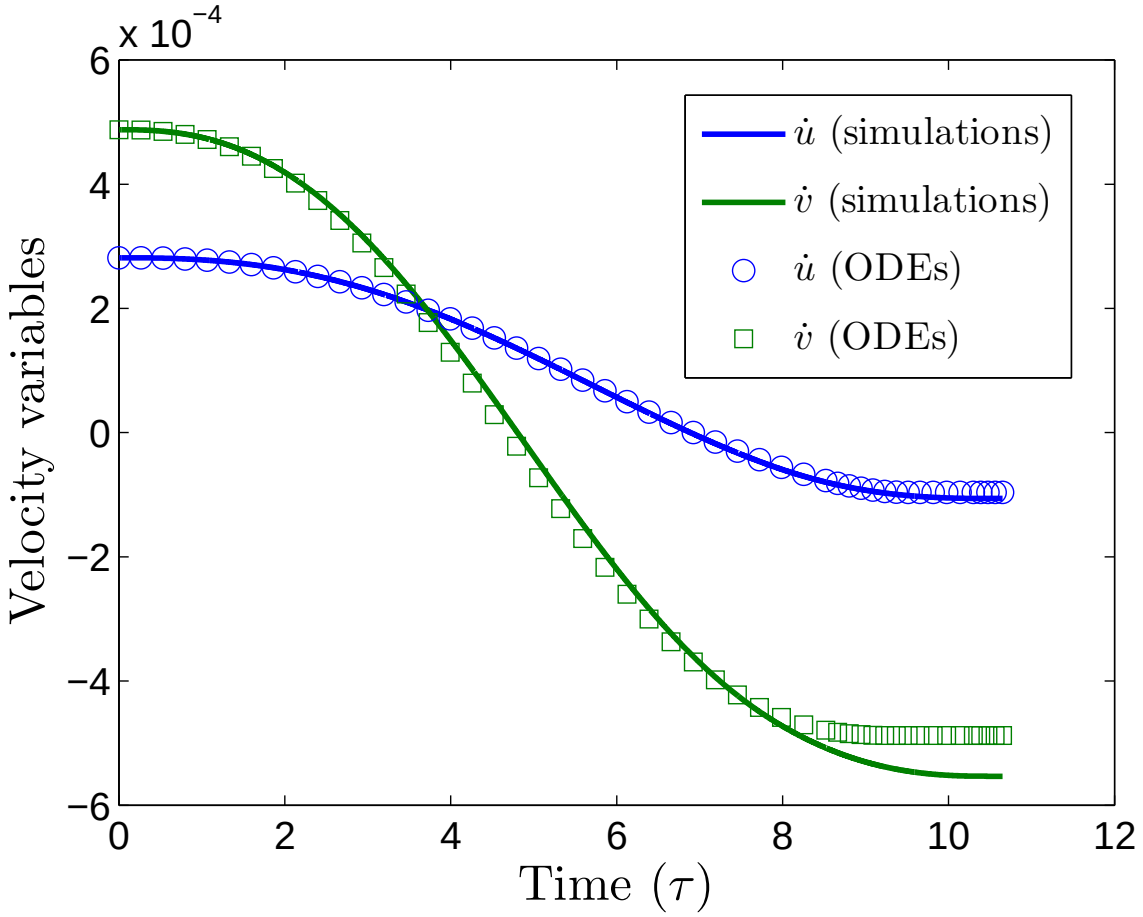

Figure 4.12: History of velocity variables $\dot{u}$ and $\dot{v}$ from the simulation of Fig. 4.8 and numerical solution of the ODEs (4.27).

Let us extract the free flight x-velocity of layer '1' and '2' ($\dot{u}_1$ and $\dot{u}_2$) by employing the conservation of linear momentum and the final asymptote value for $\dot{u}$ in Fig. 4.12. The relevant equations for iteration i are

$$\begin{aligned} \dot{u}_{1_i} + \dot{u}_{2_i} &= \dot{u}_{2_{i-1}}, \\ \dot{u}_{1_i} - \dot{u}_{2_i} &= \dot{u}_i, \end{aligned} \tag{4.29}$$

where $\dot{u}_{2_0} = 2.8168 \times 10^{-4}$. Then the ratio $q = \dot{u}_{2_i}/\dot{u}_{2_{i-1}}$ gives a measure of the

exponential decay rate (r, defined as $u_2(y) \propto \exp[-ry]$) as given by

$$q = \frac{\dot{u}_{2_i}}{\dot{u}_{2_{i-1}}} \approx \frac{e^{-r\sqrt{3}Ri}}{e^{-r\sqrt{3}R(i-1)}} = e^{-r\sqrt{3}R}. \tag{4.30}$$

The results for the first three iterations are tabulated in Table 4.1. For the numerical results, an exponential curve fit to the regime R_1 in Fig. 4.6 gives a decay rate $r = 42.61$ m^{-1}. Thus the analytical predictions in Table 4.1 approximately differ by 8% from the numerical results. One can possibly reduce the error by taking higher-order terms in the ODEs (4.27).

Table 4.1: Decay rate at each iteration from the solution of the ODEs (4.27).

Iteration	$\dot{u}_{2_{i-1}}$ ($\times 10^{-4}$)	$\dot{u}_{2_i}$ ($\times 10^{-4}$)	$q = \dot{u}_{2_i}/\dot{u}_{2_{i-1}}$	r
1	2.8168	1.8889	0.6706	46.14
2	1.8889	1.2664	0.6704	46.17
3	1.2664	0.8490	0.6704	46.17

4.4 Conclusions

Numerical and theoretical studies were performed on the effect of uniform impact on wave propagation in 2D and 3D periodic monodisperse elastic granular media such as hexagonal, FCC and BCC structures. For the normal impact case, equivalent 1D chains based on theoretical considerations were obtained for the 2D and 3D granular structures. In particular, relations between the wavefront speed and its force amplitude for the 2D and 3D structures were found to be similar to that of a homogeneous chain. Furthermore, the analytical solutions were found to be in very good agreement with the numerical results, and an universal normalized relation between the wavefront speed and its force amplitude was found to be valid for all the granular structures considered in the present study.

Studies on angular impact of 2D hexagonal packing were also investigated to

understand the effect of shear loading. Numerical study revealed that the shearing effect attenuates quickly to a state similar to that of the normal impact case. Further, the amplitude of the horizontal (shear) component of particle velocity was found to decay in several regimes such as an initial exponential regime and later a series of linear regimes. By employing a simplified two-layered model, several theoretical considerations showed good comparison with the simulations. The force amplitude of the leading pulse (for a limited range of impact angle) was predicted by determining energy of the leading pulse and then using the energy-force scaling relation. The direction of propagation of each layer was predicted by applying the force-particle velocity scaling relation, demonstrating rapid shift to the normal impact state. Finally, the exponential regime decay rate was determined based on an approximate system of ODEs for the two-layered system.

In closing, it should be mentioned that the energy dissipation associated with friction would lead to a higher decay rate of the shear component of the force and velocity. The value of the decay rate obtained in the present study therefore corresponds to a lower bound.

Chapter 5

Plane wave propagation in dimer granular media

One of the limitations of the monodisperse granular media is that the system always gives rise to energy-preserving solitary waves. We can only have the capability of changing the magnitude of the response based on the geometric and material properties. In order to obtain a different response, i.e., an energy-decaying response, we need to introduce a second set of spheres with different geometric and material properties. Few studies on dimer granular chains have successfully shown the capability to change the response from a solitary wave to energy-decaying wave [39]. The following work elicits motivation from dimer chains and extends the study on plane wave propagation in monodisperse granular media (Chapter 4) to bidisperse granular media to derive more flexibility in altering the response of the system. In the present study, we perform a numerical and theoretical investigation of plane wave propagation in square packing granular media with intruders at interstitial locations. We explore the existence of an equivalent 1D 'nonlocal chain' for the bidisperse system and carry out numerous simulations to systematically investigate plane wave propagation behavior. We demonstrate the existence of a new set of solitary waves in periodic dimer granular crystals. The current study also demonstrates different ways in which the bidisperse system can help mitigate or preserve the force amplitude of the wave.

For the square packing system with intruders at interstitial positions, an equivalent 1D chain has been identified analytically and verified with numerical simulations. The system is normalized to obtain two nondimensional parameters which

are functions of mass ratio between the larger and smaller spheres and stiffness ratio between the two types of contacts, respectively. We find that there is one set of discrete combinations of the nondimensional parameters for which there is maximum decay of force amplitude while there is another set of values that preserve the original impulse. The latter case is particularly interesting where the square packing system allows solitary waves for certain discrete combinations although the system is inhomogeneous. Out of several solitary waves possible, there is one case where the velocity profiles of both larger and smaller spheres are similar to that of a homogenous chain. Some analytical procedures similar to that of homogeneous chains such as quasi-continuum approach and asymptotic analysis are considered to predict the wavefront speed and wave width, and the theoretical results show good agreement with the numerical simulations. Eight distinct solitary waves have been systematically extracted from the simulations to construct a 'solitary wave map' illustrating the nondimensional parameters that give rise to each of these waves.

The following sections form the remainder of the chapter: Section 5.1 provides the problem statement and its numerical implementation. In Sec. 5.2.1, we determine an equivalent 1D chain for the bidisperse system and verify its formulation. Sections 5.2.2 and 5.2.3 summarize some of the key numerical observations. In Sec. 5.3, analytical techniques such as the quasi-continuum approximation and an asymptotic analysis are used to predict some of the key phenomena observed numerically. The results of the above study has been published in the journal *Physical Review E* ("Family of plane solitary waves in periodic dimer crystals." *Physical Review E* 90.3 (2014): 032209) and the remainder of this chapter follows in most part that reference.

5.1 Problem statement

Consider a square packing system of spherical particles with spherical intruders placed at interstitial locations as shown in Fig. 5.1(a). The granular system is periodic in the lateral direction ('x') and 'semi-infinite' in the longitudinal direction ('y') so that the system is free from boundary effects. The equations of motion for sphere i and the definitions of the involved variables are given in Sec. 3.1. Because of the closed-packed nature of the system, the intruder spheres can have a maximum of four neighboring contacts while the main (larger) spheres can have upto eight contacts.

For the square packing system, the ratio of the radius of a smaller sphere (R_2) to a larger sphere (R_1) is $\sqrt{2}-1$. The material properties of the spheres such as density (ρ_1, ρ_2), Young's modulus (E_1, E_2) and Poisson's ratio (ν_1, ν_2) and the geometrical properties may vary based on the nondimensional parameters that will be discussed in the next section. All the spheres are assumed to be elastic and dissipative effects such as friction and damping are neglected. The simulations are performed using the molecular dynamics code LAMMPS (Large-scale Atomic/Molecular Massively Parallel Simulator) [61], where the spheres are interpreted as point masses while the contacts are simulated using nonlinear springs. An in-house code is also developed to simulate the dynamics in 1D granular chains, where the time integration is performed using the fourth-order Runge-Kutta method. The square packing system is then given a uniform perpendicular impact of velocity magnitude v_{p0} as shown in Fig. 5.1(a). Quantities such as the velocity of the particles and the force amplitude at various contacts are monitored during the simulations.

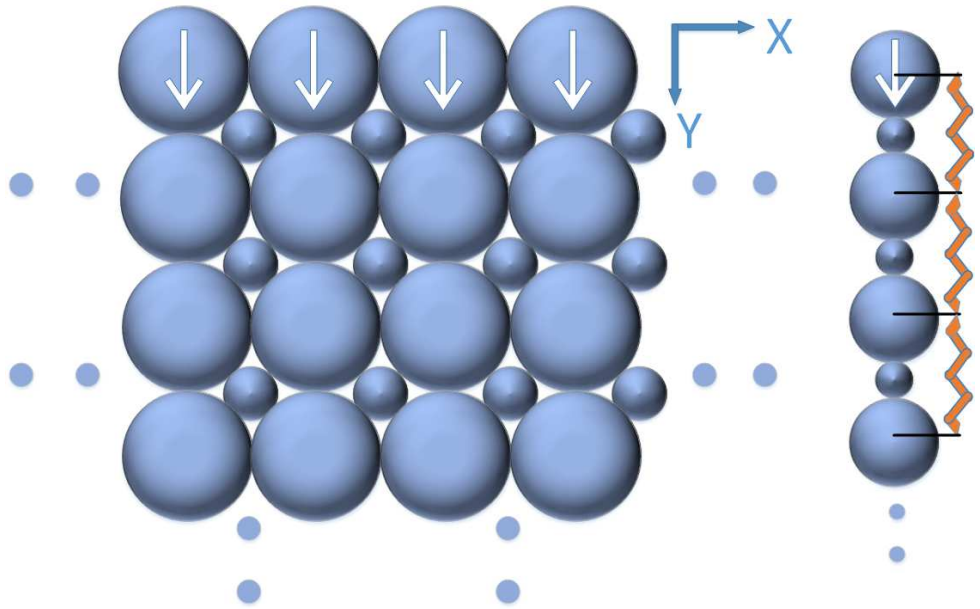

(a) (b)

Figure 5.1: (a) 2D square packing system of spheres with spherical intruders at interstitials. Arrows on the topmost layer indicate the planar initial velocity impulse. Periodicity is enforced in the x-direction while y-direction is semi-infinite. (b) The 1D chain with nonlocal interactions proposed as equivalent to the 2D system.

5.2 Numerical Results

5.2.1 Equivalent 1D system

Due to the periodicity enforced in the x-direction and the impact being planar perpendicular, the forces on the particles are symmetric with respect to the y-axis and thus the particles have displacements in the y-direction alone. Thus the governing equations of motion in the y-direction for the 2D square packing system with

intruders (Fig. 5.1(a)) are given by

$$\begin{aligned} m_1\ddot{\bar{u}}_i &= \sqrt{2}K_2\left(\frac{R_1}{R_1+R_2}\right)^{3/2}\left[(\bar{u}_{i-1}-\bar{u}_i)^{3/2}-(\bar{u}_i-\bar{u}_{i+1})^{3/2}\right] \\ &\quad + K_1\left[(\bar{u}_{i-2}-\bar{u}_i)^{3/2}-(\bar{u}_i-\bar{u}_{i+2})^{3/2}\right], \\ m_2\ddot{\bar{u}}_{i+1} &= \sqrt{2}K_2\left(\frac{R_1}{R_1+R_2}\right)^{3/2}\left[(\bar{u}_i-\bar{u}_{i+1})^{3/2}-(\bar{u}_{i+1}-\bar{u}_{i+2})^{3/2}\right], \end{aligned} \tag{5.1}$$

where K_1 and K_2 are the contact stiffnesses for main-main and main-intruder spheres interactions, respectively, while m_1 and m_2 are the masses of the larger beads with displacements $\bar{u}_i$ and $\bar{u}_{i\pm2}$ and intruder beads with displacements $\bar{u}_{i\pm1}$, respectively. The vertical displacement ($\bar{u}$) and time (t) variables are nondimensionalized as

$$u = \frac{\bar{u}}{R_1} \quad \text{and} \quad \tau = \frac{t}{\left(\frac{m_1}{K_1\sqrt{R_1}}\right)^{1/2}}, \tag{5.2}$$

respectively, where u and τ are corresponding nondimensional variables. The equations of motion (5.1) can now be written in a nondimensional form, with the two parameters governing the dynamics of the system defined by

$$\varepsilon = \frac{m_2}{m_1} \quad \text{and} \quad \alpha = \frac{2^{-1/4}K_2}{K_1}. \tag{5.3}$$

All the results reported herein are valid for a wide range of material properties depending on the nondimensional parameters in Eq. (5.3). One can now write the equations of motion in nondimensional form as

$$\begin{aligned} \ddot{u}_i &= \alpha\left[(u_{i-1}-u_i)^{3/2}-(u_i-u_{i+1})^{3/2}\right] + \\ &\quad + \left[(u_{i-2}-u_i)^{3/2}-(u_i-u_{i+2})^{3/2}\right], \\ \varepsilon\ddot{u}_{i+1} &= \alpha\left[(u_i-u_{i+1})^{3/2}-(u_{i+1}-u_{i+2})^{3/2}\right]. \end{aligned} \tag{5.4}$$

Since the system is periodic, the dynamics is essentially one-dimensional and

therefore one can think of an equivalent 1D chain that would give the same dynamic response as the 2D system. Observing the equations of motion for the 2D system, we propose the nonlocal dimer chain shown in Fig. 5.1(b) as the equivalent 1D chain for the 2D system in Fig. 5.1(a). A heavy (larger) sphere in the 1D chain interacts with the neighboring light (smaller) spheres as well as the nearest heavy spheres, giving rise to the nonlocal effect. The governing equations of motion for the 1D chain are therefore similar to Eqs. (5.4) with nondimensional parameters redefined as

$$\widetilde{\varepsilon} = \varepsilon \qquad \text{and} \qquad \widetilde{\alpha} = 2^{1/4}\alpha. \tag{5.5}$$

We now verify the equivalence suggested by the above scaling relations by conducting numerical simulations for the 1D and 2D systems of Fig. 5.1. The 2D system is simulated using LAMMPS with real material properties while the 1D chain is simulated using Eqs. (5.4) and the scaling relations (5.5). Consider the 1D and 2D systems of the same length, i.e., same number of heavy and light spheres, with the first sphere (or first layer in 2D) given an initial velocity impulse. Figure 5.2 shows the particle velocity histories nondimensionalized according to Eq. (5.2) of heavy and light spheres at locations 30 and 31, respectively, in a chain of 50 spheres for $\varepsilon = 0.07107$ and $\alpha = 0.6436$ ($R_1 = 5$ mm and material properties corresponding to steel) for both 1D and 2D systems. As apparent there, the results for the 1D chain (solid lines) overlap with that of the 2D system (markers). In summary, we have demonstrated that the nonlocal dimer chain in Fig. 5.1(b) is equivalent to the 2D system in Fig. 5.1(a) with appropriate scaling of material properties as suggested by Eq. (5.5).

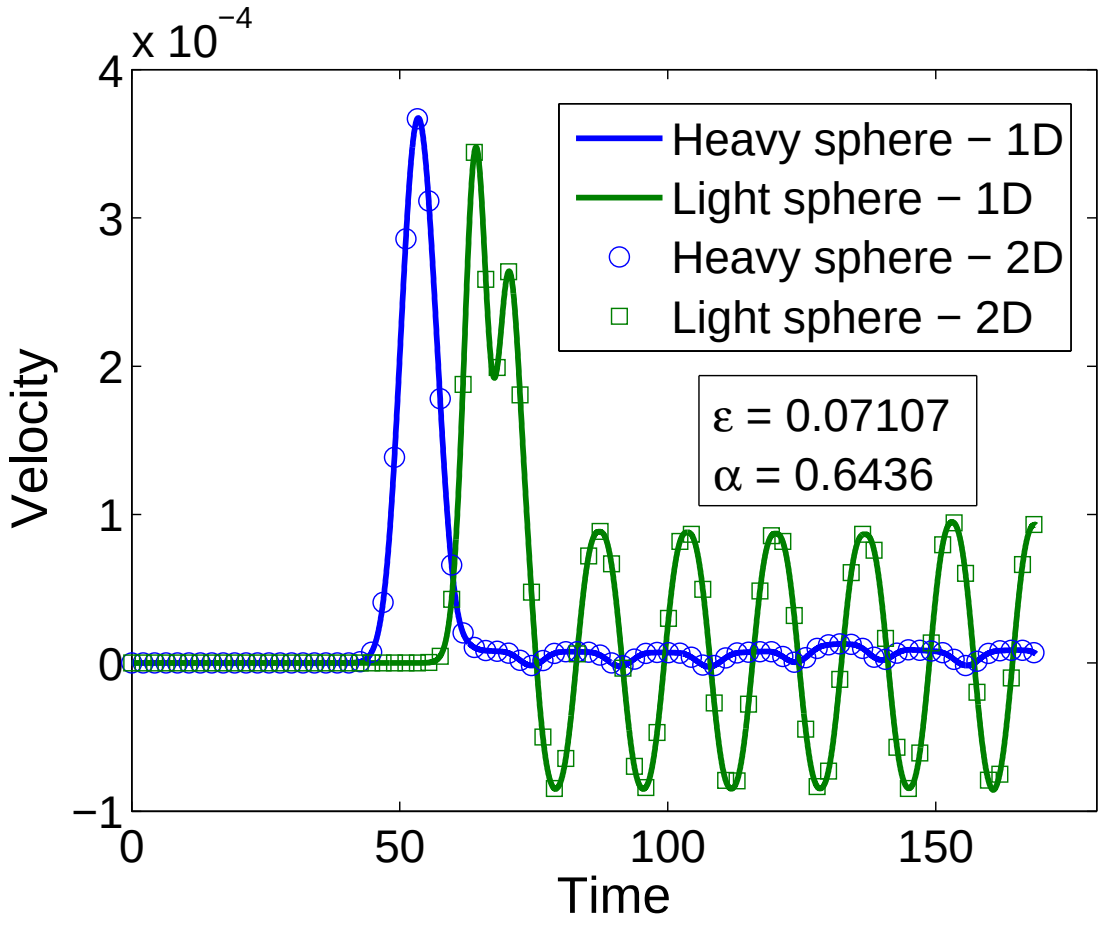

Figure 5.2: Nondimensional particle velocity histories for the heavy and light spheres for the 1D (solid lines) and 2D (markers) systems (Fig. 5.1) demonstrating the equivalence between the two responses.

5.2.2 Numerical observations

Figure 5.2 also demonstrates a typical response of the nonlocal dimer chain for arbitrary values of ε and α. After the primary compressive pulse propagation, the light sphere oscillates between its neighboring heavy spheres. The heavy spheres also oscillate but with a very low amplitude compared to that of the light sphere. A oscillating tail is also observed in the local dimer chain (absence of nonlocal interactions) [39] for arbitrary values of ε. The energy carried by the leading pulse gradually reduces as it is 'leaking' to the tail and thus the velocity (or force) amplitude reduces

with propagating distance. We expect such a decaying response because of the inhomogeneous nature of the system, but the dynamics of the local dimer chain has revealed the existence of discrete values of ε for which the system permits solitary waves [39]. Therefore, we investigate whether the nonlocal dimer system realizes solitary waves similar to that of the local dimer system. The nonlocal dimer chain in the present study has two parameters ε and α that dictate the dynamics and therefore offers richer scenarios to probe the presence of solitary waves.

Consider an equivalent nonlocal dimer chain (Fig. 5.1(b)) of 100 spheres. The mass ratio ε is varied but we fix $\alpha = 0.6436$. The heavy sphere at the left end of the chain is given a (nondimensional) velocity impulse of 5.63×10^{-4}. Figure 5.3 shows the particle velocity variation with time for neighboring heavy and light spheres for one case of $\varepsilon = 0.05250$. As evident there, a solitary wave is realized in the system since both the spheres have zero velocities immediately after the primary pulse propagation. The heavy sphere's velocity profile resembles that of a sphere in a homogeneous chain while the light sphere's profile has multiple peaks, similar to the local dimer chain. In Fig. 5.2, the non-vanishing tail implied that the light sphere was incapable of transferring the incoming energy from the previous heavy sphere to the next heavy sphere. Whereas in Fig. 5.3, the light (heavy) sphere completely transfers the incoming energy to the next heavy (heavy and light) sphere(s). Also, the light sphere's amplitude is smaller than that of the heavy sphere but, as we shall discuss later, the opposite can also be true depending on the parameters ε and α.

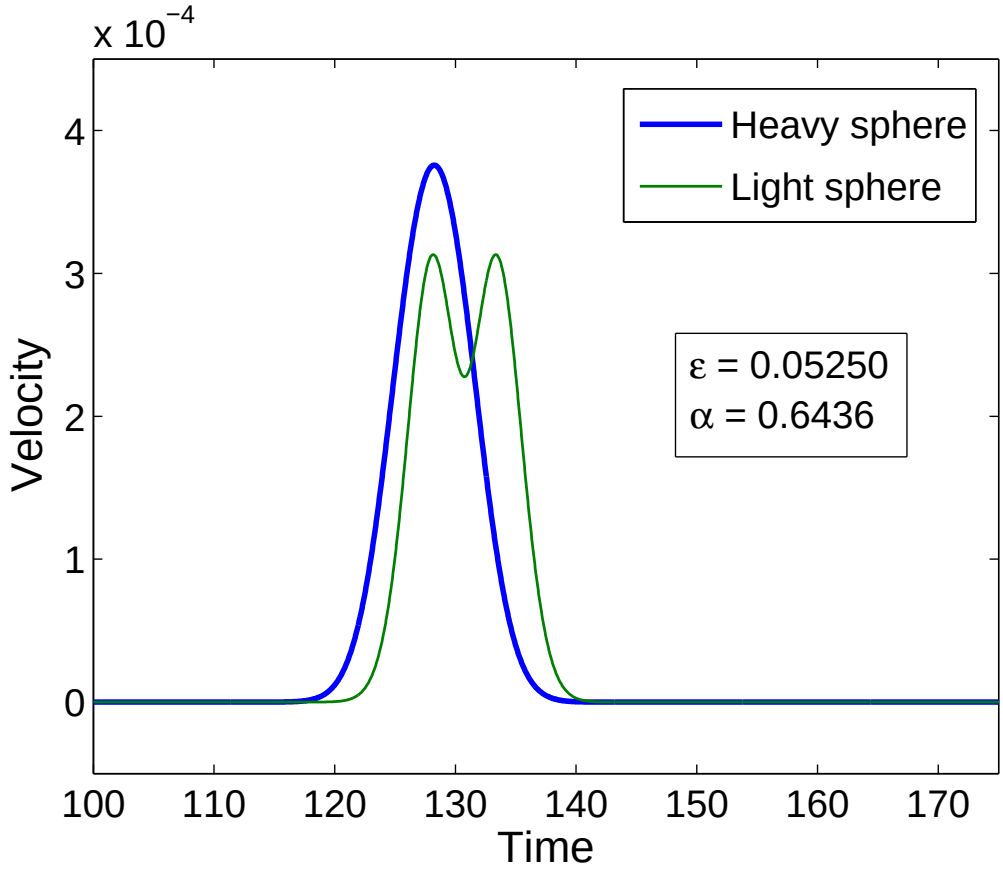

Figure 5.3: Particle velocity histories of heavy and light spheres for $\varepsilon = 0.05250$ and $\alpha = 0.6436$, showing the existence of a solitary wave.

5.2.3 Extraction of solitary waves

In Fig. 5.3, a particular case of solitary wave in the nonlocal dimer system was depicted. We now turn our attention to the systematic determination of solitary waves over a wide range of material properties defined by ε and α. The procedure employed to identify the solitary wave regimes is described hereafter.

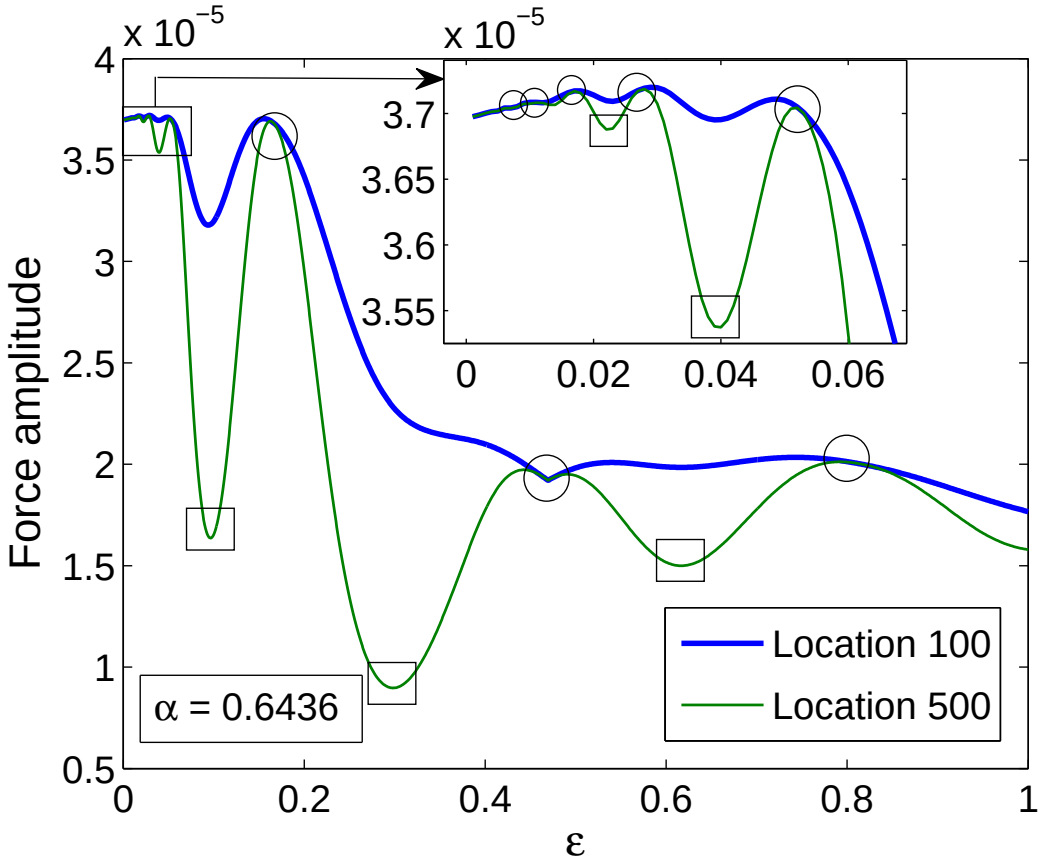

Figure 5.4: Force amplitudes as a function of ε at locations 100 and 500 for $\alpha = 0.6436$ in the nonlocal dimer chain. The inset shows the variation near zero for clarity. Circular markers show the discrete values of ε with approximately zero attenuation, while the square markers indicate locally maximum decay.

Consider a long nonlocal dimer chain of 520 spheres. As in Fig. 5.3, $\alpha = 0.6436$ is kept constant while ε ranges from 0 to 1. As noted in Ref. [39], the case of $\varepsilon \to 0$ corresponds to a homogeneous chain with stiffness coefficient dependent on α while $\varepsilon = 1$ corresponds to a homogeneous chain with local and nonlocal interactions. An initial velocity of 5.63×10^{-4} is prescribed to the first (heavy) sphere. As the wave propagates, the force amplitudes are monitored at two locations: (i) between the 100^{th} and 102^{th} spheres and (ii) between the 500^{th} and 502^{th} spheres. Figure 5.4 shows the variation of the two force amplitudes as a function of ε. The inset of Fig. 5.4 is a magnified version of the data near $\varepsilon = 0$. The figure demonstrates that

there are discrete values of ε for which the force amplitudes at the two locations are equal. Eight such cases are indicated by circular markers in Fig. 5.4. In these special cases, the leading wave is propagating without loss of force amplitude over a long distance, a key characteristic of a solitary wave. The condition of the existence of a solitary wave is referred as *antiresonance*, which will be discussed later.

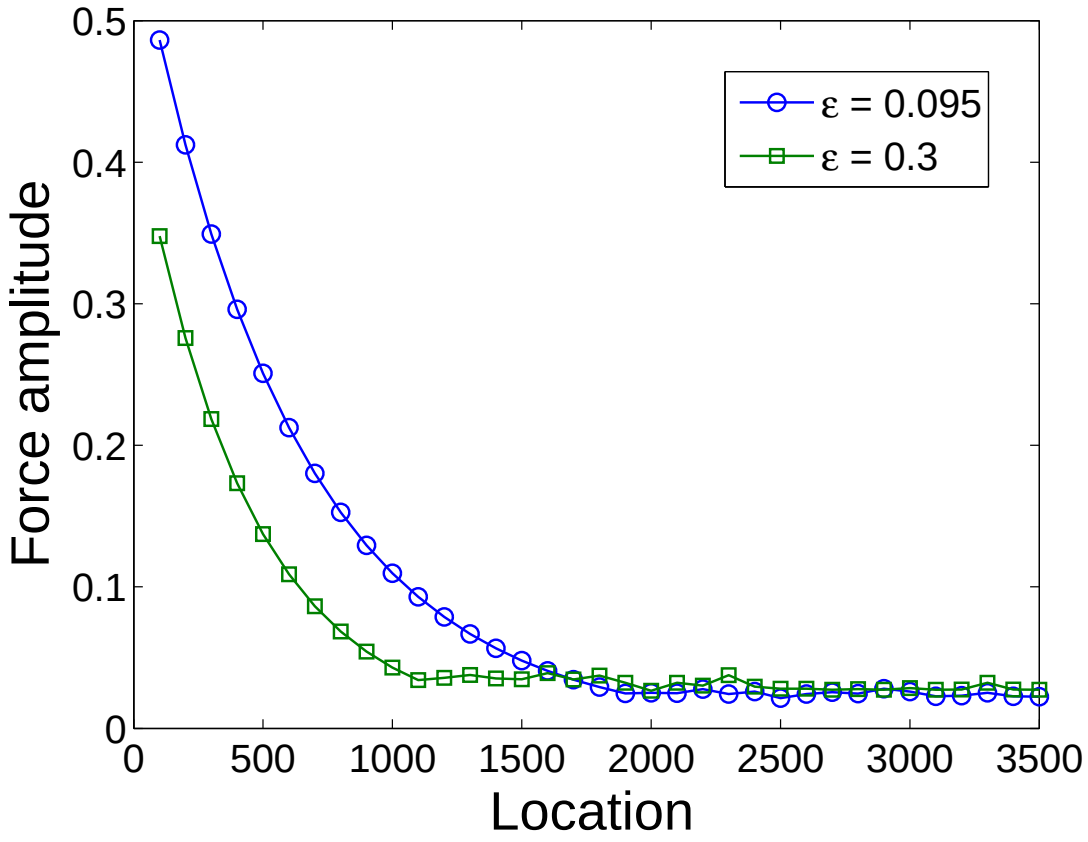

Figure 5.5: Force amplitudes as a function of contact location for $\varepsilon = 0.095$ and $\varepsilon = 0.3$.

As also observed in Fig. 5.4, the force amplitude of the leading wave decays if ε is different from the solitary wave cases. Furthermore, there is a local minimum in the force amplitude variation at location 500 between any two antiresonance cases. Five such cases are indicated by square markers. The presence of oscillations in the tail, as was demonstrated earlier in Fig. 5.2, is the cause of the decay of the force amplitude

of the leading wave. Thus, apart from the few cases of impedance mismatch at the contacts that give rise to solitary waves, the heavy and light spheres are not fully successful in transferring the incoming energy to the next neighboring spheres. As we move away from the solitary wave ε values, the oscillations in the tail gradually increase upto the local minimum, where the oscillation amplitude is maximum locally. Thus, there is another discrete set of ε values corresponding to each value for antiresonance from which (locally) maximum decay can be extracted. One may be interested in either of the two discrete sets depending upon the motivation for application.

Figure 5.5 shows the force amplitude between two neighboring heavy spheres at different locations in a chain of 3551 spheres for $\varepsilon = 0.095$ and $\varepsilon = 0.3$. As apparent there, the force amplitudes initially decrease with distance, as also observed in Fig. 5.4, but nearly plateau after certain locations. The transition here is found to be similar to the transition from exponential to power-law regime in a chain of random spheres (Fig. 2.2), i.e., the leading pulse force amplitude decaying below that of the backscatter.

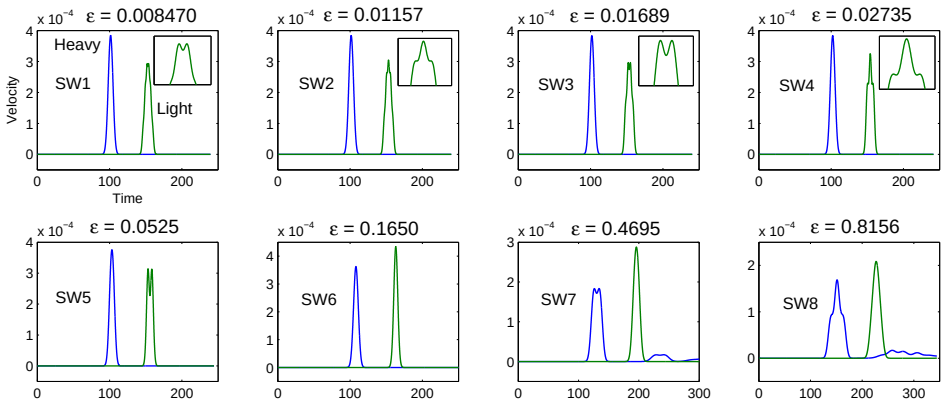

Figure 5.6: The velocity profiles for the heavy and light spheres for the eight cases of solitary waves (SW) of Fig. 5.4 (all with $\alpha = 0.6436$). The inset in each case magnifies the top portion of the light sphere's profile. *SW*6 corresponds to a case where both profiles are similar to those found in a homogeneous chain.

Figure 5.6 illustrates the eight solitary wave cases that were indicated by circular markers in Fig. 5.4. Each subfigure in Fig. 5.6 shows the velocity histories of a heavy and a light sphere in a long nonlocal dimer chain. The corresponding ε value is marked on top of each subfigure, while $\alpha = 0.6436$ is fixed for all cases. As observed there, the solitary wave profiles vary depending on the value of ε. For the cases $SW1-5$, the velocity profiles for the heavy sphere are similar to that of the homogeneous chain, while those of the light sphere are different with each case indicating multiple peaks and/or expansions and contractions in certain areas. However, for the cases $SW7$ and $SW8$, the light spheres exhibit a behavior similar to that of a homogeneous chain while the heavy spheres' profiles are different, similar to those of light spheres in $SW1-5$.

In Fig. 5.6, the velocity profiles of the heavy and light spheres corresponding to $\varepsilon = 0.165$ ($SW6$) are unique because both the spheres' responses are similar to that of a homogeneous chain. Henceforth, we refer to the case $SW6$ as a single peak solitary wave (SPSW). In contrast, a case similar to the SPSW case was not found in the local dimer chain [39]. The present finding indeed constitutes a special case as the system is inhomogeneous. As we shall discuss later, SPSW cases exist over a wide range of ε and α values. The width of the SPSW depends on the values of ε and α. In some cases of the solitary waves, there could also be smaller amplitude waves in the tail of the solitary waves. For example, $SW7-8$ show that the trailing waves are due to the transient effect and the solitary wave travels without attenuation after detachment from the tail.

One can compare the SPSW case with the homogeneous chain solitary wave by extracting the kinetic and potential energy content of the solitary waves and comparing with the virial theorem [5]. Figure 5.7 shows the history of the total kinetic and potential energies for the case of SPSW, i.e., $\varepsilon = 0.165$ and $\alpha = 0.6436$. The total kinetic (potential) energy is defined as the sum of the kinetic (potential)

energies of the spheres undergoing compression in the primary pulse. The dashed line corresponds to the sum of the total kinetic and potential energies at every time step. As observed in Fig. 5.7, the total kinetic and potential energies oscillate around their mean values, similar to that of a homogeneous chain discussed in Chapter 2. The mean values for the kinetic and potential energies are found to be approximately 0.555 and 0.444, respectively, and agree very well with the corresponding values (5/9 and 4/9) predicted by the virial theorem [5]. Thus the SPSW is indeed similar to the solitary wave in a homogeneous chain of spheres, confirming the unique case.

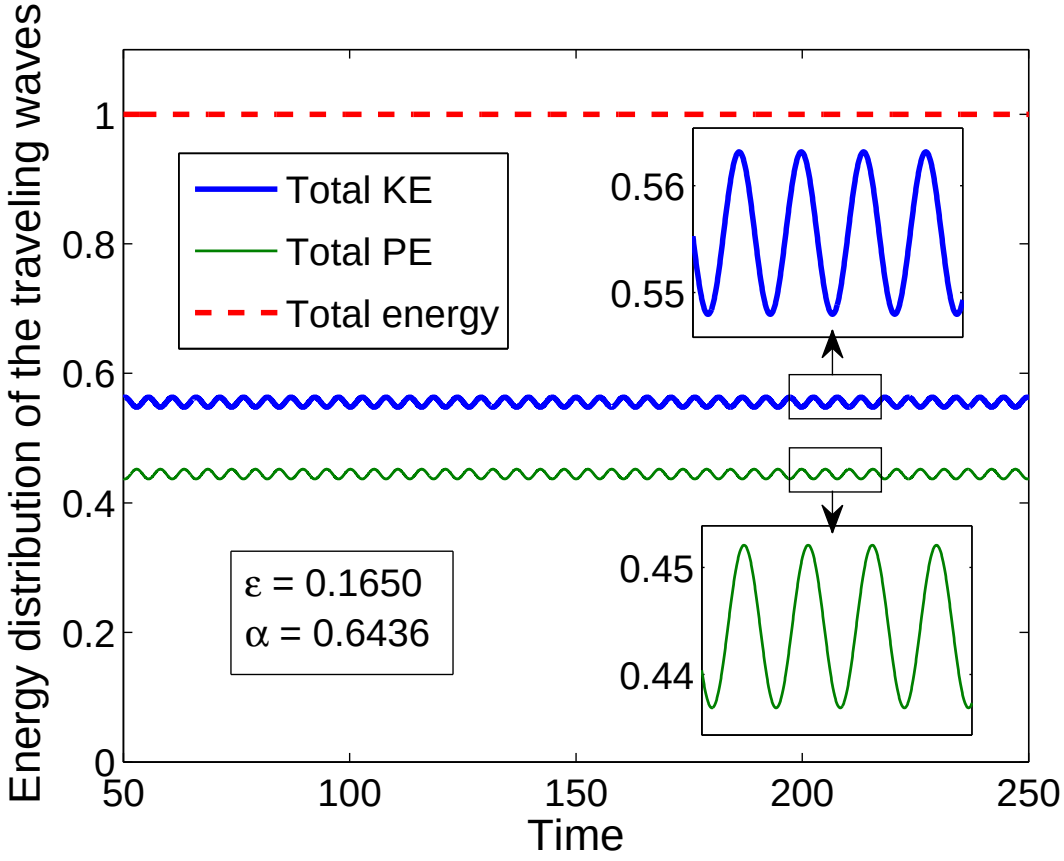

Figure 5.7: History of the energy distribution of the leading wave between total kinetic and potential energies normalized by the input kinetic energy for $\varepsilon = 0.165$ and $\alpha = 0.6436$ (SPSW). The dashed line corresponds to the sum of total kinetic and potential energies, confirming energy conservation. The insets show the magnified version of the variations about the mean values.

Figure 5.8 presents the solitary wave map defined on the (ε, α) space, i.e., for a

wide range of material properties. The stiffness ratio α is chosen in intervals of 0.1 in the range 0.1 to 1.28, which is lower than the maximum value $\alpha_{max} \approx 1.287$ (for $E_1/E_2 \ll 1$). For each α, wave propagation in a chain of 520 spheres is simulated with ε ranging from 0.001 to 1 in intervals of 0.001. Then the solitary wave cases are determined at locations where there is local minimum in force amplitude loss between sphere number 100 and 500. The case $SW6$ corresponds to SPSW, as noted in Fig. 5.6. As evident in Fig. 5.8(a), the eight solitary wave cases discussed earlier (and labeled $SW1-8$) exist for the range of α studied. Figure 5.8(b) is a magnified version showing the solitary wave cases $SW1-5$ more clearly as $\varepsilon \to 0$. We point out that the region between the curves give rise to attenuation of the leading wave, as was observed in Fig. 5.4. Thus, the solitary wave map indicates that there is lot of flexibility in choosing material combinations for the heavy and light spheres either to have zero or finite attenuation. Figure 5.8(a) also shows ε and α values for real material properties to illustrate combinations resulting in either perfect (or near) solitary wave or a amplitude-decaying response. The numbers labeled next to the circular markers indicate the material combinations and should be read according to Table 5.1. The heavy sphere is made of material corresponding to the first digit while the light sphere's material is indicated by the second digit of each of the two-digit labels.

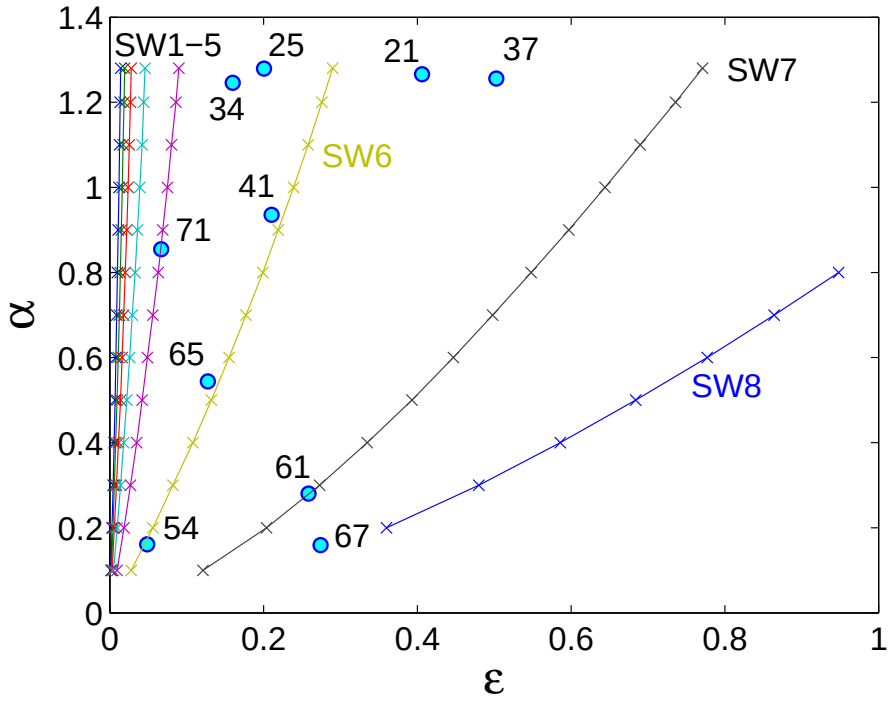

(a)

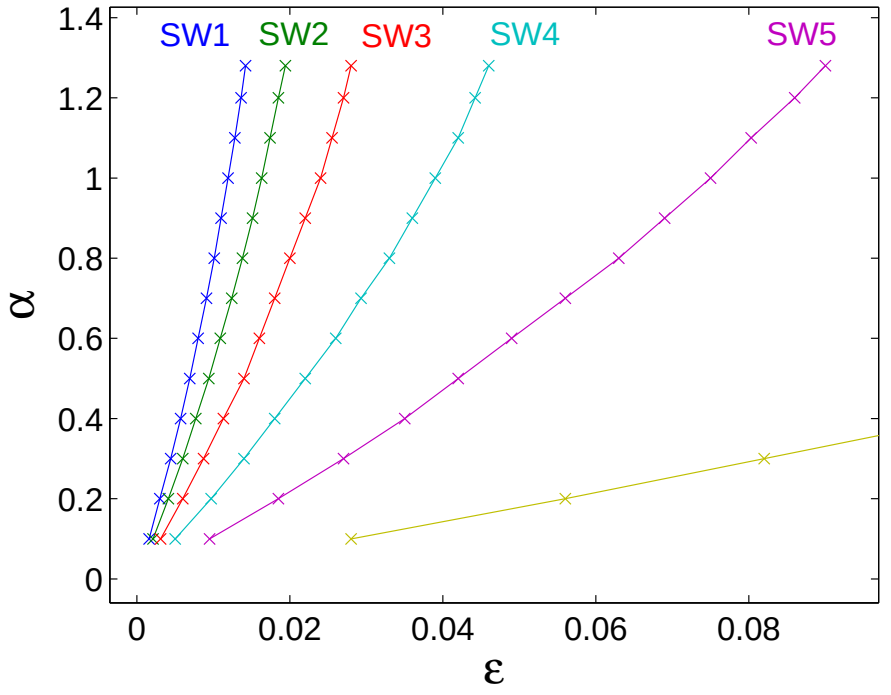

(b)

Figure 5.8: (a) Solitary wave map showing the combinations of ε and α that allow solitary wave propagation in the bidisperse system. The eight solitary wave cases of Fig. 5.6 are extracted for every α. (b) A magnified version of the map showing the data for smaller values of ε.

Table 5.1: Materials corresponding to the combinations used in Fig. 5.8(a).

Number	Material
1	Stainless steel
2	Delrin
3	Polycarbonate
4	Aluminum
5	Alumina
6	PTFE
7	Brass

5.3 Analytical investigation

5.3.1 Quasi-continuum approximation

In this section, a continuum approximation of the nonlocal dimer chain based on a long-wavelength approximation (LWA) is considered. The continuum approximation employed in this study follows the work by Pnevematikos et al. [64], who applied the method to nonlinear diatomic chains (see also [23]).

Consider the nondimensional equations of motion (5.4) of the heavy and light spheres governed by the parameters ε and α. For clarity, let us rewrite the above equations by denoting the displacement of the ith heavy particle by u_i and that of the light particle by v_i as

$$\ddot{u}_i = \alpha\left[(v_{i-1}-u_i)^{3/2}-(u_i-v_i)^{3/2}\right]+ \\ +\left[(u_{i-1}-u_i)^{3/2}-(u_i-u_{i+1})^{3/2}\right] \tag{5.6a}$$

$$\varepsilon\ddot{v}_i = \alpha\left[(u_i-v_i)^{3/2}-(v_i-u_{i+1})^{3/2}\right]. \tag{5.6b}$$

Defining $a = R_1 + R_2$ as the small parameter in the LWA and replacing u_i (v_i) with the continuous variable $u(x)$ ($v(x)$), displacements of the neighboring spheres are

defined as [5]

$$u_{i\pm1} = exp\left(\pm 2a\frac{\partial}{\partial x}\right)u_i \tag{5.7}$$
$$= u \pm 2au_x + 2a^2u_{xx} \pm \frac{4}{3}a^3u_{xxx} + \frac{2}{3}a^4u_{xxxx} + \cdots,$$

with the light sphere's displacement (v_i) similarly obtained. Substituting Eq. (5.7) in Eqs. (5.6) results in two coupled partial differential equations (PDEs). To solve these PDEs, the two displacements u_i and v_i are decoupled by incorporating the following condition [64]:

$$v = \sigma\left(u + b_1au_x + b_2a^2u_{xx} + b_3a^3u_{xxx} + b_4a^4u_{xxxx} + \cdots\right), \tag{5.8}$$

where σ and b_i are the unknown coefficients. Due to the ansatz Eq. (5.8), the two PDEs of Eqs. (5.6) are now only a function of heavy particle's displacement u. Since there is only one dependent variable, the parameters σ and b_i are determined by forcing the two PDEs to be equivalent. Similar to the cases discussed in [64] and [23], there are two possible values for σ, one corresponding to in-phase motion or acoustic mode ($\sigma = 1$) and the other for out-of-phase motion or optical mode ($\sigma = -\frac{1}{\varepsilon}$). Here, we report results for the acoustic mode case ($\sigma = 1$), given that the initial impulse condition for the present study leads to in-phase motion [23].

The parameters b_i are then obtained by equating successive orders of the small parameter a to zero. One obtains the following relations for the parameters b_1, b_2

and b_3:

$$
\begin{aligned}
b_1 &= 1, \\
b_2 &= \frac{\alpha - 2\sqrt{2}\varepsilon}{\alpha(1+\varepsilon)}, \\
b_3 &= \frac{2\alpha - 6\sqrt{2}\varepsilon - \alpha\varepsilon}{3\alpha(1+\varepsilon)}.
\end{aligned}
\tag{5.9}
$$

Determining the value of b_4 is not, however, as straightforward. After the two PDEs of Eqs. (5.6) are equated, we find that there are several derivative terms at the order $a^{9/2}$, where b_4 needs to be obtained, while the earlier b_i values had just one term at the corresponding orders of a. The presence of "residual" derivative terms is typical of problems with second-neighbor interactions [64], which is indeed the case in our study. The concerned order $a^{9/2}$ expression is

$$
\begin{aligned}
& a^{9/2}\Big[\varepsilon\Big(2\alpha^3(-1+\varepsilon) + 24\alpha\varepsilon + 8\sqrt{2}\varepsilon^2 - \sqrt{2}\alpha^2(4 + (-10+\varepsilon) \\
& \varepsilon)\Big)u_{xx}^3 + 12\alpha\varepsilon\Big(-\alpha^2(-1+\varepsilon) + 4(-3+\varepsilon)\varepsilon + \sqrt{2}\alpha(2 \\
& + (-5+\varepsilon)\varepsilon)\Big)u_x u_{xx} u_{xxx} + 4\alpha\Big(-24\varepsilon^2 + 2\sqrt{2}\alpha\varepsilon(4 \\
& + (-1+\varepsilon)\varepsilon) + \alpha^2\Big(-1 + \varepsilon - \varepsilon^2 + 3(1+\varepsilon)^3 b_4\Big)\Big)u_x^2 u_{4x}\Big] \\
& = a^{9/2}\Big[P(\varepsilon,\alpha)u_{xx}^3 + Q(\varepsilon,\alpha)u_x u_{xx} u_{xxx} + S(b_4,\varepsilon,\alpha)u_x^2 u_{4x}\Big].
\end{aligned}
\tag{5.10}
$$

As apparent in Eq. (5.10), P, Q and S have to be *simultaneously* zero for the two PDEs to be identical. We can set $S = 0$ to obtain b_4 as

$$
\begin{aligned}
b_4 = & \frac{1}{3\alpha^2(1+\varepsilon)^3}\Big(\alpha^2 - 8\sqrt{2}\alpha\varepsilon - \alpha^2\varepsilon + 24\varepsilon^2 + 2\sqrt{2}\alpha\varepsilon^2 \\
& + \alpha^2\varepsilon^2 - 2\sqrt{2}\alpha\varepsilon^3\Big),
\end{aligned}
\tag{5.11}
$$

but P and Q cannot be equated to zero simultaneously. A similar situation occurs in the case of original local dimer chain [23], where $P = Q$, and $P = Q = 0$ is valid only

when $\varepsilon = 1$. In that study, the two functions were neglected, possibly due to the functions being coefficients of higher-order terms. Thus, a single PDE was obtained with the assumption that $P = Q = 0$ and then a traveling wave solution similar to that of a homogeneous chain was obtained. In the present study, however, we ask the following question: Is it possible to predict the values (ε, α) for the case of SPSWs ($SW6$ in Fig. 5.8(a))? Since $P = Q = 0$ will yield solitary wave solutions, we now proceed and compare the solutions of $P = 0$ and $Q = 0$ with that of the discrete data points for SPSWs. The required solutions of $P = 0$ and $Q = 0$ are given by

$$\begin{aligned} \alpha &= \frac{\sqrt{2}\varepsilon\left(6 - \varepsilon + \sqrt{52 - 28\varepsilon + \varepsilon^2}\right)}{4\,(1-\varepsilon)}, \\ \alpha &= \frac{\sqrt{2}\varepsilon\,(3-\varepsilon)}{1-\varepsilon}, \end{aligned} \tag{5.12}$$

respectively. Figure 5.9 shows the $\alpha - \varepsilon$ variation as given by Eqs. (5.12) and data points of SPSWs ($SW6$) from the map in Fig. 5.8. As evident in Fig. 5.9, the solution for $Q = 0$ predicts the numerical data well, while the solution of $P = 0$ is not very accurate. At this end, we resort to the technique of introducing an additional term in the ansatz given in Eq. (5.8), similar to Eq. (3.2) in [64]. This additional term is guessed based on the residual terms' derivatives. In our case, $P(\varepsilon, \alpha)u_{xx}^3$ is chosen as the residual term that needs to be eliminated, while we enforce $Q = 0$ to seek solitary wave solutions. To eliminate the residual term, the additional term in Eq. (5.8) is taken as $b_5 a^4(-u_x)^{-2}u_{xx}^3$, where b_5 is given by

$$\begin{aligned} b_5 =& \frac{\varepsilon}{12\alpha^3(1+\varepsilon)^3}\Big(4\sqrt{2}\alpha^2 + 2\alpha^3 - 24\alpha\varepsilon - 10\sqrt{2}\alpha^2\varepsilon - 2\alpha^3\varepsilon \\ & - 8\sqrt{2}\varepsilon^2 + \sqrt{2}\alpha^2\varepsilon^2\Big). \end{aligned} \tag{5.13}$$

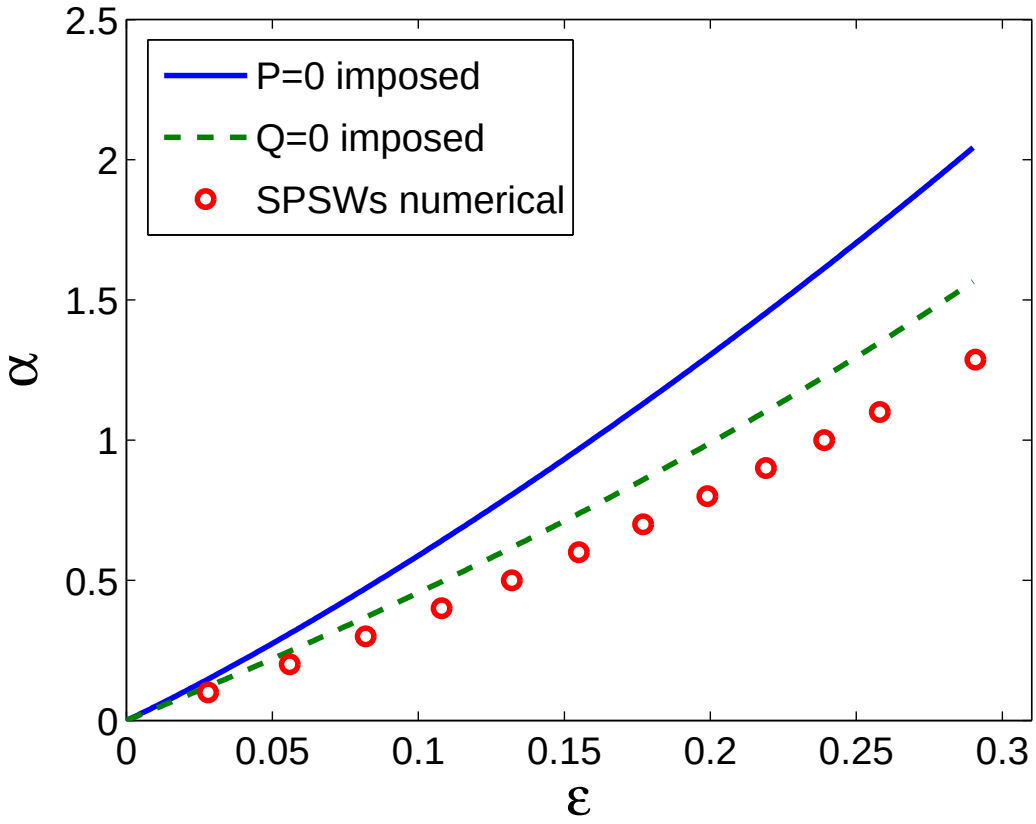

Figure 5.9: Variation of α with ε comparing the numerical data for $SW6$ from Fig. 5.8 with Eqs. (5.12). The first and the second Eqs. (5.12) correspond to $P = 0$ (solid line) and $Q = 0$ (dashed line), respectively.

We now end up with a single PDE in heavy particle's displacement u given by

$$\begin{aligned} u_{tt} =& \frac{3\sqrt{2}a^{5/2}(-2+\varepsilon)\sqrt{-u_x}u_{xx}}{-1+\varepsilon} \\ &- \frac{a^{9/2}(-2+\varepsilon)(-u_x)^{3/2}}{4\sqrt{2}(-3+\varepsilon)(-1+\varepsilon)(1+\varepsilon)}\Big(\Big(-3-2\varepsilon+4\varepsilon^2\Big)u_{xx}^3 \\ &+ 4\Big(6+\varepsilon-5\varepsilon^2\Big)u_x u_{xx} u_{xxx} - 8\Big(-3+\varepsilon+\varepsilon^2\Big)u_x^2 u_{4x}\Big), \end{aligned} \tag{5.14}$$

with the same order derivative terms as in the homogeneous chain's PDE [5] but with different coefficients. Rescaling the time variable (t) as

$$\tau = t\sqrt{3\sqrt{2}a^{5/2}(2-\varepsilon)/(1-\varepsilon)}. \tag{5.15}$$

We can now obtain exact periodic solutions for traveling waves with the transformation $\xi = x - V\tau$, where V is the wave speed. The new definition transforms the PDE of Eq. (5.14) into an ODE in the first derivative of u (u_ξ) (see [23] for intermediate steps). We find the final solution as

$$u_\xi = B(\varepsilon) cos^4\left(b(\varepsilon)\xi\right), \tag{5.16}$$

where the amplitude of the wave $B(\varepsilon)$ and the characteristic spatial wavelength $w(\varepsilon)$ as a function of $b(\varepsilon)$ are given by

$$B(\varepsilon) = \frac{9V^4(15 - 2\varepsilon - 8\varepsilon^2)^2}{4(12 - \varepsilon - 7\varepsilon^2)^2}, \tag{5.17}$$

$$w(\varepsilon) = \frac{\pi}{b(\varepsilon)} = \sqrt{2}a\pi\sqrt{\frac{15 - 2\varepsilon - 8\varepsilon^2}{3 + 2\varepsilon - \varepsilon^2}}, \tag{5.18}$$

respectively.

Figure 5.10(a) shows the variation of the normalized spatial wavelength (w/a) with ε, as given by Eq. (5.18). We note that $\varepsilon = 1$ exactly recovers the 1D homogeneous chain solution of Nesterenko [5], which is about five particle diameters. Figure 5.10(b) shows the velocity profiles from simulations for $\varepsilon = 0.165$ and $\varepsilon = 0.7$ (markers in Fig. 5.10(a)). Thus the spatial wavelengths from simulations for $\varepsilon = 0.165$ and $\varepsilon = 0.7$ are found to be about 10 and 8 particle diameters, respectively, showing a very good agreement with the analytical prediction of Fig. 5.10(a).

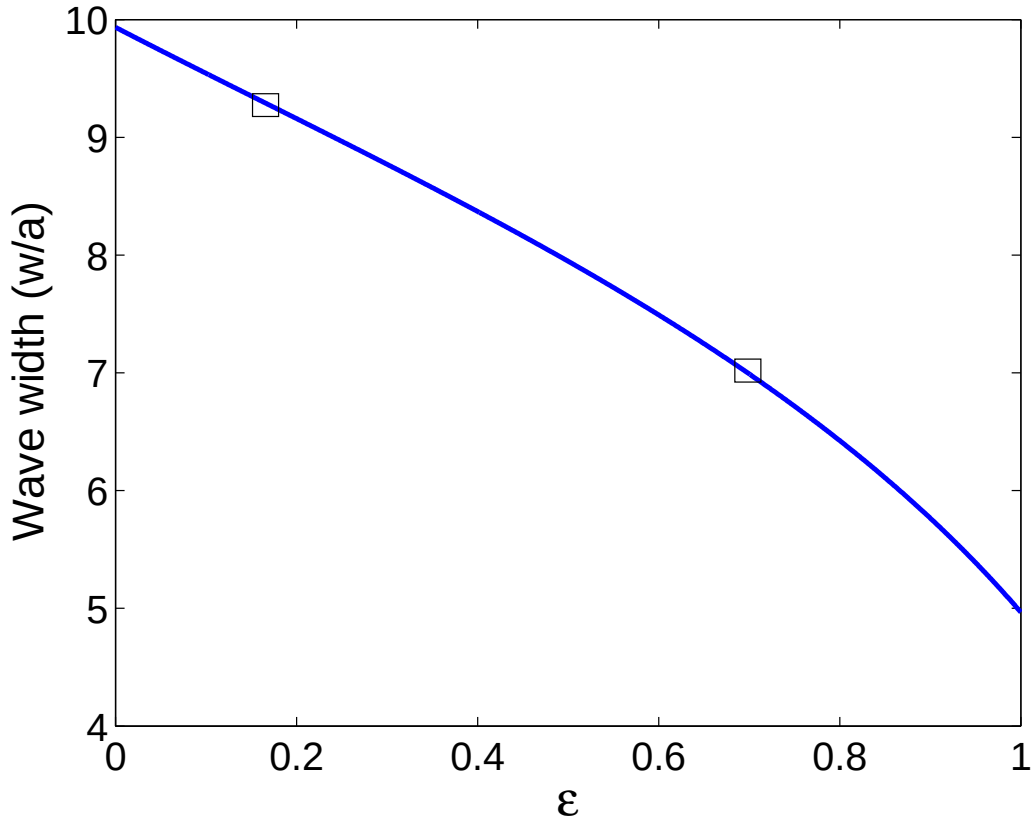

(a)

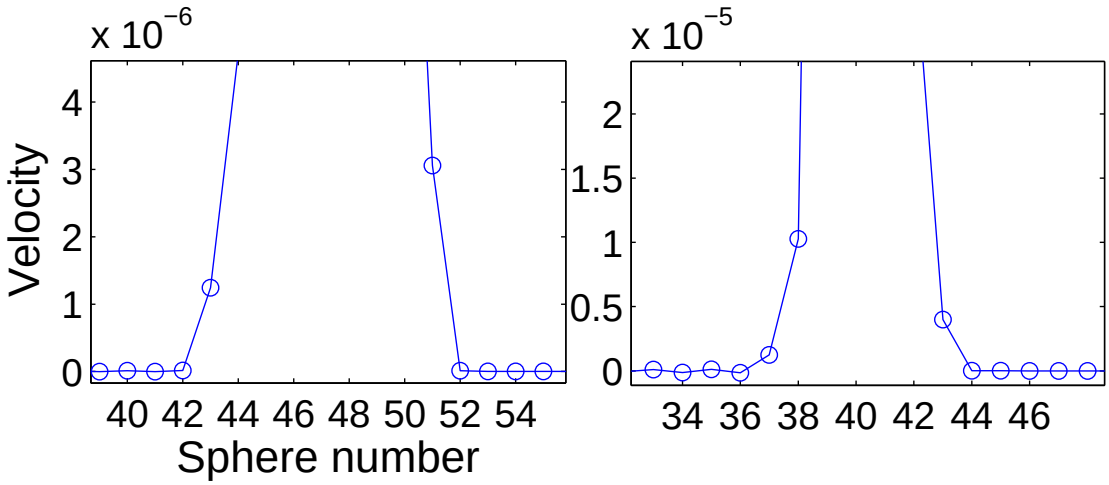

(b)

Figure 5.10: (a) Normalized spatial wavelength (w/a) as a function of ε from the analytical solution (5.18). (b) Velocity profiles (illustrating spatial wavelength) for the two cases of ε marked by symbols in Fig. 5.10(a) ($\varepsilon = 0.165$ and $\varepsilon = 0.7$), showing a good comparison with the analytical solution.

By employing the solution for strain variable (Eq. (5.16)), one can also obtain the wave speed as a function of its force amplitude [2]. Figure 5.11 compares the wave speed-force amplitude dependence for $\varepsilon = 0.165$ with that of the simulations. A reasonable comparison (with an error of about 9.5%) is obtained with the error arising from the quasi-continuum approximation and the fact that the force amplitude varies as $F_m \propto V^6$, i.e., the error is more pronounced since the phase velocity is raised to the power six.

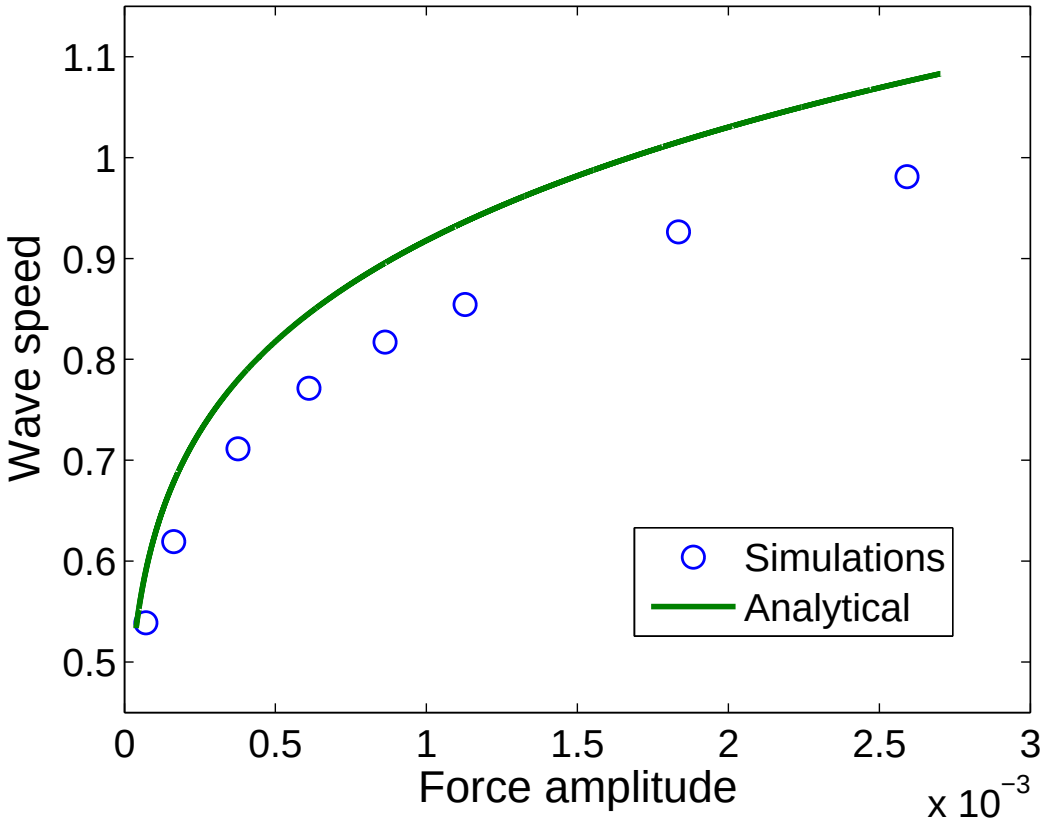

Figure 5.11: Nondimensional wave speed as a function of the force amplitude comparing the simulation results with the analytical solution from (5.16).

5.3.2 Asymptotic analysis

In the previous section, the set of values of ε and α for the case of SPSWs was predicted by using a quasi-continuum approach. In this section, the objective is to

predict the solitary waves over a wider range of ε and α with the aid of an asymptotic method [65].

Consider the normalized equations of motion in Eq. (5.4), where ε is considered small in the following analysis, i.e., $0 < \varepsilon \ll 1$, while there is no restriction on α. As discussed in [65, 39], the main principle behind the asymptotic method adopted hereafter is the separation of time scale in the limit of small ε. Thus, for the primary (solitary) wave propagation, we can write the heavy and light spheres' displacements (u_i and u_{i+1}) with the following asymptotic expansions:

$$\begin{aligned} u_i &= u_{i0}(t_0) + \varepsilon^{\lambda} u_{i1}(t_1) + \cdots, \\ u_{i+1} &= u_{(i+1)0}(t_0) + \varepsilon^{\gamma} u_{(i+1)1}(t_1) + \cdots, \end{aligned} \tag{5.19}$$

where the separated time scales are $t_0 = \tau$ and $t_1 = \varepsilon^{\beta} t_0$ and λ, γ and β are the unknowns to be determined. We now substitute Eq. (5.19) in Eq. (5.4) along with the two time scales, and then expand the relevant terms in power series as $\varepsilon \to 0$ to obtain, for the heavy sphere,

$$\begin{aligned} \ddot{u}_{i0} + \varepsilon^{\lambda+2\beta} u''_{i1} =& \alpha \left[\left(u_{(i-1)0} - u_{i0} \right)^{3/2} - \left(u_{i0} - u_{(i+1)0} \right)^{3/2} \right] \\ &+ \left(u_{(i-2)0} - u_{i0} \right)^{3/2} - \left(u_{i0} - u_{(i+2)0} \right)^{3/2} \\ &+ (3/2)\alpha \left(u_{(i-1)0} - u_{i0} \right)^{1/2} \left(\varepsilon^{\gamma} u_{(i-1)1} - \varepsilon^{\lambda} u_{i1} \right) \\ &- (3/2)\alpha \left(u_{i0} - u_{(i+1)0} \right)^{1/2} \left(\varepsilon^{\lambda} u_{i1} - \varepsilon^{\gamma} u_{(i+1)1} \right) \\ &+ (3/2)\varepsilon^{\lambda} \left(u_{(i-2)0} - u_{i0} \right)^{1/2} \left(u_{(i-2)1} - u_{i1} \right) \\ &- (3/2)\varepsilon^{\lambda} \left(u_{i0} - u_{(i+2)0} \right)^{1/2} \left(u_{i1} - u_{(i+2)1} \right) \\ &+ \mathrm{O}\left(\left\| \varepsilon^{\lambda} u_{i1} - \varepsilon^{\gamma} u_{(i+1)1} \right\|^2 \right), \end{aligned} \tag{5.20}$$

while the light sphere's equation expands to

$$\begin{aligned}
&\varepsilon\left(\ddot{u}_{(i+1)0}+\varepsilon^{\gamma+2\beta}u''_{(i+1)1}\right)=\\
&\alpha\Big[\left(u_{i0}-u_{(i+1)0}\right)^{3/2}-\left(u_{(i+1)0}-u_{(i+2)0}\right)^{3/2}\\
&+(3/2)\left(u_{i0}-u_{(i+1)0}\right)^{1/2}\left(\varepsilon^{\lambda}u_{i1}-\varepsilon^{\gamma}u_{(i+1)1}\right)\\
&-(3/2)\left(u_{(i+1)0}-u_{(i+2)0}\right)^{1/2}\left(\varepsilon^{\gamma}u_{(i+1)1}-\varepsilon^{\lambda}u_{(i+2)1}\right)\\
&+\mathrm{O}\left(\left\|\varepsilon^{\lambda}u_{i1}-\varepsilon^{\gamma}u_{(i+1)1}\right\|^2\right)\Big].
\end{aligned}\tag{5.21}$$

In Eqs. (5.20) and (5.21), overdots and primes correspond to differentiation with respect to the two times scales, t_0 and t_1, respectively. One can now compare different terms at each order to obtain the unknown parameters λ, γ and β. From the left hand side of Eq. (5.20), we can choose $\lambda+2\beta=1$ for the first-order approximation, which allows us to choose either $\lambda=1$ or $\gamma=1$ or $\lambda=\gamma=1$ from the right hand side of the equation. Since β cannot be zero ($\beta=0$ implies no separation of time scales), we choose $\gamma=1$. Equation (5.21) now implies $\gamma+2\beta=0$, which yields $\beta=-1/2$ and $\lambda=2$. Thus, $t_1=\varepsilon^{-1/2}t_0$ and Eqs. (5.20) and (5.21) have errors of order $\left\|\varepsilon^2u_{i1}-\varepsilon u_{(i+1)1}\right\|^2$.

We now proceed to obtain the approximations at various orders of Eqs. (5.20) and (5.21) essentially yielding the slow (zeroth-order approximation) and fast dynamics (first-order approximation) components of the above equations. The zeroth-order approximations for heavy and light spheres are obtained as

$$\begin{aligned}
\ddot{u}_{i0}=&\alpha\left[\left(u_{(i-1)0}-u_{i0}\right)^{3/2}-\left(u_{i0}-u_{(i+1)0}\right)^{3/2}\right]\\
&+\left(u_{(i-2)0}-u_{i0}\right)^{3/2}-\left(u_{i0}-u_{(i+2)0}\right)^{3/2},\\
u_{(i+1)0}=&\frac{u_{i0}+u_{(i+2)0}}{2},
\end{aligned}\tag{5.22}$$

respectively. Thus the slow dynamics of the light sphere (indicated by its depen-

dence on t_0 alone) is simply the average of the slow dynamics of its neighboring heavy spheres, similar to the local dimer chain [39]. The slow dynamics of a heavy sphere is more complicated due to the presence of nonlocal interactions. However, one can simplify the first Eq. (5.22) further by substituting the response of the light spheres from second Eq. (5.22):

$$\begin{aligned} \ddot{u}_{i0} &= \left(1 + \frac{\alpha}{2^{3/2}}\right)\left[\left(u_{(i-2)0} - u_{i0}\right)^{3/2} - \left(u_{i0} - u_{(i+2)0}\right)^{3/2}\right], \\ u_{(i+1)0} &= \frac{u_{i0} + u_{(i+2)0}}{2}. \end{aligned} \tag{5.23}$$

The slow dynamics of the heavy sphere (first Eq. (5.23)) now solely depends on the nonlocal interactions with its nearest heavy spheres, which is equivalent to the response of a homogeneous chain of heavy spheres. We observe that the first Eq. (5.23) has an explicit dependence on α while it is a constant in the local dimer chain [39].

The dynamic response of a homogeneous chain of spheres is basically a solitary wave [5]. Thus, the zeroth-order solution for both heavy and light spheres does not lead to formation of any "tail". In the open literature, there are a number of analytical approximations [5, 3] which are applicable to the first Eq. (5.23). We choose the solution by Sen et al. [6], which has been shown to be more accurate than the solution by Nesterenko [5]. The displacement of the solitary wave is described in terms of the hyperbolic tangent function as [3]

$$\begin{aligned} S(z) =& A + (A/2)\left[\tanh\left\{\left(C_1(z/T) + C_3(z/T)^3 + C_5(z/T)^5\right)/2\right\} - 1\right], \\ C_1 =& 2.39536, \qquad C_3 = 0.268529, \qquad C_5 = 0.0061347, \end{aligned} \tag{5.24}$$

where A and T are the amplitude of the solitary wave and time taken by the solitary wave to reach maximum amplitude between two neighboring spheres, respectively. In order to obtain the displacements of the individual spheres in the system (5.23),

the following transformations are employed:

$$\begin{aligned} u_{i0}(t_0) =& S_i(kt_0), \qquad k = (1 + \alpha/2^{3/2})^{1/2}, \\ S_i(kt_0) =& S[k(t_0 - iT)]. \end{aligned} \tag{5.25}$$

By employing the above solution for the slow dynamics of the heavy spheres, the slow dynamics of the light spheres can be written as

$$u_{(i+1)0} = \frac{S_i(kt_0) + S_{i+2}(kt_0)}{2}. \tag{5.26}$$

Since the zeroth-order solution does not have any trailing waves for any ε and α, higher-order approximation is necessary to find the discrete set of values of ε and α for which the tail goes to zero, i.e., for the formation of solitary waves. We now proceed to the first-order approximation ($O(\varepsilon)$) in Eqs. (5.20) and (5.21) to obtain the following relations for the fast dynamics component of the heavy and light spheres:

$$\begin{aligned} u''_{i1} =& (3/2)\alpha(S_{i-1}(kt_0) - S_i(kt_0))^{1/2}\left(u_{(i-1)1}(t_1)\right) \\ &+ (3/2)\alpha(S_i(kt_0) - S_{i+1}(kt_0))^{1/2}\left(u_{(i+1)1}(t_1)\right), \\ u''_{(i+1)1}(t_1) + \Omega^2_{i+1}(t_0)u_{(i+1)1}(t_1) =& f_{i+1}(t_0). \end{aligned} \tag{5.27}$$

In second Eq. (5.27), Ω^2 is the natural frequency and f is the force excitation, which are functions of the zeroth-order (slow) responses of the spheres as given by

$$\begin{aligned} \Omega^2_{i+1}(t_0) =& 3\alpha\left(\frac{u_{i0}(t_0) - u_{(i+2)0}(t_0)}{2}\right)^{1/2}, \\ f_{i+1}(t_0) =& -\ddot{s}_{i+1}(kt_0). \end{aligned} \tag{5.28}$$

Furthermore, we observe that Eqs. (5.27) are linear oscillators, where the second Eq. (5.27) is solely a function of light sphere's displacement, i.e., it is uncoupled.

The uncoupled linear oscillator is then numerically integrated to find the cases for which solitary waves are formed. The second Eq. (5.27) is sufficient because a zero tail in the light sphere's fast response implies a zero tail in the heavy sphere's fast response.

We direct the reader to Ref. [39] for a detailed discussion on the relevant conditions for the formation of localized solitary waves with compact support. In essence, the necessary and sufficient conditions for the generation of these specific solitary waves respectively are

$$\begin{aligned} u_{(i+1)1}(t_1 = 0) &= 0, \\ \lim_{t_1 \to +\infty} u'_{(i+1)1}(t_1) &= 0, \end{aligned} \tag{5.29}$$

where the time axis is shifted such that the reference time $\tau = 0$. Then the differential equation to be solved to determine the values of ε (for a given α) that satisfy Eq. (5.29) is given by

$$u''_{(i+1)1}(t_0) + \frac{\Omega^2_{i+1}(t_0)}{\varepsilon} u_{(i+1)1}(t_0) = \frac{f_{i+1}(t_0)}{\varepsilon}. \tag{5.30}$$

Equation (5.30) is just another version of the second Eq. (5.27), with the fast time scale (t_1) written in terms of the slow time scale (t_0). Equation (5.30) is solved numerically by iterating over various values of $0 < \varepsilon \leq 1$. Figure 5.12 shows the variation of the displacement $u_{(i+1)1}$ at $t_0 = 0$ as a function of ε for $\alpha = 0.6436$. We note the oscillatory nature of the displacement leading to the existence of countable infinity of discrete values of ε that have $u_{(i+1)1}(0) = 0$, i.e., solitary waves. For ε values close to zero, we need a much finer spacing between any two values to obtain more accurate results. The circular markers correspond to the six solitary wave cases $SW1-6$ in Fig. 5.6 which were shown for the same $\alpha = 0.6436$. Thus, the asymptotic method fails to predict solitary waves beyond $SW6$. The primary reason for this

limited application is that the fast dynamics is no longer in the light sphere but is shifted to the heavy sphere, as shown in the velocity profiles for $SW7$ and $SW8$ in Fig. 5.6.

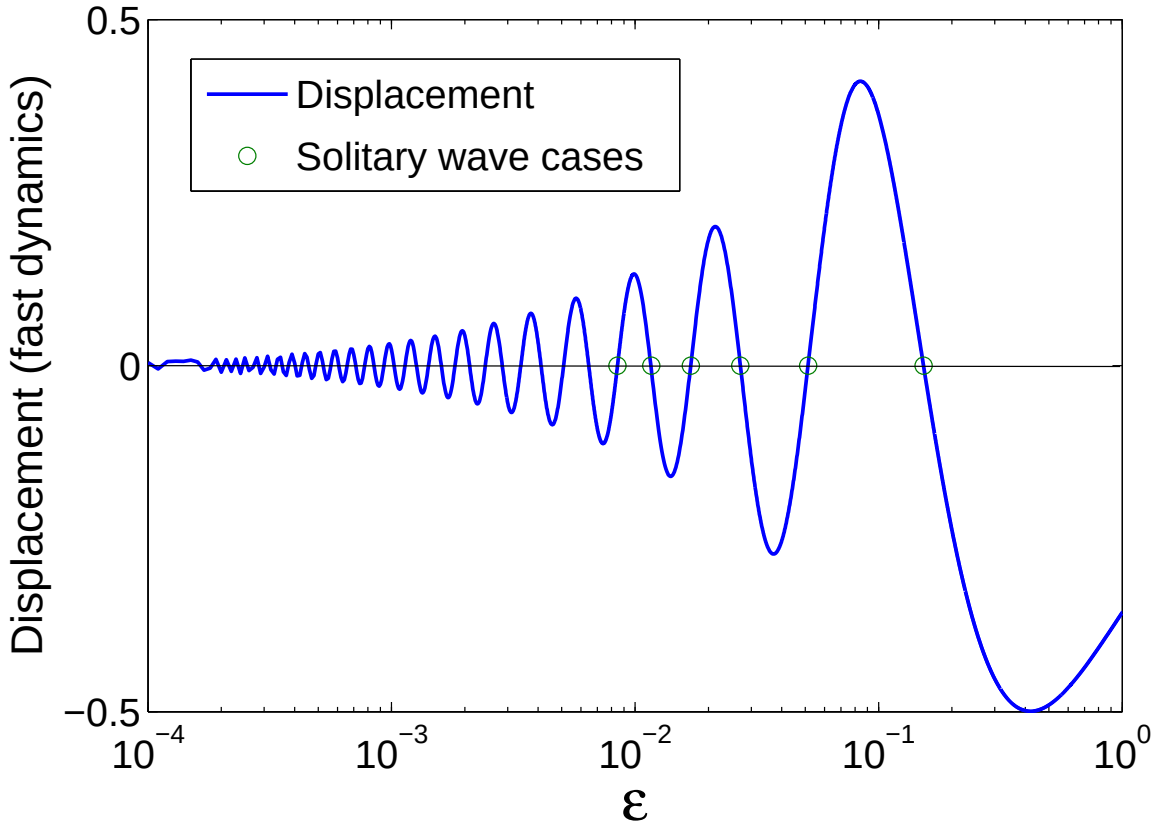

Figure 5.12: Fast dynamics displacement component of the light sphere at $t_0 = 0$ as a function of ε (on log scale). The solitary wave cases $SW1 - 6$ (Fig. 5.6) are marked with circles.

Figure 5.13 shows the history of fast dynamics component of the displacement ($u_{(i+1)1}$) and the total velocity ($\dot{u}_{i+1}$) of the light sphere for $\varepsilon = 0.01692$ and $\alpha = 0.6436$. As the displacement is anti-symmetric ($u_{(i+1)1}(0) = 0$) and the velocity is decaying to zero after a certain time, this case corresponds to the solitary wave $SW3$ in Fig. 5.6. We can also observe that the velocity profile is captured well by the asymptotic method. The number of peaks (or valleys) in the displacement profile indicates the number of "humps" in the traveling wave. Therefore, there are four humps for

*SW*3 case and increases (decreases) further by one hump as ε decreases (increases). The final case (*SW*6) will therefore have only one hump, after which the asymptotic analysis used in this section becomes inapplicable.

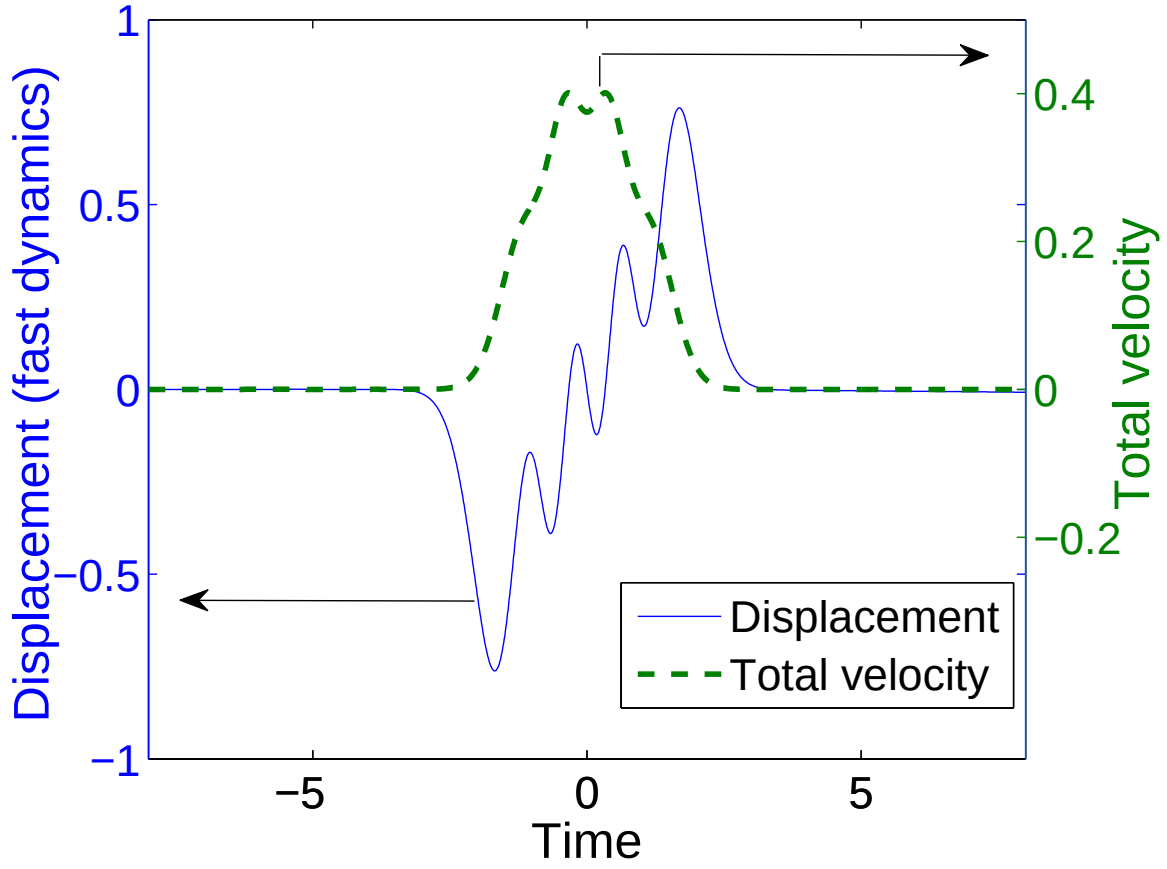

Figure 5.13: History of the fast dynamics displacement component and the total velocity of the light sphere for the solitary wave case *SW*3 (ε = 0.01692 and α = 0.6436).

Equation (5.30) is now solved over a wider range of α to obtain the corresponding discrete values of ε that give rise to solitary waves. Figure 5.14 shows the comparison between asymptotic ε predictions for certain values of α and the solitary wave map from the simulations (Fig. 5.8) for *SW*4 − 6. Thus we find that the asymptotic values are predicted well especially for smaller values of ε, as expected. As the ε value increases the asymptotic prediction begins to deviate, as apparent for the case *SW*6, which can be made more accurate by considering higher-order terms in the

asymptotic expansions (5.19). We again emphasize that the *SW*6 case is the final case predicted by the aforementioned asymptotic analysis.

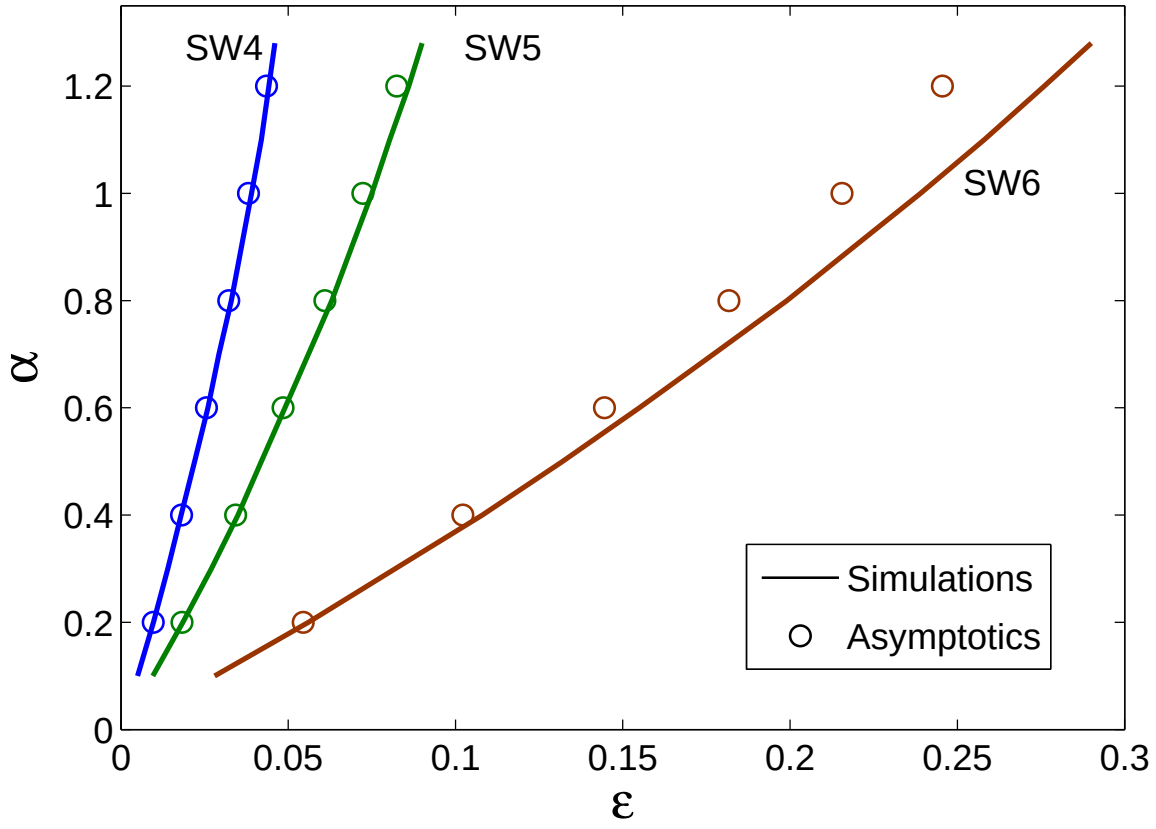

Figure 5.14: α-ε variation for the solitary wave cases $SW4-6$ comparing the asymptotic solution (circles) with the numerical simulation (solid lines) (Fig. 5.8). *SW*6 corresponds to the SPSW case.

5.4 Conclusions

A numerical investigation was undertaken to study plane wave propagation in a 2D square packing system of spherical particles with intruders at interstitial locations. The granular system was considered to be periodic in the lateral direction and semi-infinite in the direction of propagation. Nondimensionalizing the system of equations demonstrated two key parameters governing the dynamics of the granu-

lar system: the mass ratio ε and the stiffness ratio α. An equivalent 1D granular chain was proposed based on the periodicity of the closed-packed system and the planar impact loading. The equivalent granular chain, termed nonlocal dimer chain, differs from the original dimer chain due to the presence of additional nonlocal interactions between nearest larger spheres. The 1D equivalence was verified by comparing the numerical results of the 1D and 2D systems. Further investigation of the nonlocal dimer chain revealed the existence of a new family of solitary waves for discrete combinations of ε and α. The solitary waves were found to propagate with different profiles depending on the nondimensional parameters α and ε. Furthermore, an unique case of a solitary wave where the profile is similar to that of a homogeneous chain was reported in the present inhomogeneous system. A systematic procedure was performed to generate a solitary wave map of combinations of ε and α encompassing some of the solitary wave cases. Finally, a couple of analytical studies were conducted to predict the solitary wave cases, particularly the case similar to the homogeneous solitary wave. By employing a quasi-continuum approximation, the discrete system of partial differential equations was reduced to a single ordinary differential equation and a solitary wave solution was obtained. Wave width and wave speed-force amplitude dependence were compared with the analytical solution and showed a good agreement. In another approach, an asymptotic analysis was performed to predict the discrete values of material combinations for the existence of solitary waves in the limit of $\varepsilon \to 0$. The asymptotics also demonstrated a very good agreement with the solitary wave map generated from the simulations.

Chapter 6

Embedded granular systems

Due to the inherently nonlinear properties of the inter-particle contact, granular chains have unique wave propagation properties that are increasingly being considered for impact protection and wave tailoring applications. However, most of the work so far has focused on 'laboratory granular systems' in the absence of a container or matrix material. However, the granular chains need to be embedded in a matrix or contained if these systems are to be deployed in engineering applications. A computational analysis of this new class of granular chain-matrix material system is the topic of this chapter. We undertake a preliminary study to investigate the bending response of a linear elastic beam with granular chains embedded in an ordered manner. A key motivation comes from the unique flexibility of granular chains with regard to response of the spherical particles under compression or tension. This 'unusual' response can be visualized by considering the granular chains as nonlinear 'fibers' with zero stiffness under tension whereas they follow the Hertzian law under compression. Thus, depending on the presence or absence of the contact forces, spheres or the surrounding matrix may play a dominant role in the bending response. The no-tension condition thus yields a unique kind of bending behavior where some of the chains are under compression while some are in tension depending on their locations with respect to the neutral axis.

Our previous studies on the effect of randomness on wave propagation in granular systems have shown that the energy carried by the wavefront decays very quickly due to backscattering, and thus emphasis will be placed on avoiding randomness

in the embedded granular system. Some of the ways the spheres can be packed together is by filling matrix material in between the spheres or drilling holes in a matrix to accommodate granular networks. Experiments such as dynamic impact of square or hexagonal packing of spheres in a matrix, energy transfer between two or more chains in a matrix and numerically extracting a quasi-static force-displacement law at the sphere-matrix interface have demonstrated some challenges in manufacturing and testing the "infused" configuration, thus the focus of our studies will be on the "drilled" configuration.

The remainder of the chapter is organized as follows: Section 6.1 defines the problem and describes the numerical setup. In Sec. 6.2,we present the finite element formulation for the embedded granular system is presented. Section 6.3 explains the algorithm used in current study. Sections 6.4 and 6.5 verify the finite element program and perform convergence studies, respectively. Section 6.6 summarizes the results of dynamic studies of embedded granular systems. Precompression in the granular chains is also expected to play a role in the bending response because it directly affects the amplitude of vibration. In Sec. 6.6, we also perform studies to investigate the effect of precompression on the bending behavior particularly at resonance.

6.1 Problem description and numerical setup

Consider a beam made of a linear elastic homogeneous material and fixed at both ends. In the axial direction of the beam, i.e., parallel to the neutral axis, one or more homogeneous granular chains are inserted by drilling holes into the beam. The granular chains are assumed to extend from the left to right end of the beam. Figure 6.1 shows an example where one chain of spheres is inserted into a beam fixed at both ends. The beam is subjected to a point load at the center of the top edge.

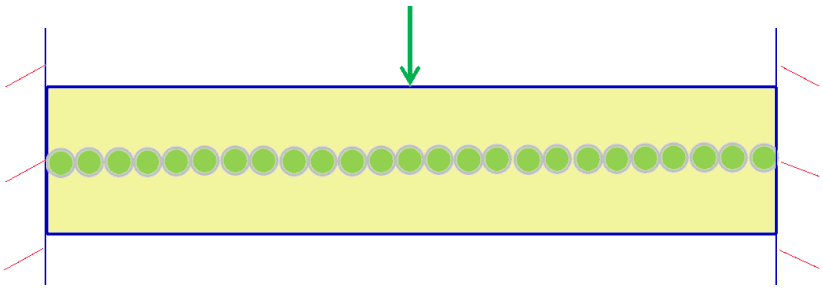

Figure 6.1: A granular chain embedded at the center of a linear elastic beam. The loading is applied at the center of the beam.

A finite element solver is written in MATLAB® to simulate the static and dynamic behavior of beams embedded with granular chains. The granular chains are approximated as continuum bar elements where a nonlinear force-displacement relationship is derived. Then we seek the tangent stiffness matrix which is employed in the Newton-Raphson technique. Newmark method is used for numerical time integration. In our studies, the material properties for the linear elastic beam and spheres are fixed corresponding to epoxy and steel, respectively. Epoxy (steel) properties are taken as: Young's modulus $E = 2.3$ GPa (200 GPa), Poisson's ratio $\nu = 0.37$ (0.3) and density $\rho = 1200$ kg/m^3 (7850 kg/m^3). The dimensions of the beam are given by 0.5 m by 0.01 m by 0.01 m unless otherwise mentioned. The displacement (d) is normalized by the center displacement amplitude for a static loading on a beam fixed at both ends and time (t) is normalized by the angular frequency of the applied loading (ω), i.e.,

$$\tilde{d} = \frac{d}{\left(\frac{F_{\max} L^3}{192EI}\right)}, \tag{6.1}$$

$$\tilde{t} = t\omega, \tag{6.2}$$

where L is the length of the beam and I is the area moment of inertia of the beam cross-section. We consider a harmonic loading of amplitude $F_{max} = 0.01$ N to study the overall bending response of the beam.

6.2 Finite element formulation

The linear elastic beam is modeled as a 2D plane-stress problem discretized into four-node quadrilateral elements. The equations of linear elasticity and its finite element formulation for quadrilateral elements are not presented here but the interested reader can obtain the formulation in any introductory text on the finite element method [66, 67]. As alluded to earlier, we approximate one or more spheres in a granular chain as a continuum bar element. Thus the granular chain is replaced by a series of bar elements. We first obtain a constitutive relation for the bar element which is then combined with that of the quadrilateral elements.

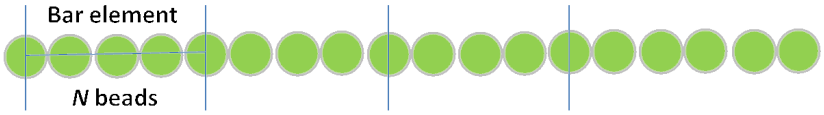

Figure 6.2: A chain of spheres discretized into a number of bar elements with each bar element consisting of N spheres.

Consider a single chain of spheres as shown in Fig. 6.2. Let us assume that there are N number of spheres in a bar element. Here, we note that the centers of the first and N^{th} spheres represent the nodes of the bar element. Thus the length of the element is $l = (N-1)D$, where D is the diameter of a sphere. Consider a compressive force F applied at each end of the element. The total deformation Δ_t in the element can be written as

$$\Delta_t = (N-1)\Delta, \tag{6.3}$$

where Δ is the deformation at a single contact. The deformation at a contact between two spheres can be related to the force applied by using the Hertzian law described in the previous chapters. Thus, Δ_t translates to

$$\Delta_t = (N-1)\left(\frac{F}{K}\right)^{3/2}, \tag{6.4}$$

where $K = 2E_s/(3(1-\nu_s^2))\sqrt{R/2}$ is the contact stiffness and R is the radius of a sphere. The strain in the chain of N spheres can now be approximately determined by dividing the total deformation of Eq. (6.4) by the length of the element. Thus, we obtain

$$\varepsilon = \frac{\Delta_t}{l}, \tag{6.5}$$

$$= \frac{1}{D}\left(\frac{F}{K}\right)^{2/3}. \tag{6.6}$$

Now we translate the above definitions to bar element variables shown in Fig. 6.3. The forces at ends of the bar element are related to the compressive force F by $F_1 = -F_2 = F$. The strain variable as a function of the displacements u_1 and u_2 is

$$\varepsilon = \frac{u_2 - u_1}{l}. \tag{6.7}$$

We now recall that there is no tensile force between the spheres, i.e., there is no contact force if the spheres separate. Combining Eqs. (6.5) and (6.7), the forces F_1 and F_2 of the bar element are now written as

$$F_1 = -F_2 = F = \begin{cases} \frac{K}{(N-1)^{3/2}}(u_1 - u_2)^{3/2} & \text{if } \varepsilon < 0, \\ 0 & \text{otherwise.} \end{cases}$$

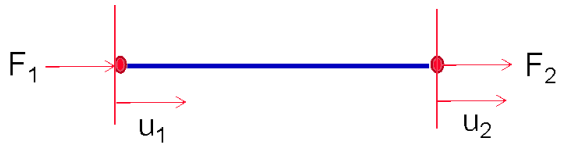

Figure 6.3: Bar element illustrating the nodal displacements and forces.

The bar element's nonlinear force-displacement relation derived above is combined with the linear constitutive stress-strain relations of the quadrilateral elements

of the beam. The force-displacement relations for the bar and quadrilateral elements, and their tangential stiffness matrices are given in Appendix A.

6.3 Implementation

We solve for the displacements at each node of the beam after assembling the Eqs. (A.1) and (A.2). The equations are evidently nonlinear as the force-displacement relations for the bar elements are nonlinear. At each Newton-Raphson iteration we determine the active bar elements ($\varepsilon < 0$) based on the displacements of the previous iteration (or initial displacements for the first iteration). The tangential stiffness matrix is then calculated for the active bar elements. The internal force vector is then computed by adding the contribution of the bar elements at corresponding nodes to the contribution of the beam alone (quadrilateral elements). The Newmark time stepping scheme defines the modified stiffness matrix and force vector, which is then used to determine the displacement increments in a Newton-Raphson iteration. Convergence is monitored by comparing the relative norm of the displacement solution with a tolerance value of 10^{-3}. Finally, acceleration and velocity vectors are updated by using the converged values of displacement. The algorithm used for finding the converged solution for displacements is summarized in Algorithm 1. A more detailed explanation of the algorithm is given in Appendix A.

Algorithm 1 Algorithm for displacement solutions

Initialize $i = 1$
while $(i \leq maxTimeSteps)$ **do**
  Initialize $j = 1$
  while $(condition > tolerance)$ **do**
    Find active bar elements.
    K_{bar} = tangential-Stiffness-Bars
    F_{int} = internal-Force-Vector
    $K_p = K^{quad} + K^{bar} + \frac{1}{\beta \Delta t^2} M^{beam}$
    $\mathbf{F}_p = \mathbf{F}_{ext}^{i+1} + \frac{M^{beam}}{\beta \Delta t^2} \left(\mathbf{d}_i - \mathbf{d}_j + \Delta t \mathbf{v}_i + (0.5 - \beta) \Delta t^2 \mathbf{a}_i \right)$
    $\Delta d = K_p^{-1} (F_p - F_{int})$
    $d_{j+1} = d_j + \Delta d$
    $condition = \frac{\|d_{j+1} - d_j\|}{\|d_j\|}$
    $j \leftarrow j + 1$
  end while
  $\mathbf{a}_{i+1} = \frac{1}{\beta \Delta t^2} \left(\mathbf{d}_{i+1} - \mathbf{d}_i - \Delta t \mathbf{v}_i - (0.5 - \beta) \Delta t^2 \mathbf{a}_i \right)$
  $\mathbf{v}_{i+1} = \mathbf{v}_i + \Delta t \left((1 - \gamma) \mathbf{a}_i + \gamma \mathbf{a}_{i+1} \right)$
  $i \leftarrow i + 1$
end while

6.4 Dynamic code verification

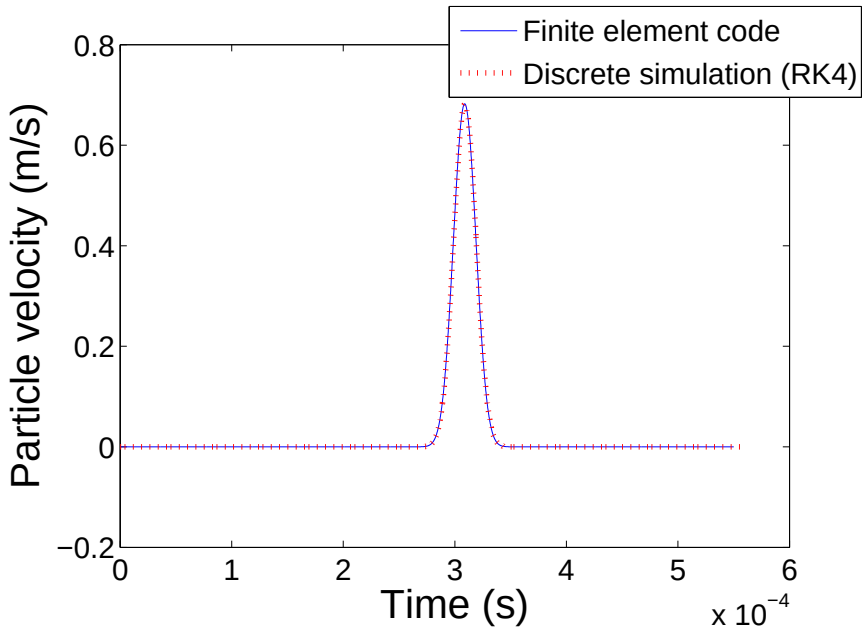

Figure 6.4: Velocity history for the 21^{st} sphere in a 1D chain, comparing the results from the finite element code and Runge-Kutta fourth-order integration.

In this section, we verify the MATLAB program for dynamic nonlinear finite element analysis of embedded granular systems with other sources. First, the nonlinear bar elements representing a granular chain are considered separately for verification purposes. We compare the finite element program results with a Runge-Kutta fourth-order discrete solver which has been previously verified in Chapter 2. Consider a chain of 40 steel spheres, with the first sphere given an initial velocity of 1 m/s. We choose $N = 2$, and thus we have 39 bar elements as each element will have an equivalent of one sphere. The same initial condition is specified to the left node of the first bar element. Figure 6.4 shows the velocity history for the 21^{st} sphere in the granular chain and the corresponding node in the series of 1D bar elements. As evident there, the two results compare very well, thus verifying the finite element formulation for the granular chain.

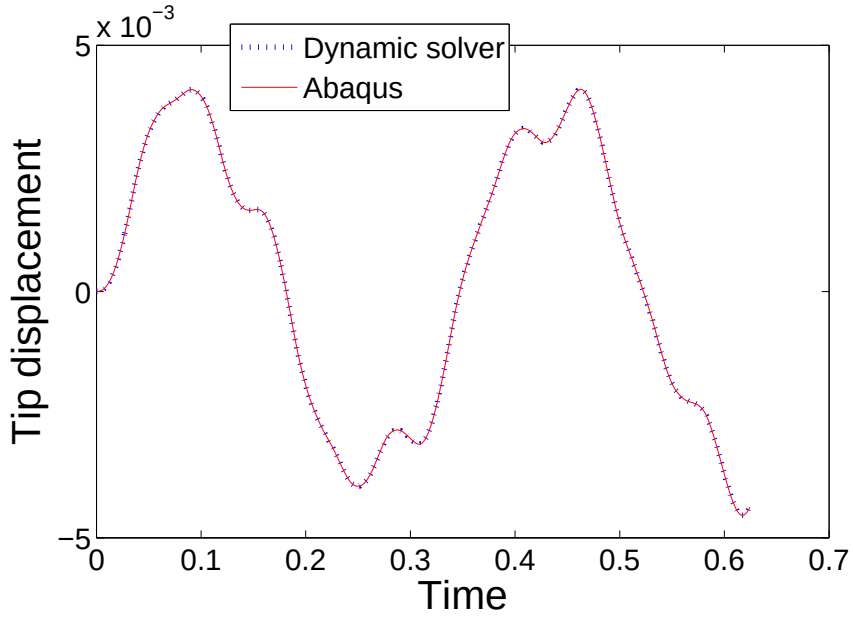

Figure 6.5: Normalized tip displacement history for harmonic type of loading, comparing Abaqus and MATLAB code results.

The finite element code for a linear elastic beam comprising of four-node quadrilateral elements is verified using Abaqus™. We define the following example to

compare the two results. Consider a cantilever beam fixed at the left end and made of epoxy. In this case, the dimensions of the beam are given by 0.4 m by 0.05 m by 0.01 m. As before, a harmonic loading is applied at the right end of the beam and the mesh size is chosen as 20 by 10 elements. Figure 6.5 shows the tip displacement history over a certain interval of time comparing both Abaqus and the finite element (MATLAB) code results. As apparent there, the displacement profiles agree very well. Figure 6.6 then compares the velocity histories for the two cases in the same interval of time, again showing very good agreement.

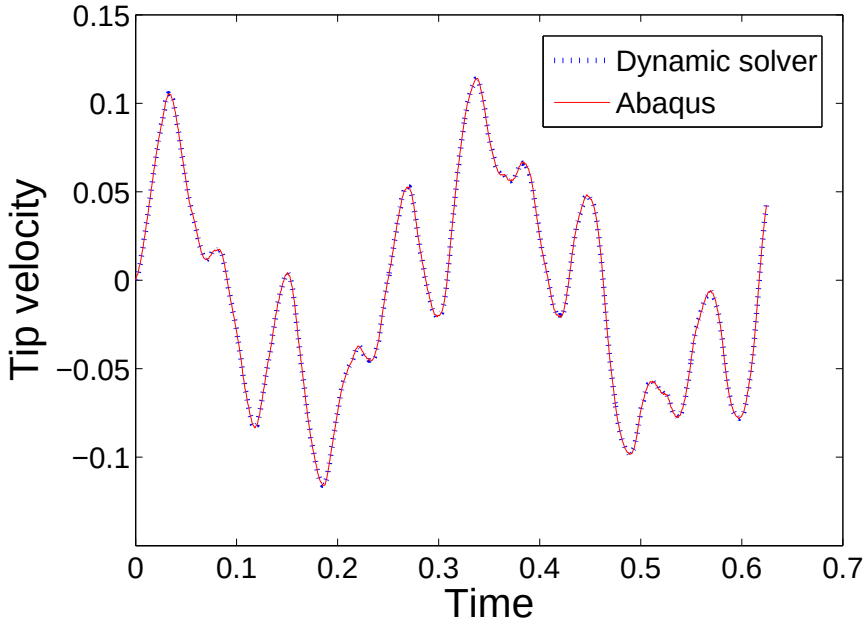

Figure 6.6: Tip velocity (m/s) history for harmonic type of loading, comparing Abaqus and MATLAB code results.

6.5 Convergence studies

In this section, we perform convergence studies with respect to the number of elements in the longitudinal (x) and transverse (y) directions and the time step used in the Newmark method. The convergence studies are conducted for the linear case,

where a harmonic loading of frequency 25 Hz is applied to a beam fixed at both ends. The dimensions and material properties of the beam are same as that mentioned in Sec. 6.1. First, the number of elements in the x direction is kept constant at 20 while that in the y direction is varied. Figure 6.7 shows the displacement history for three cases of discretization. Thus, based on the results for 4 and 6 y-elements, we choose the latter as the converged number in the y direction.

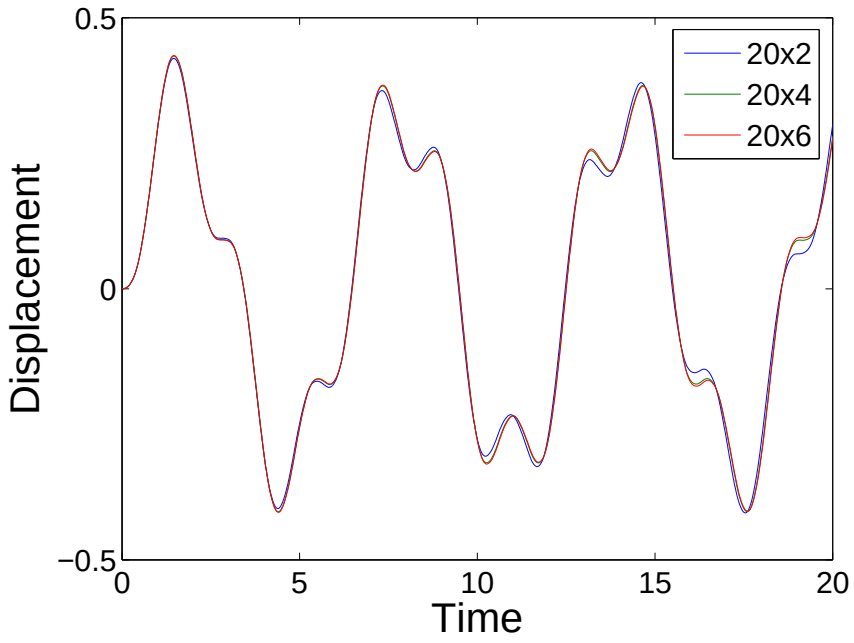

Figure 6.7: Normalized center displacement history showing convergence with respect to number of elements in the y direction. Normalization factors are shown in Sec. 6.1.

Then, we fix the number of y elements as 6 and vary x elements from 20 to 120. Figure 6.8 shows the center displacement history for five cases of mesh size. We can therefore observe that there is substantial variation in the initial three cases, i.e., x-elements of 20, 40 and 60. The number of x-elements is expected to play a bigger role than the y-elements since we are solving a beam bending problem. We ignore small deviations and choose number of x-elements equal to 100 as the converged value.

Finally, we consider the time step used in the Newmark method for marching. Since the run time of a simulation depends on the time step, the convergence study would help us choose an optimum value. Figure 6.9 shows the center displacement history for three values of time step, $\Delta t = 5 \times 10^{-5}$, 1×10^{-4} and 2×10^{-4} seconds. As evident there, the results are not very sensitive to the time step for the chosen applied frequency and time interval. As also indicated by the inset of Fig. 6.9, we choose $\Delta t = 1 \times 10^{-4}$ seconds as an optimum value. Although the above studies were performed for the linear case, we found the convergence to be valid for the nonlinear case as well.

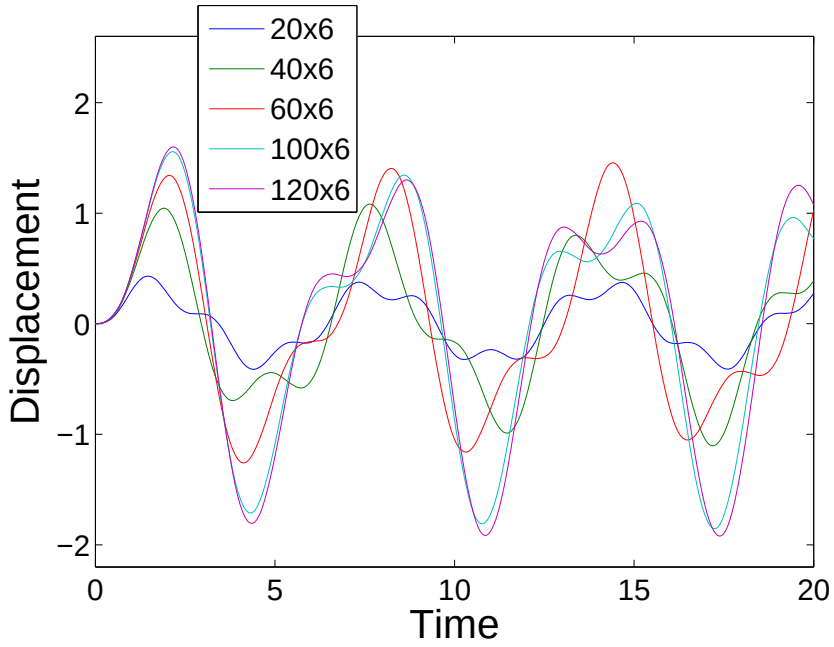

Figure 6.8: Normalized center displacement history showing convergence with respect to number of elements in the x direction.

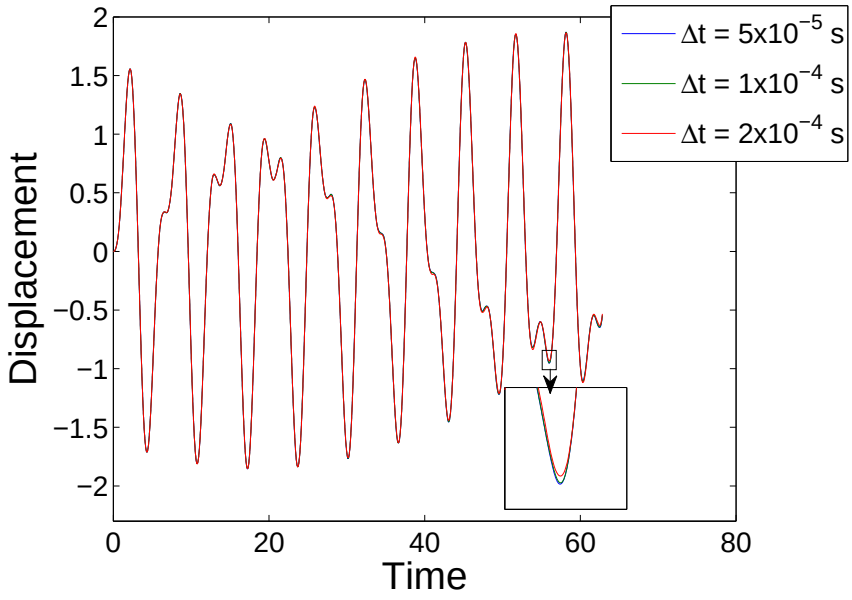

Figure 6.9: Normalized center displacement history showing convergence with respect to time step Δt. Inset shows the magnified version of part of the result for clarity.

6.6 Results: dynamic loading

6.6.1 Linear elastic beam

Consider a linear elastic beam made of epoxy and fixed at both ends. As before, a harmonic loading of a certain frequency is applied at the center of the beam. Figure 6.10 shows the center displacement amplitude as a function of the loading frequency. We observe that at a certain frequency, the displacement amplitude reaches a peak value which corresponds to the familiar point of resonance. The loading frequency is taken in intervals of 0.1 Hz near the peak value and 1 Hz elsewhere. Since the run time of the simulation is finite (2 seconds), the displacement amplitude at resonance is finite but theoretically the value tends to infinity. A theoretical prediction for the

first natural frequency can be obtained from the beam equation as

$$\omega_1 = 2\pi f = \sqrt{\frac{EI}{\rho A L^4}}, \tag{6.8}$$

where A is the cross-section area. The dashed line in Fig. 6.10 corresponds to Eq. (6.8).

Now consider the point of resonance where the frequency is 59.52 Hz. Figure 6.11 shows the center displacement history at the resonance frequency and as expected the displacement amplitude grows linearly with time. Therefore, in absence of damping, the displacement amplitude tends to infinity for a linear elastic beam.

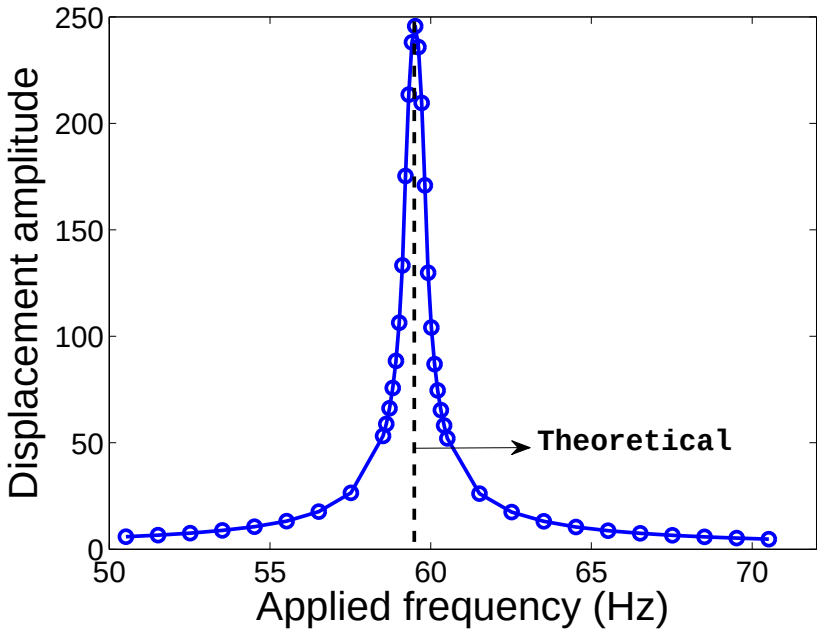

Figure 6.10: Normalized center displacement amplitude as a function of applied frequency for the linear elastic beam without granular chains with the dashed line corresponding to the theoretical prediction for resonance frequency.

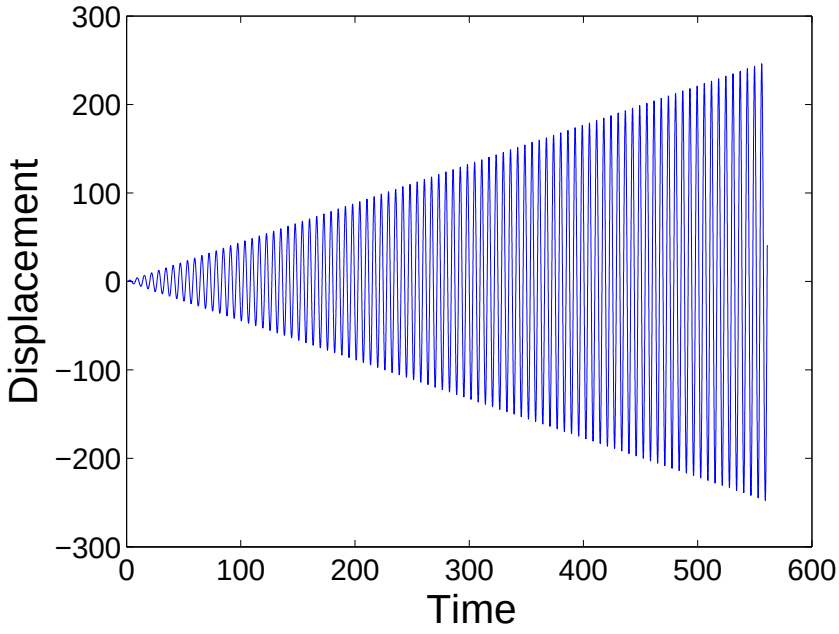

Figure 6.11: Normalized center displacement history for the linear elastic beam without granular chains, showing indefinite growth in amplitude.

6.6.2 Embedded granular system

We now embed a granular chain at the top of the beam, i.e., the line of sphere centers corresponds to the top edge of the beam. The main idea is to embed the chain farthest from the neutral axis to derive maximum advantage during bending. The spheres are made of steel and of diameter 4 mm, resulting in $N = 2.25$. Similar to Sec. 6.6.1, a harmonic loading is applied at the center of the beam at different frequencies. The run time of each simulation is 6 seconds. Figure 6.12 shows the variation of center displacement amplitude with the applied frequency ranging from 40-60 Hz. The frequency is applied in intervals of 0.5 Hz except near the peak value, where the interval gap is either 0.05 Hz or 0.01 Hz. Thus, as in the beam case, the displacement amplitude reaches a peak value at a particular frequency.

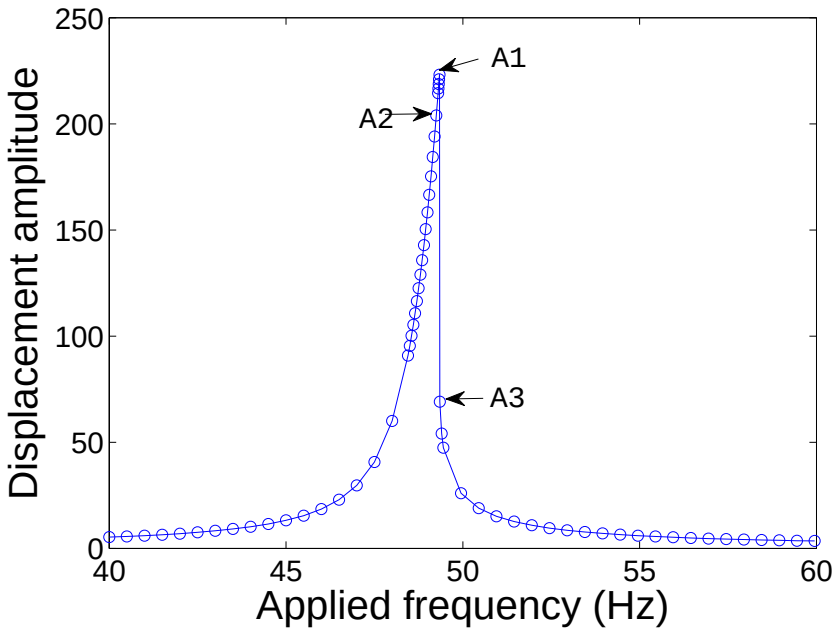

Figure 6.12: Normalized center displacement amplitude as a function of applied frequency for the embedded granular system with no precompression.

However, there are some key differences in the embedded system's response. The variation of the displacement amplitude in Fig. 6.10 is symmetric with respect to the resonance frequency. In Fig. 6.12, however, the displacement amplitude drops sharply on the right side of the peak value. The sharp drop suggests similarity to the jump phenomenon observed in forced oscillations of nonlinear systems [68]. Although the exact reason is yet to be ascertained, the displacement histories at/near the peak location might provide us with more information. Another difference is that the peak displacement amplitude is much lower than that in Fig. 6.10 (which should be multiplied by a factor of 3 since the run time for the linear case was 2 seconds). However, we should note that the masses of the two systems are not equal since the present formulation does not remove the corresponding beam mass to embed the spheres.

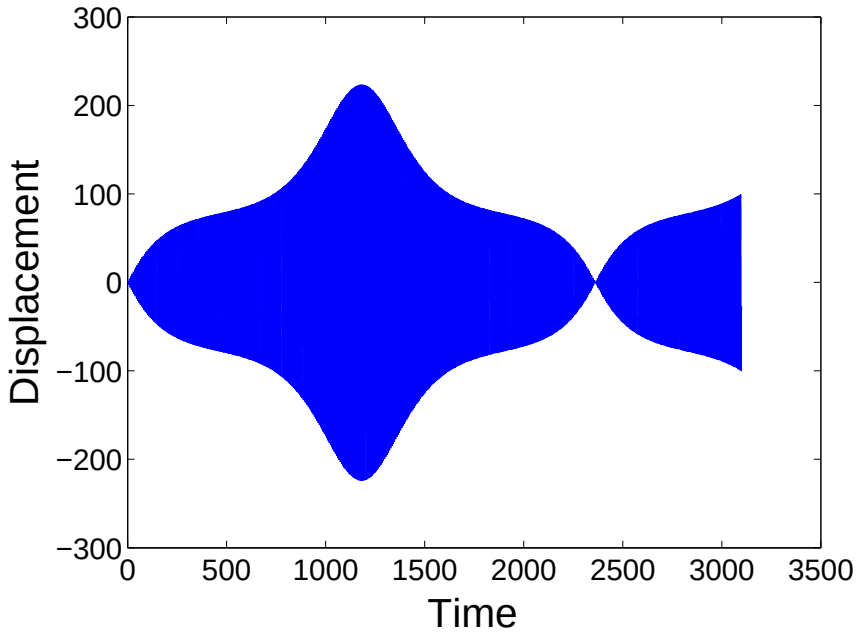

Figure 6.13: Normalized center displacement history for the embedded granular system with no precompression at frequency 49.34 Hz corresponding to the peak displacement in Fig. 6.12.

Figures 6.13 and 6.14 show the displacement histories at frequencies 49.34 Hz and 49.35 Hz, respectively. In Fig. 6.12, the two frequencies correspond to the peak displacement amplitude (labeled 'A1') and the next data point after the sharp decrease (labeled 'A3'), respectively. Firstly, Fig. 6.13 reveals that the displacement *actually* reaches a maximum value at a certain instant and the cycle is repeated similar to beats. Here, we have demonstrated one of the primary results of this study where the displacement amplitude near the point of resonance, although still of high magnitude, reaches a finite value, unlike a linear elastic beam (Fig. 6.11). Figure 6.13 also shows that the variation is highly nonlinear, arising from the Hertzian contact law. The data point labeled 'A2' in Fig. 6.12 has a displacement profile similar to that of the data point labeled 'A1'.

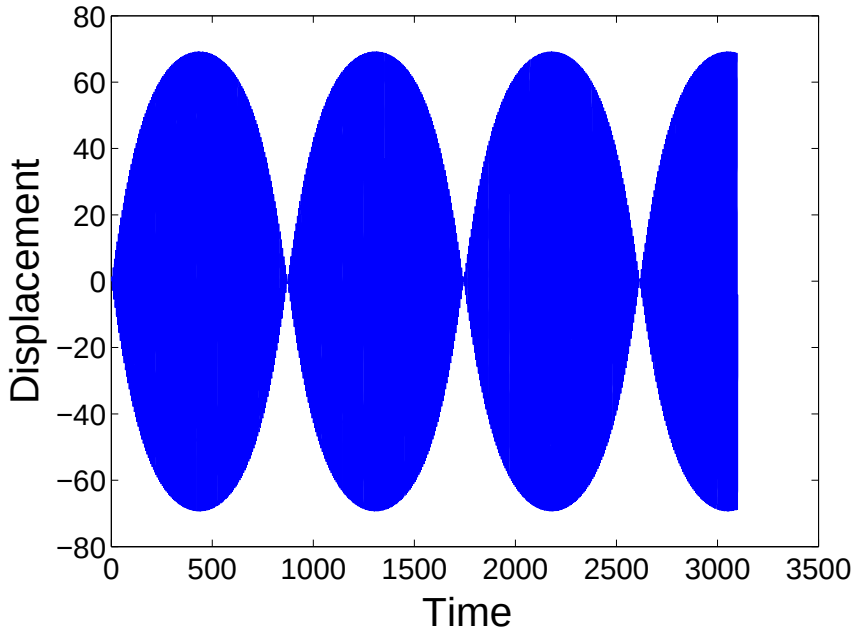

Figure 6.14: Normalized center displacement history for the embedded granular system with no precompression at frequency 49.35 Hz corresponding to the point right of the peak value in Fig. 6.12.

At the right of the peak value, however, the displacement history is very different from that of the peak value. The displacement profile in Fig. 6.14 is similar to the usual beat phenomenon that we also observe in linear elastic beams near the resonance frequency. As also observed in Fig. 6.14, the displacement amplitude is about three times lower, the beat frequency is around two times higher than that of the variation at the peak value (Fig. 6.13). Thus we observe a drastic change although the change in applied frequency is just 0.01 Hz.

Let us now suppose that the spheres are precompressed at inter-particle contacts, holding the two ends of the chain through the built-in ends of the embedded system. Let us define a nondimensional parameter $\Delta = \delta/R$, where δ is the amount or level of precompression at each contact and R is the radius of a sphere. Figure 6.15 shows the variation of the center displacement amplitude with frequency of loading for different levels of precompression ranging from $\Delta = 0$ to 5×10^{-4} which, for steel

beads of diameter 4 mm corresponds to a precompression level of 0 to 4.63 N. We earlier considered the case of $\Delta = 0$ in Fig. 6.12. As evident in Fig. 6.15, the peak displacement amplitude and the frequency at which it occurs change with the applied precompression level. The frequency at which the displacement amplitude peaks shows a monotonic increase with Δ while the displacement amplitude increases upto $\Delta = 1 \times 10^{-4}$ and then decreases. Furthermore, there is no particular trend in our results as to what direction the sharp decrease in displacement amplitude occurs. In the first two cases, i.e., $\Delta = 0$ and 1×10^{-4}, the sharp decrease is to the right of the peak value while it is to the left for the other two cases. Thus, we believe that there is a value of Δ where the jump phenomenon changes from hardening to softening behavior.

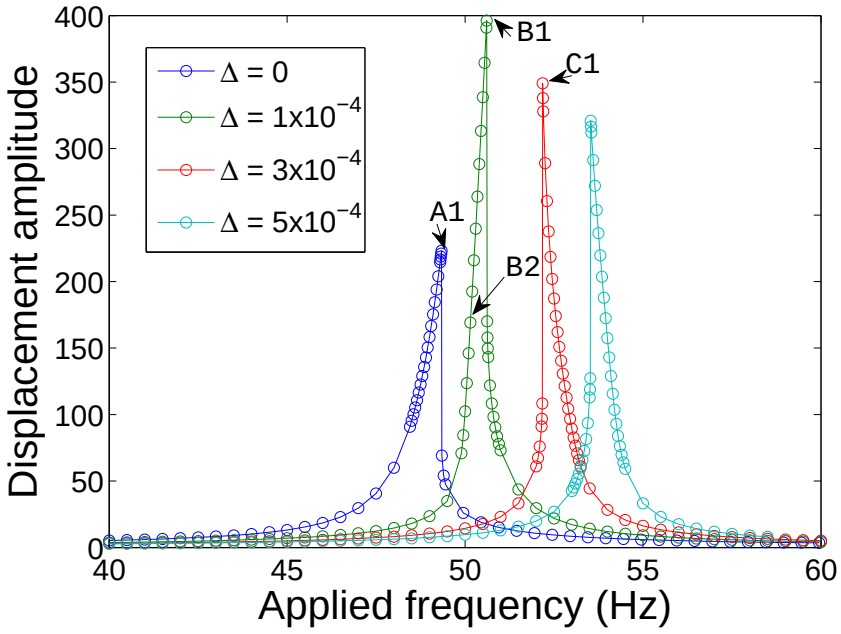

Figure 6.15: Normalized center displacement amplitude as a function of applied frequency for the embedded granular system for different levels of precompression (Δ).

Figure 6.16 compares the displacement history at the peaks for different levels of precompression, labeled 'A1', 'B1' and 'C1' in Fig. 6.15. As evident there, the

displacement profiles are very similar and the displacement reaches a finite value in each case. Further, the beat frequency varies with precompression. Figure 6.17 shows the displacement history for $\Delta = 1 \times 10^{-4}$ at frequency 50.15 Hz, labeled 'B2' in Fig. 6.15. We note that the displacement profile in Fig. 6.17 is closer to a triangular shape while the profile in Fig. 6.14 is closer to a circular shape. We also observe that the displacement profile in Fig. 6.17 occurs at frequencies whose amplitudes are similar to that of the point at sharp decrease, but on the other side of the peak value. Whereas the response in Fig. 6.14 occurs for frequencies corresponding to the point at sharp decrease/increase for different levels of precompression (for example, case 'A3' in Fig. 6.12).

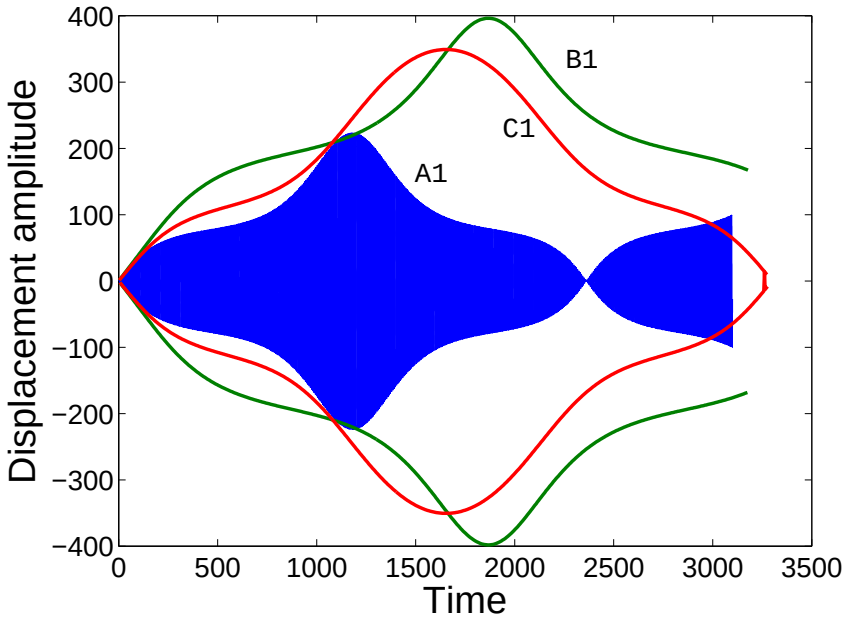

Figure 6.16: Normalized center displacement history for different levels of precompression (Δ) at frequencies corresponding to the peaks in Fig. 6.15.

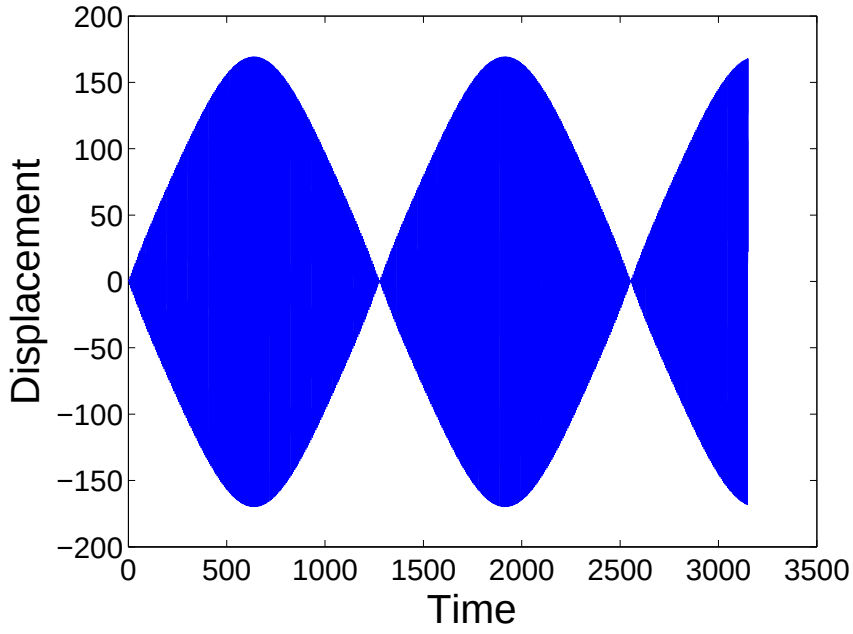

Figure 6.17: Normalized center displacement history for $\Delta = 1 \times 10^{-4}$ at frequency 50.15 Hz, labeled 'B2' in Fig. 6.15.

Precompression introduces an initial "stiffness" component which changes the natural frequency of vibration in the embedded system. The variation in the peak displacement amplitude with precompression level depends on the applied force magnitude relative to the precompression force level. In summary, we have demonstrated a novel way through which the resonance frequency of the embedded system can be controlled along with the key result that the displacement amplitude at resonance reaches a finite value.

6.7 Conclusions

In this chapter, we considered a practical aspect of granular media by performing a preliminary study of embedded granular systems wherein a granular chain was embedded in a linear elastic beam and then analyzed numerically. The beam was modeled using four-node quadrilateral elements while a continuum approximation

of the granular chains was utilized to model the chains as nonlinear bar elements. A harmonic loading applied at the center of the embedded system revealed that it is actually possible to overcome resonance in the sense that the deflection amplitude, although high, stops growing indefinitely, unlike a linear elastic beam alone. We have therefore demonstrated in this study a practical way of taking advantage of the nonlinearity at inter-particle contacts. Furthermore, application of precompression in the granular chains allowed us to control the frequency at which the deflection amplitude reaches a maximum. Embedded granular systems have thus shown the potential to control the vibration response of beams.

Chapter 7

Conclusions and Future Work

7.1 Key contributions

One of the key objectives of the current work has been to address some of the fundamental aspects in granular media to be ultimately able to deploy them in practical applications. On that front, the focus has been on the effect of randomness and plane wave propagation in granular media. Finally, a preliminary study on embedded granular systems has been conducted to apply the fundamental understandings of granular media including the role of nonlinearity and precompression.

The key contributions of the work described in this thesis are as follows:

- A series of snapshots of wave propagation revealed that solitary waves are absent in random granular chains.
- Reflection and transmission processes occurring at each inter-particle contact lead to a progressive decay of the leading pulse amplitude showing the presence of two decay regimes: an initial exponential regime transitioning into a universal power-law regime, valid for all levels of randomness.
- The decay behavior qualitatively remains the same for randomness in mass, Young's modulus and radius, while the decay rate was found to be maximum for randomness in radius for a given degree of randomness.
- The energy distribution in random chains showed a gradual transfer from potential to kinetic energy.

- The effect of randomness in 1D and 2D random granular media are fundamentally similar with regards to decay, where the two decay regimes, an exponential and a universal power-law, are also present in the 2D system for decay along a single direction.

- Randomness in mass leads to minimal changes in the wavefront profile but the wavefront speed has been shown to decrease with increase in degree of randomness due to increasing reflections at inter-particle contacts.

- Decay rate has been found to depend on direction and level of randomness, showing potential for tailoring waves.

- For monodisperse spheres under uniform perpendicular impact, ordered packings such as hexagonal, face-centered cubic and body-centered cubic arrangements always result in a single leading pulse, a solitary wave.

- An equivalence between solitary wave properties in the higher dimensional structures and 1D chains was derived, leading to a key result of a universal wavefront speed-force amplitude relation for the 2D and 3D structures.

- In the angular impact case, the shear component of the loading decays very rapidly in several regimes, i.e., an initial exponential regime and then a series of linear regimes.

- For wave propagation in periodic square packing system with intruders, an equivalent dimer chain comprising of nonlocal interactions between heavier spheres has been derived.

- A set of discrete values of two key nondimensional parameters ϵ and α demonstrated a new family of solitary waves in the nonlocal dimer system, including

a unique case of a solitary wave similar to that of monodisperse or homogeneous chains.

- A solitary wave map has been generated along with real material data showing different material combinations that allow solitary waves and locally maximum decay, demonstrating a way to tune the granular system depending on the objective.

- Harmonic loading on embedded granular systems revealed some novel ways to control resonance. The deflection amplitude of the embedded granular system reached a peak value at a certain time, unlike a linear elastic beam. Also, application of precompression to the chains allowed us to change the frequency at which deflection reached a maximum value.

7.2 Future directions

Several paths for future research direction are suggested herein, which can be undertaken either independently or by combining two or more topics. In the topic of randomness in granular media, we observed the universal power law regime in force/kinetic energy amplitude decay. One of the key questions that remains open is to explain the phenomena associated with the power-law regime including the formation of the silent zone. We believe that considerable amount of knowledge is required in the area of wave scattering behavior to understand the fundamental mechanisms. As mentioned earlier, we could get more information from disorder in other systems such as photonic and dielectric lattices to explain the behavior in granular media. Furthermore, the random phenomena can be better understood by applying the techniques of stochastic calculus. In addition, since the level of randomness is usually small in reality compared to the actual property of the ma-

terial, an asymptotic analysis can be performed to predict the solutions at small variations. In all the theoretical approaches mentioned above, we point out that it is more convenient to start with a continuous version of the discrete PDE, for example, by using a long-wave approximation.

Another direction of research would be to incorporate preferential randomness along certain paths for the granular system to have wave tailoring capabilities. As reported in the current work, randomness can lead to rapid decay of kinetic energy and the decay rate can be direction-dependent in 2D and 3D systems. Therefore, we could take advantage of the above fact by having paths with random chains to mitigate the incoming wave kinetic energy to a desired level. If the randomness is in the radii of the particles, the packing itself will be random, leading to a more complex dynamic behavior. Although there has been some progress with regards to wave propagation in random packings, there has not been a sincere effort to understand from a fundamental level such as the presence of force chains. There has been extensive research in static packings but the dynamic analysis could give us a clue regarding the dominant pathways so that wave tailoring can be sought after. Another source of randomness that researchers have observed in experiments is the presence of gaps (absence of inter-particle contacts). Substantial wave mitigation can occur along certain pathways due to gaps and therefore can potentially be taken advantage of in tailoring the wave.

In the plane wave propagation study, the idea of comparing the solitary wave map with real material properties is to motivate future experiments to verify and take advantage of the square packing system with intruders. Although the numerical simulations considered periodic boundary conditions, the results will be still valid in the case of experiments but sufficiently far from the boundaries. Therefore, experiments will serve as the first step for further research, paving the way for finding similar higher dimensional systems having wave-preserving and wave-

mitigating natures. Another path for future research would be to determine the effect of inhomogeneity on plane wave propagation. As a consequence, we can think of very interesting applications such as cloaking which are frequently studied in transmission of electromagnetic or acoustic waves. We can think of optimizing the properties of the particles surrounding the inhomogeneity in order to preserve the plane wave characteristics of the incoming wave, thus 'hiding' the inhomogeneity.

In all the studies in the present work, the loading is uniform, i.e., equal magnitudes of impact velocities. Since the primary motivation for the plane wave study is to address the complex loadings that occur in reality, we can consider more general types of loadings. One type of nonuniform loading is to have a triangular profile for the impact velocities, i.e., alternating spheres have equal magnitudes. We can then look at the case of random loading conditions, firstly in velocity magnitudes alone and finally in both magnitude and direction. We can also consider introducing precompression as it is relatively easier to apply in the case of 2D/3D systems than 1D chains due to alignment issues. A solitary wave map for different levels of precompression can now be obtained to be able to actively control the wave-preserving and wave-mitigating natures without changing the material or geometric properties of the particles. Some researchers have utilized 1D chains and precompression to develop acoustic lens to focus the impact energy to a point. For plane wave propagation in 2D/3D systems, there could be precompression in preferential directions in order to concentrate the planar impact to a single location.

In the present work on embedded granular systems, some assumptions are made in the finite element formulation. As a further step, we could overcome some assumptions by reformulating the whole problem. For example, the present formulation does not take into account that some matrix material has to be removed for the spheres to be inserted in the beam. In terms of application, we could build energy harvesting systems wherein the granular chains convert the external

vibrations to useful energy. There are few studies in the open literature that provide ways to contain the impact energy within the granular system (for e.g., see Ref. [12]). In the matrix and granular chain composite system, the granular chain can be utilized to absorb the impact energy as well as the energy due to vibrations. One could possibly use magnetized spheres to be able to convert to a suitable form of energy.

In the current study, the impact velocity is assumed to be low enough so that inter-particle contacts undergo elastic deformation. But it is desirable to design systems for high impact loading, and this will lead to plastic deformation. As noted earlier, precompression will enable us to actively control the bending response but for very low amplitudes. In order to use granular systems multiple times, we can precondition the spheres instead to sustain high amplitude forces and still remain in the elastic regime [69]. Finally, we can extend the current study to investigate bending behavior of plates with embedded granular chains. Plates offer more flexibility for material design in the sense that the bending modes have more complex bending profiles. Therefore we can think of embedding curved granular chains, where different chains get 'activated' by different modes. Passive control is thus built-in within the system. If we consider a plate fixed on two sides then applying precompression would be feasible as in the case of beams, and also can precondition the spheres.

We may ideally want to have the weight of the embedded system to be same as that of the plate without the chains. Since some of the matrix material has to be removed to embed the spheres, we should make the spheres hollow in order to have equal mass. Let us suppose that the outer radius of the spheres is R and the wall thickness is h, and also that we have the flexibility to change the materials of both the matrix (of density ρ_1) and the spheres (of density ρ_2). We can now derive a relation between the wall thickness and the ratio of densities ($\lambda = \rho_1/\rho_2$) by equating the cylindrical matrix mass that needs to be removed to the total mass of the hollow

spheres as

$$\frac{h}{R} = \left[1 - \left(\frac{2 - 3\lambda}{2}\right)^{1/3}\right]. \tag{7.1}$$

Figure 7.1 shows above function for different values of λ and also some representative material combinations. For example, the label 'epoxy, steel' indicates that the matrix is epoxy and the spheres are made of steel, which gives $h/R \approx 0.09$. Therefore, we can make progress in this regard by using hollow spheres of relevant thickness.

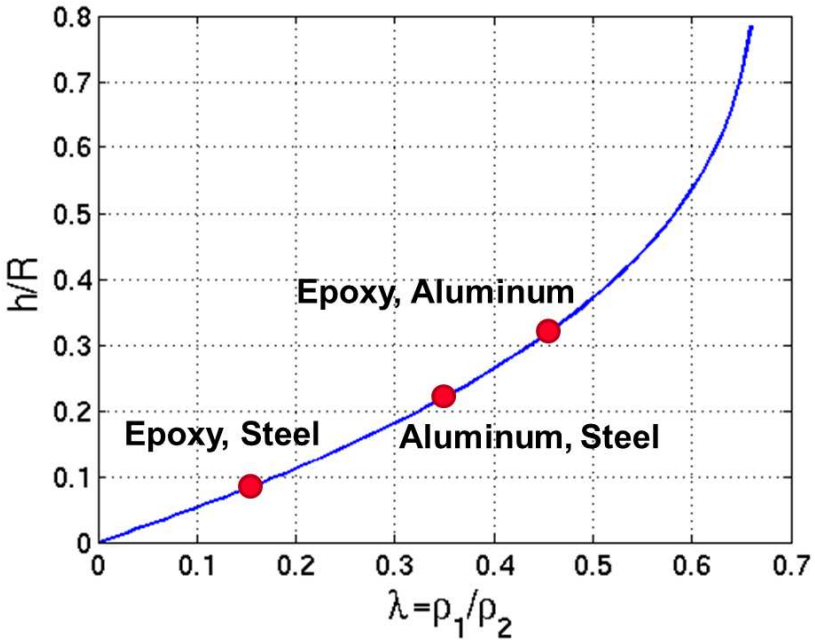

Figure 7.1: Normalized wall thickness (h/R) of the hollow spheres as a function of the density ratio ($\lambda = \rho_1/\rho_2$) and few representative material combinations.

Appendix A

Finite element formulation

A.1 Force-displacement relations

The force-displacement relations for a bar element and a linear quadrilateral element are

$$\left\{ \begin{array}{c} F_{1x} \\ F_{2x} \end{array} \right\} = \frac{K}{(N-1)^{3/2}} \left\{ \begin{array}{c} (u_1 - u_2)^{3/2} \\ -(u_1 - u_2)^{3/2} \end{array} \right\} \tag{A.1}$$

and

$$\{F\} = [k]\,\{d\}\,, \tag{A.2}$$

respectively. The element stiffness matrix $[k]$ in Eq. (A.2) is determined by

$$[k] = \iiint_{V^e} [B]^T\,[D]\,[B]\,dV, \tag{A.3}$$

where V^e is the volume of the element, $[B]$ is the deformation matrix, and $[D]$ is the constitutive matrix. For plane stress assumption, $[D]$ is given by

$$[D] = \frac{E}{1-\nu^2} \begin{bmatrix} 1 & \nu & 0 \\ \nu & 1 & 0 \\ 0 & 0 & \frac{1-\nu}{2} \end{bmatrix}. \tag{A.4}$$

The reader is directed to any introductory text on the finite element method for a more detailed derivation of the element stiffness matrix.

A.2 Tangent stiffness matrix

We need to compute the tangent stiffness matrix at every iteration of the Newton-Raphson procedure. Consider a quadrilateral element with a bar element located on the edge with node numbers 1 and 2. The total internal force vector will now include the contribution of the quadrilateral and bar elements given by

$$\mathbf{F}_{\text{int}} = \mathbf{F}_{\text{int}}^{quad} + \mathbf{F}_{\text{int}}^{bar}, \tag{A.5}$$

where the internal force vectors $\mathbf{F}_{int}^{bar}$ and $\mathbf{F}_{int}^{quad}$ are defined in Eqs. (A.1) and (A.2), respectively. From Eq. (A.5), the internal force at node 1 is given by

$$F_1 = K_{11}^{quad} u_1 + \cdots + K_1^{bar}(u_1 - u_2)^{3/2}, \tag{A.6}$$

where K_{11}^{quad} and $K_1^{bar} = K/(N-1)^{3/2}$ are the corresponding components in the stiffness matrices. Therefore, the first term in the tangent stiffness matrix is

$$\frac{dF_1}{du_1} = K_{11}^{quad} + \frac{3}{2} K_1^{bar}(u_1 - u_2)^{1/2}. \tag{A.7}$$

Similarly, other elements of the tangent stiffness matrix can be derived to get

$$\frac{d\mathbf{F}_{\text{int}}}{d\mathbf{u}} = K^{quad} + K^{bar} \tag{A.8}$$

$$= K^{quad} + \begin{bmatrix} \frac{3}{2}K_1^{bar}(u_1 - u_2)^{1/2} & 0 & -\frac{3}{2}K_1^{bar}(u_1 - u_2)^{1/2} & \\ 0 & 0 & 0 & \cdots \\ -\frac{3}{2}K_1^{bar}(u_1 - u_2)^{1/2} & 0 & \frac{3}{2}K_1^{bar}(u_1 - u_2)^{1/2} & \\ & \vdots & & \ddots \end{bmatrix}. \tag{A.9}$$

We note that the tangent stiffness matrix for the bar elements K^{bar} is determined only if one or more bar elements have negative strain.

A.3 Newmark method

The Newton-Raphson iterative procedure combined with the incremental method is followed to update the displacements at each load step i. Let the external and internal force vectors at load step $i+1$ be $\mathbf{F}_{ext}^{i+1}$ and $\mathbf{F}_{int}^{i+1}$, respectively. First, we seek to satisfy the equilibrium condition

$$\mathbf{F}_{ext}^{i+1} - \mathbf{F}_{int}^{i+1} = 0. \tag{A.10}$$

A Taylor series expansion of $\mathbf{F}_{int}^{i+1}$ at iteration j for a small increment $\Delta\mathbf{d}$ in displacement vector gives

$$\mathbf{F}_{ext}^{i+1} = \mathbf{F}_{\text{int}}^{j} + \frac{d\mathbf{F}_{\text{int}}}{d\Delta\mathbf{d}}\Delta\mathbf{d} + \mathrm{O}\left(d\Delta\mathbf{d}^2\right). \tag{A.11}$$

Using terms upto first order in Eq. (A.11), we get

$$\Delta\mathbf{d} = \left(\frac{d\mathbf{F}_{\text{int}}}{d\Delta\mathbf{d}}\right)_j^{-1}\left(\mathbf{F}_{ext}^{i+1} - \mathbf{F}_{\text{int}}^{j}\right), \tag{A.12}$$

$$= (K_p)_j^{-1}\left(\mathbf{F}_p - \mathbf{F}_{\text{int}}^{j}\right), \tag{A.13}$$

where K_p and F_p are the algorithmic stiffness matrix and force vectors derived from the Newmark method [66], respectively, given by

$$K_p = K^{quad} + K^{bar} + \frac{1}{\beta\Delta t^2}M^{beam}, \tag{A.14}$$

$$\mathbf{F}_p = \mathbf{F}_{ext}^{i+1} + \frac{M^{beam}}{\beta\Delta t^2}\left(\mathbf{d}_i - \mathbf{d}_j + \Delta t\mathbf{v}_i + (0.5-\beta)\Delta t^2\mathbf{a}_i\right), \tag{A.15}$$

where β is a Newmark parameter, $\mathbf{v}_i$ and $\mathbf{a}_i$ are velocity and acceleration vectors, respectively. The displacement from the previous iteration j is now updated as

$$\mathbf{d}_{j+1} = \mathbf{d}_j + \Delta\mathbf{d}. \tag{A.16}$$

The above steps are repeated until a desired convergence is obtained. Finally, we get a converged value for the displacement vector $\mathbf{d}_{i+1}$. The acceleration and velocity vectors can now be updated using the Newmark equations as

$$\mathbf{a}_{i+1} = \frac{1}{\beta \Delta t^2}\left(\mathbf{d}_{i+1} - \mathbf{d}_i - \Delta t \mathbf{v}_i - (0.5 - \beta)\Delta t^2 \mathbf{a}_i\right), \tag{A.17}$$

$$\mathbf{v}_{i+1} = \mathbf{v}_i + \Delta t\left((1 - \gamma)\mathbf{a}_i + \gamma \mathbf{a}_{i+1}\right), \tag{A.18}$$

where γ is another Newmark parameter. The mass matrix of the beam M^{beam} in Eq. (A.15) is calculated by adding the contributions of the quadrilateral and bar elements. Element mass matrices for the quadrilateral elements are determined using

$$[m] = \iiint_{V^e} \rho [N]^T [N] \, dV, \tag{A.19}$$

where $[N]$ is the matrix of shape functions. Row-sum technique is then employed to obtain the global lumped mass matrix for the quadrilateral elements. For the bar elements, mass of the element is shared equally between the two nodes, and the resulting mass matrix is added to that of the quadrilateral elements to obtain M^{beam}.

References

[1] A. Mehta, *Granular physics*. Cambridge University Press, 2007.

[2] V. F. Nesterenko, *Dynamics of Heterogeneous Materials*. New York: Springer Verlag, 2001.

[3] S. Sen, J. Hong, J. Bang, E. Avalos, and R. Doney, "Solitary waves in the granular chain," *Phys. Rep.*, vol. 462, no. 2, pp. 21–66, 2008.

[4] K. L. Johnson, *Contact Mechanics*. Cambridge University Press, Cambridge, 1985.

[5] V. F. Nesterenko, "Propagation of nonlinear compression pulses in granular media," *J. Appl. Mech. Tech. Phys.*, vol. 24, no. 5, pp. 733–743, 1983.

[6] S. Sen and M. Manciu, "Solitary wave dynamics in generalized hertz chains: An improved solution of the equation of motion," *Phys. Rev. E*, vol. 64, no. 5, p. 056605, 2001.

[7] S. Sen, M. Manciu, and J. D. Wright, "Solitonlike pulses in perturbed and driven hertzian chains and their possible applications in detecting buried impurities," *Phys. Rev. E.*, vol. 57, no. 2, p. 2386, 1998.

[8] J. Hong and A. Xu, "Nondestructive identification of impurities in granular medium," *Appl. Phys. Lett.*, vol. 81, no. 25, pp. 4868–4870, 2002.

[9] D. Khatri, C. Daraio, and P. Rizzo, "Highly nonlinear waves' sensor technology for highway infrastructures," vol. 6934, p. 69340U, SPIE, 2008.

[10] A. Spadoni and C. Daraio, "Generation and control of sound bullets with a nonlinear acoustic lens," *Proceedings of the National Academy of Sciences*, vol. 107, no. 16, pp. 7230–7234, 2010.

[11] V. F. Nesterenko, C. Daraio, E. B. Herbold, and S. Jin, "Anomalous wave reflection at the interface of two strongly nonlinear granular media," *Phys. Rev. Lett.*, vol. 95, p. 158702, Oct 2005.

[12] C. Daraio, V. F. Nesterenko, E. B. Herbold, and S. Jin, "Energy trapping and shock disintegration in a composite granular medium," *Phys. Rev. Lett.*, vol. 96, no. 5, p. 058002, 2006.

[13] E. Fermi, J. Pasta, and S. Ulam, "Studies of nonlinear problems," tech. rep., I, Los Alamos Scientific Laboratory Report No. LA-1940, 1955.

[14] N. J. Zabusky and M. D. Kruskal, "Interaction of solitons in a collisionless plasma and the recurrence of initial states," *Phys. Rev. Lett*, vol. 15, no. 6, pp. 240–243, 1965.

[15] A. Lazaridi and V. Nesterenko, "Observation of a new type of solitary waves in a one-dimensional granular medium," *Journal of Applied Mechanics and Technical Physics*, vol. 26, no. 3, pp. 405–408, 1985.

[16] V. Nesterenko, "Solitary waves in discrete media with anomalous compressibility and similar to," *Le Journal de Physique IV*, vol. 4, no. C8, pp. C8–729, 1994.

[17] V. Nesterenko, A. Lazaridi, and E. Sibiryakov, "The decay of soliton at the contact of two acoustic vacuums," *Journal of applied mechanics and technical physics*, vol. 36, no. 2, pp. 166–168, 1995.

[18] C. Coste, E. Falcon, and S. Fauve, "Solitary waves in a chain of beads under hertz contact," *Phys. Rev. E.*, vol. 56, no. 5, p. 6104, 1997.

[19] R. MacKay, "Solitary waves in a chain of beads under hertz contact," *Physics Letters A*, vol. 251, no. 3, pp. 191–192, 1999.

[20] G. Friesecke and J. A. Wattis, "Existence theorem for solitary waves on lattices," *Communications in mathematical physics*, vol. 161, no. 2, pp. 391–418, 1994.

[21] J.-Y. Ji and J. Hong, "Existence criterion of solitary waves in a chain of grains," *Physics Letters A*, vol. 260, no. 1, pp. 60–61, 1999.

[22] C. Daraio, V. F. Nesterenko, E. B. Herbold, and S. Jin, "Strongly nonlinear waves in a chain of teflon beads," *Phys. Rev. E.*, vol. 72, no. 1, p. 016603, 2005.

[23] M. A. Porter, C. Daraio, I. Szelengowicz, E. B. Herbold, and P. Kevrekidis, "Highly nonlinear solitary waves in heterogeneous periodic granular media," *Physica D: Nonlinear Phenomena*, vol. 238, no. 6, pp. 666–676, 2009.

[24] N. Boechler, G. Theocharis, and C. Daraio, "Bifurcation-based acoustic switching and rectification," *Nature materials*, vol. 10, no. 9, pp. 665–668, 2011.

[25] R. Doney and S. Sen, "Decorated, tapered, and highly nonlinear granular chain," *Phys. Rev. Lett.*, vol. 97, no. 15, p. 155502, 2006.

[26] R. L. Doney, J. H. Agui, and S. Sen, "Energy partitioning and impulse dispersion in the decorated, tapered, strongly nonlinear granular alignment: A system with many potential applications," *J. Appl. Phys.*, vol. 106, no. 6, p. 064905, 2009.

[27] U. Harbola, A. Rosas, M. Esposito, and K. Lindenberg, "Pulse propagation in tapered granular chains: An analytic study," *Phys. Rev. E.*, vol. 80, no. 3, p. 031303, 2009.

[28] U. Harbola, A. Rosas, A. H. Romero, M. Esposito, and K. Lindenberg, "Pulse propagation in decorated granular chains: An analytical approach," *Phys. Rev. E.*, vol. 80, no. 5, p. 051302, 2009.

[29] S. Job, F. Melo, A. Sokolow, and S. Sen, "How hertzian solitary waves interact with boundaries in a 1d granular medium," *Physical review letters*, vol. 94, no. 17, p. 178002, 2005.

[30] L. Vergara, "Scattering of solitary waves from interfaces in granular media," *Physical review letters*, vol. 95, no. 10, p. 108002, 2005.

[31] E. Hascoët and H. J. Herrmann, "Shocks in non-loaded bead chains with impurities," *Eur. Phys. J. B*, vol. 14, no. 1, pp. 183–190, 2000.

[32] S. Job, F. Santibanez, F. Tapia, and F. Melo, "Wave localization in strongly nonlinear hertzian chains with mass defect," *Phys. Rev. E*, vol. 80, no. 2, p. 025602, 2009.

[33] R. K. Pal, A. P. Awasthi, and P. H. Geubelle, "Wave propagation in elasto-plastic granular systems," *Granul. Matter*, vol. 15, no. 6, pp. 747–758, 2013.

[34] R. Carretero-González, D. Khatri, M. A. Porter, P. Kevrekidis, and C. Daraio, "Dissipative solitary waves in granular crystals," *Physical review letters*, vol. 102, no. 2, p. 024102, 2009.

[35] A. Sokolow, E. Bittle, and S. Sen, "Solitary wave train formation in hertzian chains," *EPL (Europhysics Letters)*, vol. 77, no. 2, p. 24002, 2007.

[36] S. Job, F. Melo, A. Sokolow, and S. Sen, "Solitary wave trains in granular chains: experiments, theory and simulations," *Granular Matter*, vol. 10, no. 1, pp. 13–20, 2007.

[37] R. K. Pal, A. P. Awasthi, and P. H. Geubelle, "Characterization of wave propagation in elastic and elastoplastic granular chains," *Physical Review E*, vol. 89, no. 1, p. 012204, 2014.

[38] A. Chatterjee, "Asymptotic solution for solitary waves in a chain of elastic spheres," *Physical Review E*, vol. 59, no. 5, p. 5912, 1999.

[39] K. Jayaprakash, Y. Starosvetsky, and A. F. Vakakis, "New family of solitary waves in granular dimer chains with no precompression," *Physical Review E*, vol. 83, no. 3, p. 036606, 2011.

[40] K. Jayaprakash, Y. Starosvetsky, A. F. Vakakis, and O. V. Gendelman, "Nonlinear resonances leading to strong pulse attenuation in granular dimer chains," *Journal of nonlinear science*, vol. 23, no. 3, pp. 363–392, 2013.

[41] R. Potekin, K. Jayaprakash, D. McFarland, K. Remick, L. Bergman, and A. Vakakis, "Experimental study of strongly nonlinear resonances and anti-resonances in granular dimer chains," *Experimental Mechanics*, vol. 53, no. 5, pp. 861–870, 2013.

[42] K. Jayaprakash, A. F. Vakakis, and Y. Starosvetsky, "Solitary waves in a general class of granular dimer chains," *Journal of Applied Physics*, vol. 112, no. 3, p. 034908, 2012.

[43] M. Manciu, S. Sen, and A. Hurd, "Impulse propagation in dissipative and disordered chains with power-law repulsive potentials," *Physica D*, vol. 157, no. 3, pp. 226–240, 2001.

[44] L. Ponson, N. Boechler, Y. M. Lai, M. A. Porter, P. G. Kevrekidis, and C. Daraio, "Nonlinear waves in disordered diatomic granular chains," *Phys. Rev. E.*, vol. 82, no. 2, p. 021301, 2010.

[45] A. Shukla and C. Damania, "Experimental investigation of wave velocity and dynamic contact stresses in an assembly of disks," *Exp. Mech.*, vol. 27, no. 3, pp. 268–281, 1987.

[46] A. Shukla, "Dynamic photoelastic studies of wave propagation in granular media," *Opt. Laser. Eng.*, vol. 14, no. 3, pp. 165–184, 1991.

[47] A. Shukla, M. Sadd, and H. Mei, "Experimental and computational modeling of wave propagation in granular materials," *Exp. Mech.*, vol. 30, no. 4, pp. 377–381, 1990.

[48] M. Sadd, L. Qiu, W. Boardman, and A. Shukla, "Modelling wave propagation in granular media using elastic networks," *Int. J. Rock. Mech. Min.*, vol. 29, no. 2, 1992.

[49] A. Leonard, F. Fraternali, and C. Daraio, "Directional wave propagation in a highly nonlinear square packing of spheres," *Exp. Mech.*, pp. 1–11, 2011.

[50] A. Leonard and C. Daraio, "Stress wave anisotropy in centered square highly nonlinear granular systems," *Phys. Rev. Lett.*, vol. 108, p. 214301, May 2012.

[51] A. P. Awasthi, K. J. Smith, P. H. Geubelle, and J. Lambros, "Propagation of solitary waves in 2d granular media: a numerical study," *Mechanics of Materials*, vol. 54, pp. 100–112, 2012.

[52] I. Szelengowicz, P. Kevrekidis, and C. Daraio, "Wave propagation in square granular crystals with spherical interstitial intruders," *Physical Review E*, vol. 86, no. 6, p. 061306, 2012.

[53] I. Szelengowicz, M. Hasan, Y. Starosvetsky, A. Vakakis, and C. Daraio, "Energy equipartition in two-dimensional granular systems with spherical intruders," *Physical Review E*, vol. 87, no. 3, p. 032204, 2013.

[54] M. Sadd, Q. Tai, and A. Shukla, "Contact law effects on wave propagation in particulate materials using distinct element modeling," *Int. J. Nonlin. Mech.*, vol. 28, no. 2, pp. 251–265, 1993.

[55] A. Leonard, C. Daraio, A. Awasthi, and P. Geubelle, "Effects of weak disorder on stress-wave anisotropy in centered square nonlinear granular crystals," *Physical Review E*, vol. 86, no. 3, p. 031305, 2012.

[56] C. S. Chang and J. Gao, "Non-linear dispersion of plane wave in granular media," *Int. J. Nonlin. Mech.*, vol. 30, no. 2, pp. 111–128, 1995.

[57] J. Anfosso and V. Gibiat, "Elastic wave propagation in a three-dimensional periodic granular medium," *Europhys. Lett.*, vol. 67, no. 3, p. 376, 2004.

[58] A. M. Tichler, L. R. Gómez, N. Upadhyaya, X. Campman, V. F. Nesterenko, and V. Vitelli, "Transmission and reflection of strongly nonlinear solitary waves at granular interfaces," *Phys. Rev. Lett.*, vol. 111, p. 048001, Jul 2013.

[59] R. M. Corless, G. H. Gonnet, D. E. G. Hare, D. J. Jeffrey, and D. E. Knuth, "On the Lambert W function," *Adv. Comput. Math.*, vol. 5, no. 1, pp. 329–359, 1996.

[60] H. Goldstein, C. P. Poole, and J. L. Safko, *Classical mechanics*. Addison Wesley, 2002.

[61] S. Plimpton, "Fast parallel algorithms for short-range molecular dynamics," *J. Comput. Phys.*, vol. 117, no. 1, pp. 1–19, 1995.

[62] P. Panat, *Classical Mechanics*. Imperial College Press, 2005.

[63] V. Bhatia, *Classical Mechanics: With Introduction to Nonlinear Oscillations and Chaos*. Narosa Publishing House, 1997.

[64] S. Pnevmatikos, N. Flytzanis, and M. Remoissenet, "Soliton dynamics of nonlinear diatomic lattices," *Phys. Rev. B*, vol. 33, pp. 2308–2321, Feb 1986.

[65] J. Cole and J. Kevorkian, "Multiple scale and singular perturbation methods," *Appl. Math. Sci*, vol. 114, 1996.

[66] D. Logan, *A first course in the finite element method*. Cengage Learning, 2011.

[67] J. N. Reddy, *An introduction to the finite element method*, vol. 2. McGraw-Hill New York, 1993.

[68] A. H. Nayfeh and D. T. Mook, *Nonlinear oscillations*. John Wiley & Sons, 2008.

[69] E. Wang, M. Manjunath, A. P. Awasthi, R. K. Pal, P. H. Geubelle, and J. Lambros, "High-amplitude elastic solitary wave propagation in 1-d granular chains with preconditioned beads: Experiments and theoretical analysis," *Journal of the Mechanics and Physics of Solids*, 2014.